Explorations into the structure modification of amorphous silica surfaces and the implications to water dynamics at the interface: A theoretical study

Pubudu N. Wimalasiri

Submitted to the graduate degree program in Department of Chemistry, University of Kansas and the Graduate Faculty of the University of Kansas in partial fulfillment of the requirements for the degree of Doctor of Philosophy.

Committee members

Ward H. Thompson, Chairperson

Brian B. Laird

Marco Caricato

Mikhail V. Barybin

Craig P. Marshall

Date defended: December 15, 2020

The Dissertation Committee for Pubudu N. Wimalasiri certifies
that this is the approved version of the following dissertation :

Explorations into the structure modification of amorphous silica surfaces and the implications to water dynamics at the interface: A theoretical study

Ward H. Thompson, Chairperson

Date approved: December 17, 2020

Abstract

Amorphous silica (a-SiO_2) is used in a wide range of applications that include separations, sensing, optical processing, drug delivery, and catalysis. Its advantages include low cost, optical transparency, ready synthesis, and structural and chemical tunability. At the same time, the properties of a-SiO_2 in these and future applications are not completely understood. Amorphous silica is difficult to characterize due to its intrinsic disorder, the wide variety of synthetic approaches, and the critical role of buried interfaces in its mesoporous forms. This gives an impetus to modeling studies that can provide insight into the relationships between the structural features and functional properties of a-SiO_2.

In this work, we address this issue through the development and characterization of realistic, atomistic a-SiO_2 slab models. Syntheses of amorphous silica involve steps that occur on timescales of minutes to hours and are therefore not feasible for direct computational simulations. Thus, the present approach is an artificial one designed to reproduce the range of experimental a-SiO_2 structures with methods accessible by molecular dynamics methods. Specifically, a melt-quench-functionalize procedure is described that permits variation of a number of the key a-SiO_2 properties including surface roughness, defect density, silanol density, and silanol spatial distribution.

The developed melt-quench-functionalize algorithm generates a disordered silica structure *via* melting, by heating to a high temperature within molecular dynamics simulations, a crystalline silica sample and cutting it to make a slab. The molten slab is equilibrated before cooling back to room temperature at a rate that is too rapid to allow recrystallization, producing an amorphous silica solid. Finally, the resulting solid slab is functionalized using an *ad hoc* procedure that mimics a hydroxylation reaction by adding a water molecule across a silicon-oxygen bond.

The melt-quench-functionalize approach is applied to produce more than two thousand slab models using multiple force fields that have previously been developed to describe crystalline and

amorphous silica. The properties of the resulting slabs are characterized in detail as a function of the cooling rate and the details of the functionalization algorithm. In nearly all cases the bond and angle distributions of the silica structure are in excellent agreement with prior experimental measurements, but we further analyze the density and location of coordination defects and ring structures as well as the atomic-scale surface roughness.

We show that the cooling rate has important effects on the quenched disorder silica structure. In particular, it modulates the surface roughness of the slabs, which is a key feature of silica surfaces that has been generally overlooked in modeling efforts. We find that faster cooling rates result in rougher slab surfaces while slower cooling rates generate smoother interfaces. The cooling rate also influences the number of coordination defects present in the solid, with more rapid cooling preventing rearrangement of five-coordinate silicon and three-coordinate oxygen atoms.

The functionalization method has been developed to be flexible and is automated within a computer code. Specifically, the total silanol density can be controlled by continuing to select silicon-oxygen bonds for hydroxylation until the desired number of surface hydroxyl groups is achieved. We also show that the spatial distribution of silanols can also be varied by identifying silicon-oxygen bonds for functionalization in different ways, *i.e.*, by finding strained (elongated) bonds or by a random selection of bonds. The former leads to more clustered silanols due to the correlation position of strained bonds in the silica.

Finally, the effect of the roughness of the a-SiO_2 surfaces on the dynamics of a liquid at its interface is examined. Understanding water confined within silica frameworks is important both because of its occurrence in natural geological structures and its relevance to applications that involve aqueous solutions. Thus, we use the developed slab models to create three nanometer wide amorphous silica slit pores, using surfaces of varying roughness and investigate the confined water dynamics, specifically OH reorientation, using molecular dynamics simulations. We find that the reorientational dynamics are slowed in the pores with larger surface roughness. The effect is limited to the first one to two water layers at the silica interface, which, however, is where much of the important chemistry in mesoporous materials occurs.

To my loving parents,

Weerappuli Radage Wimalasiri & Kuruppu Mudiyanselage Swarnalatha Wimalasiri

for your dedication and commitment to make me the person that I am today.

Acknowledgements

My graduate career at the Department of Chemistry, University of Kansas was a very rewarding and amazing journey. Many mentors, teachers, friends, and family helped me achieve this goal and I am indebted to each and every one of them. Starting from my advisor, Prof. Ward Thompson, who was the best mentor and teacher that I've had in my whole academic career. I am deeply humbled and grateful that you accepted me to your group Ward; thank you so much for all the encouraging words, intriguing research opportunities, and metoring where I was able to learn and become a confident researcher. I've enjoyed the coffee breaks, group lunches and every time I was invited to your home to spend quality time with your family. I wish you all the very best in your future endeavors, and the very best of health.

I owe so much gratitude to Prof. Brian Laird and Prof. Marco Caricato for the valuable guidance, suggestions, and support throughout my time at KU. I enjoyed our conversations and learnt a lot from them. I am also very grateful to Prof. Cindy Berrie and Prof. Christopher Elles for your confidence in my teaching abilities. I cherished each of the teaching opportunities which was altogether a rewarding experience.

I would like to thank my committee members, Prof. Mikhail Barybin, Prof. Craig Marshall, and Prof. Krzysztof Kuczera fo spending some of your valuable time with me by serving in my committee. I have always enjoyed your spirited comments and questions Misha, and I thank you for your input.

The Thompson Group members were just amazing. Special thanks to Dr. Jacob Harvey helping me get started on working with silica. Dr. Pansy Patel, Dr. Oluwaseun Mesele, and Dr. Hiranya Mendis were so helpful and supportive. A shoutout to the "loud room" composition: Ankita (mom), and the children, myself, Hasini, and Ashley. Zeke, Prof. Yantun, Sahan, Ally, and TJ, thank you for the support and fellowship, I will always cherish my time with all of you.

My undergraduate mentors were crucial in my success as a researcher. I am very thankful to Dr. Udayana Ranatunga, my undergraduate supervisor for the amazing support and mentorship in getting me started with molecular dynamics. You are one of the pillars without which this journey would not have been possible. Also to my mentors, Prof. Chandani Perera, Dr. Vajira Seneviratne, and Prof. Namal Priyantha for your confidence in me.

Outside of school, I was blessed with a community of wonderful fellow Sri Lankans. I did not miss home when I was with them, because it felt as if I was home. The adult power-duo of the community, Nalin, Chamani, and their little daughter Nethni are my secondary family away from home. They took care of me and supported me always and I am truly happy to have had to spend so much time with them. Secondly, my immediate brothers and sisters, Indeewara-Sachini, Uditha-Sayuri, and Kumuditha-Loshini were amazing; we had the best laughs, and the stupidest of times which made me feel so lucky to have had such a strong bond with such amazing people. Also my KC, and Manhattan friends, especially, Anuruddha-Geetha, Dhammika-Anoja, Meenu, Dishan, Chamiranga, and Devinda for the times that we had a blast. The rest of my wonderful Lawrence peeps, Manjula, Sasanka-Kavisha, Thilina-Sumudu, Nilan-Shiwanthi, Nandana-Achala, Kasun-Malika, Shamal-Mihiri, Dhanushka-Chamalee, Gihan-Dimuthu, Milani, Muditha, Dhanushki, Indika-Pamodha, Piyanka, Sayuri, Chanak-Shakya, Dilupa-Sachindra, Sahan-Prabhavie, Miyuru-Indu, Kasun-Nishama thank you so much for the amazing memories, I will always remember them.

A special shoutout to Dr. Amy Jystad, Dr. Tal Aharon, Dr. Chris Otolski, Paul Burris, Brittany Sanders, Zeke Piskulich and Kelci Schilly for the amazing fellowship. From getting pizza before proctoring, playing softball to hanging out at Merchants, you guys helped me take a load off when it was needed.

If not for the loving support from my family, I would not have been able to come this far. Dear amma, I came all this way because of you. Your strong will and commitment to me and my brother has reached fruition today. I will never be able to account for the sacrifices that you made to bring me this far, but I promise to keep working hard making you proud of the son that you brought up.

Thaththi, you may not have always said the best of things, but in a way, you prepared me to survive in the outside world and for that I thank you. Malli, you were my inspiration to achieve greatness. You were always there for me and a man that I know I can count on, and for that, I thank you. To my amazing wife who is the best thing that ever happened to me; Hashini, you make me a better person by the day, your love makes me want to push harder and dream to better our future together; thank you. Thank you so very much for what each of you have given me; I am a better son, a better sibling, and a better husband thanks to each and everyone of you and I love you.

Contents

List of Figures

List of Tables

Chapter 1

Overview

1.1 Amorphous Silica (a-SiO_2) Materials in Catalysis

Silicon dioxide supports are widely used in heterogeneous catalysis. The silica itself is generally inert, but the large, tunable surface area of mesoporous silica is advantageous for maximizing the catalyst density while maintaining accessibility to reactants. Catalysts can either be grafted to the surface after preparation or directly incorporated into the a-SiO_2 synthesis reactant mixture to generate isolated metal sites.[8–11] The a-SiO_2 structure can serve not only as a support for metal active sites, but can also act to promote catalytic reactions.[12, 13] These properties make silica an important component of the development of catalytic systems.

The work of Yan *et al.* on the synthesis of ethylene oxide (EO) *via* epoxidation is a key example of the use of silica as a support for single-site metal atom catalysts.[9] The goal of their work was the development of a green catalyst for generating EO from ethylene using Nb-incorporated mesoporous silica materials. They successfully demonstrated ethylene epoxidation using multiple stable and selective catalysts in gas-expanded liquids using H_2O_2 as an oxidant. The silicate supports used in their work are easy to synthesize and have advantages that include flexible pore sizes, tunable surface chemistry, and environmentally benign synthesis protocols. Further, their best catalysts showed EO productivity from ethylene that was competitive or better than the conventional Ag-based gas phase industrial method.[9]

Subramaniam and co-workers have investigated EO formation in these metal-incorporated silicates in great detail.[9, 10, 14] Their studies concluded that framework-incorporated metal species are significantly more active for more epoxidation than homogeneous metal oxide species. Al-

though their extensive study of the reaction kinetics yielded significant mechanistic insights, the work also benefited from theoretical investigations of minimalist models of the active site.[15] However, the kinetics of the catalysis are intrinsically complex due to the diverse ensemble of active sites that are present in these amorphous materials. Each active site will have its own characteristic rate constant for the epoxidation reaction that will determine its contribution to the experimentally observed reaction kinetics.

It remains unknown what features of the active site and surrounding silica are advantageous or deleterious for the catalysis. This is partly due to the difficulty of directly probing the active site structures experimentally. It is anticipated that the disordered structure of a-SiO_2 results in structurally diverse active sites with widely varying reaction activation energies.[16, 17] This leads to the conclusion that only a small number of the active sites are relevant to the catalysis because those with larger activation energies will have negligible contributions (due to the exponential dependence of the rate constant on the Arrhenius activation energy). Indeed, advanced imaging techniques that can identify active sites on a material[18] suggest that only $\sim 1-10\%$ of the catalytic sites contribute to the observed observed kinetics. Thus, even in an ideal situation where the structures of the entire ensemble of active sites can be measured, the vast majority of them will be irrelevant to the catalysis. This provides a powerful impetus for computational methods to correlate active site structure to reactivity.

The most straightforward computational approaches of this type would generate an ensemble of model active sites (*e.g.*, using cluster models centered around the metal atom) and calculate the activation energy of the reaction for each one. Averaging over such active sites will, in principle, predict the experimentally observed turnover frequency, but it will require sampling thousands of active site structures.[17] For each, a transition state search will have to be carried out with (computationally expensive) electronic structure methods to determine the reaction barrier for each individual active site, and the result for the silica-supported catalyst obtained by averaging all of these costly calculations. If this procedure adequately describes the experimental measurements, insight is available by identifying the common features of the sites with low activation energies.

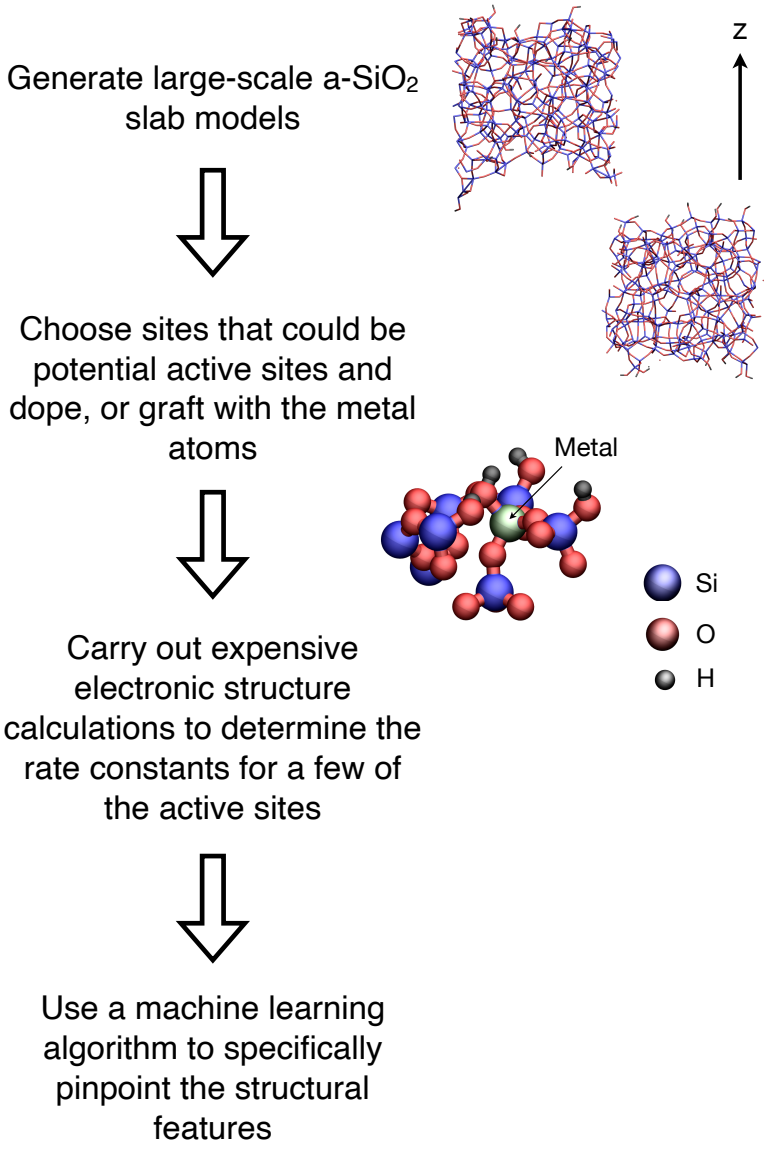

Figure 1.1: Schematic illustration of the approach to determine the reaction kinetics at an a-SiO_2 support.

However, as may be apparent from this description, such a procedure is likely not feasible for most catalytic systems and more cost-effective approaches are required. The present work is part of efforts to develop such methods, motivated, in part, by the work of Subramaniam and co-workers on ethylene epoxidation catalysts based on mesoporous silica. The strategy, illustrated schematically in Fig. 1.1, is to take advantage of emerging machine-learning tools to dramatically reduce the number of active site models for which expensive electronic structure calculations of the barrier height are required. The ingredients of these active site models are a central focus of the work in this thesis. It is envisioned that they can be generated by carving out clusters from a amorphous silica slab models that provide a realistic representation of the quenched disordered structure of those materials. A metal atom can then be incorporated into these clusters to form an active site model on which the electronic structure calculations can be carried out.[19] The resulting estimated rate constants will represent the training set of the machine learning algorithm to identify the structural features around a metal atom that lead to fast reaction rate constants.

A key component of these machine learning approaches, Fig. 1.1, are amorphous silica slab models that span the full range of structural arrangements present in the actual mesoporous support materials. This is a primary focus of the work described in this Thesis. Specifically, the aim is a systematic study of procedures to generate ensembles of silica slab models with an emphasis on controlling and characterizing specific characteristics such as coordination defects, ring structures, surface silanol density, silanol spatial distributions, and surface roughness. This is an important step in efforts to understand the implications of different active site structural features for the resulting reaction kinetics.

1.2 Other Applications of Amorphous Silica

Silica is of broad utility that is not at all limited to catalysis. Indeed, silica is also widely used to do liquid- and gas-phase separations. For example, Mohan and Pittman have reviewed the capability of silica to separate arsenic from ground water which has importance global health implications for generating safe drinking water.[20] In another recent review, Brady *et al.* discussed emerging

technology that can use a-SiO_2 frameworks for food bioactive ingredient separation.[21] As another example application, mesoporous silica has received significant interest as a potential drug delivery agent, where the goal is the development of materials that release a loaded drug molecule in response to a particular stimulus. Key characteristics of silica materials important in this field include biological safety and facile release of biologically active species. In some cases it has been shown that these materials are able to prevent premature release of the drug that occurs for other systems.[22, 23] The ability to tune the pore size and surface chemistry to enhance the drug-silica interaction are key advantages of mesoporous silica frameworks for these problems. Moreover, because silica is transparent over a wide range of the electromagnetic spectrum, they have also been used in encapsulation of bio-imaging organic dyes as a way to reduce photo-bleaching and enhance biocompatibility.[24]

For each of these applications, exploring the effect of the silica surface structure is paramount. In the case of separations, attractive interactions between the surface and the species of interest must be tuned. In drug delivery, the surface properties should prevent the premature release of the drug. Because a primary goal of this study is to develop the methodology to tune the surface properties of a-SiO_2 slab models, it will facilitate the study of surface interactions in these applications as well.

1.3 Theoretical Simulation of Silica

Molecular-dynamics (MD) simulations of amorphous silica are the main focus of this work. A brief discussion of the significant advances that have been made in this area over the past few decades. In general, field has evolved along two parallel tracks, classical MD simulations to describe long-time and lengthscale behavior, including phase equilibria, and electronic structure methods on clusters or small periodic models, primarily focused on the surface chemistry.

The crystalline phases of silica have been modeled with reasonable success using a wide variety of classical force fields beginning for more than 40 years. One of the earliest studies was carried out by Woodcock *et al.*[25] and subsequent variations and advances have resulted in force fields

that reproduce the structure and thermodynamics of both crystalline and amorphous silica.[1, 2, 4–7, 26, 26–35] Because of significant interest in the phase behavior of silica, early descriptions focused on reproducing the structures and relative stability of the crystalline phases using pair-wise interaction models with fixed charges.

Indeed, crystalline and amorphous silica have been investigated with a wide variety of fixed-charge force fields. While these approaches cannot generally describe chemical reactivity (outside of the SiO_2 solid), polarization, or charge transfer effects, they have been successfully used to describe the phase behavior of silica as well as the properties of the amorphous solid. In addition, they have been used effectively in describing the interactions of silica with liquids,[7, 36–57] particularly for chemical phenomena that require long simulation times.[52, 53] Several force fields have been shown to display transferability between crystalline phases and even to amorphous silica.[58] Most of these force fields share a common structure of electrostatic interactions combined with shorter-ranged potentials describing van der Waals interactions.[1, 2, 4–7, 26–28] They differ primarily in the quantitative balance between these two components as well as the form of the latter as either Buckingham,[1, 2, 29] Lennard-Jones,[6, 7, 27, 28] or Morse[4, 5] potentials.

Significant work has been aimed at improving upon these pair-wise force fields, the simplest of which incorporate many-body interactions. Feuston and Garofalini added a three-body term to the pair-wise Born-Mayer potential[31] to improve the tetrahedral angle distribution and bond defect compositions in vitreous silica.[32] Using a melt-quench method to form the silica framework they found that the bond defects decreased from 6-8% to 1-2% when this term is added. Vashishta *et al.* also developed a three-body interaction potential to describe some silica crystalline phases and amorphous silica and showed that this model described the angular distributions in the amorphous solid well.[33] In some cases, "hard" potentials (*i.e.*, those with large Si and O charges) exhibit an elevated melting point while "soft" potentials (*i.e.*, those with smaller Si and O charges) agree well with the experimental melting point of silica but fail to describe the density changes at low temperatures.[58]

Multiple reactive force fields have also been developed that can describe chemical rearrange-

ments important in the chemistry of silica, *e.g.*, hydroxylation and dissolution reactions. For example, Demiralp *et al.* used a charge equilibration approach to model the pressure-induced phase transition from quartz to stishovite.[30] More recently, a description of silica that can model bond formation and breakage was included by van Duin and co-workers within the their ReaxFF framework, which uses a relationship between the bond distance and bond order.[34, 59] The Duin *et al.* ReaxFF description was improved by Forgarty *et al.* to better predict the properties of bulk silica and reactions that occur at the water-silica interface.[35] Kulkarni *et al.* used ReaxFF in a one-to-one comparison with electronic structure calculations for the reaction of O_2 with realistic silica clusters including both defect and non-defect sites.[59] They showed that the ReaxFF interaction energies agree very well with the, much more computationally expensive, electronic structure calculations. A comparison of the ReaxFF Si/O/H force field developed by Yeon *et al.*[60] was carried out by Rimsza *et al.*,[61] who found that it gave results in accord with *ab initio* calculations for the reaction of water with nanoporous silica. Other reactive force fields include those based on the dissociative water model by Garofalini and co-workers,[62, 63] who have used the model to examine the dissolution of *a*-SiO_2 silica in water. Their calculated activation energies for dissolution were at the lower end of the experimental range of values, but slightly different from *ab initio* cluster calculations.[64]

The past two decades have see the application of *ab initio* molecular dynamics (AIMD) to investigations of crystalline and amorphous silica.[65–76] The computational expense of these approaches limits them to small unit cells and short simulation times. However, AIMD simulations have also been used to benchmark classical force fields that can avoid these limitations.[67, 68] For example, this approach has been used to identify shortcomings in force field descriptions of coordination defects[65] and the vibrational density of states of an *a*-SiO_2 surface.[66] However, in some instances, classical force fields are able to show comparable behavior to AIMD as was found for the description of the water structure at the quartz($10\bar{1}1$)-water interface,[67] while in others they display a more mixed performance.[68] More generally, AIMD simulations have been used to describe the surface reactivity, including acid-base chemistry, at both crystalline and amorphous

silica interfaces.[69–76]

Unfortunately, none of these descriptions of silica can explicitly model the experimental timescales of amorphous silica synthesis, which takes at least minutes or hours. This is the process that determines the surface structure, and hence the active site environments in silica-supported catalysts, which is a key target of this work. Thus, we make use of methods that aim to simulate the *a*-SiO_2 structure (see Chapter 2), but not the process by which it is created. Even with these approaches, AIMD simulations, the most accurate descriptions of silica, are not feasible because of the required system sizes and simulation times. These methods can be carried out with reactive force fields such as ReaxFF.[34, 60, 77] However, ReaxFF is approximately fifty times more computationally expensive than a fixed-charge force field. Thus, in the present study we use such simple, pair-wise force fields, which have been shown accurately describe amorphous silica,[58] to explore and test approaches for generating *a*-SiO_2 slab models that can be used in descriptions of catalysis. They permit simulations involving large system sizes and long timescales that are not significantly limited by the computational effort. These efforts will also assist in the future application of similar approaches based on more complex, and computationally costly, descriptions of silica interactions.

The first aim of this study is to develop models that are representative of the actual amorphous silica structures from the wide variety of synthetic methods that are in use. We focus first on the pair-wise "BKS" force field developed by van Beest, Kramer, and van Santen[1] that is perhaps the most widely used model for *bulk* amorphous silica because of its effectiveness in predicting structural properties[78]. In Chapter 2 we propose a melt-quench-functionalize procedure for generating *a*-SiO_2 slab models in which the silanol density, silanol distribution, and surface roughness can be tuned. The application of this approach using the BKS force field is presented in Chapter 3 with a detailed analysis of the features of the resulting amorphous silica slab models. These results are compared to analogous slab models generated by using three other pair-wise silica force fields in Chapter 4.

1.4 Silica-Water Interfaces

The interactions of silica with water has long been of interest because of its relevance to geological systems, separations in aqueous media including water purification, and catalysis. In the case of the last, which motivates much of the present work, the role water in heterogeneous catalysis is diverse. Varghese *et al.* have noted that the solvent can change the reactivity, catalyst structure, and product selectivities in heterogeneous catalysis.[79] Reactivity can be influenced by either direct solvent involvement in the mechanism, *e.g.*, *via* hydrogen-atom transfer, or indirectly, where water can stabilize reactive intermediates through hydrogen bonding.[80] On the other hand, if a silica catalyst support preferentially hydrogen bonds to water over the reactant, the catalysis can be inhibited. Similarly, metal leaching through dissolution in aqueous solution is a mechanism for catalyst deactivation.[9] Water reacting with the silica frameworks has also been observed in zeolites at high temperatures.[81] These considerations indicate the importance of understanding the behavior of water, and solvents more generally, at the silica interface.

The behavior of water at silica surfaces has been investigated both experimentally[82–89] and theoretically[36, 37, 43, 84, 90] in non-confining geometries. Special attention has been given to the hydrophilicity of the surface modulated through charge scaling[43] or *via* changing the hydroxyl density.[36, 37] Some of the most detailed characterizations have made use of vibrational sum-frequency generation (SFG) experiments, which are surface sensitive.[86–89] Early interpretations of these spectra concluded that they showed evidence of ice-like water at the silica interface.[86, 87] More recent work has demonstrated that the "ice-like" features are instead due to resonant vibrational coupling and disappear when the water is isotopically dilute, *i.e.*, HOD dilute in D_2O or H_2O.[88, 89]

These measurements also indicate that the SFG spectra differ between amorphous silica and crystalline quartz interfaces,[86, 87] and are also modulated for a-SiO_2 surfaces by the surface charge (which can be controlled through the solution pH).[88, 89] Connected to this, the mechanism for slowed dynamics observed in simulations at diverse hydrophobic/hydrophilic pores has been attributed to the ordering of water near the interface.[43] However, other characteristics such

as surface curvature and roughness have not been systematically investigated. One study has found that curvature in the nanoconfining framework destabilizes the tetrahedral ice structure formation of water, even at the bulk limit, preventing crystallization.[84] This is consistent with the general behavior of depressed freezing points for nanoconfined solvents due to the confining framework inhibiting the long-range order of the crystalline structure. The implications for dynamics are still unclear. Experimentally, the structure of water in MCM-41 has been determined through neutron diffraction measurements[85] that suggest, for pore diameters of more than 2 nm, that the water structure and dynamics are perturbed primarily at the interface, while the pore center behaves more like the bulk liquid.

The changes in the water structure and dynamics at a silica surface are representative of the silica structure. A key open issue in the field is the relationship between the silica surface structure, *e.g.*, silanol density, silanol distribution, roughness, and experimentally measurable properties such as vibrational spectra. The amorphous silica slab models generated in this work provide an opportunity to probe these connections and thereby assist in the interpretation of measurements of silica-water interfaces. A first effort in this direction is presented in Chapter 5 where the effect of surface roughness on the interfacial water reorientational dynamics is investigated.

Chapter 2

Simulation Methods

2.1 Overview

The central focus of this work is improved modeling and understanding of amorphous silica interfaces. As discussed in Chapter 1, these materials are of significant interest in applications from catalysis to drug delivery as well as for understanding naturally occurring geological systems. A key goal of the present work is the generation of amorphous silica slab models that can be used in studies of *i)* catalysis, where the silica serves as a support for transition metal active sites, *ii)* interfacial dynamics, where a fluid in contact with the silica surface exhibits modified behavior that affects key chemistry, or *iii)* confinement effects, in which two silica surfaces modify the overall properties of a nanoscale-wide liquid layer. In this Chapter, the approaches used to generate amorphous silica slab models with varying properties are described. The properties of these silica slabs as a function of variations in the procedure for different force fields are described in detail in Chapters 3 and 4. The behavior of water confined in nanoscale slit pores between two silica slab interfaces obtained with these approaches is examined in Chapter 5.

2.2 Procedures for Slab Generation

The approaches used here are based on the widely applied melt-quench method.[6, 7, 31, 78, 91–93] Amorphous silica is synthesized by a wide range of methods, all of which take place on timescales that are too long to be feasibly simulated explicitly in an atomistic description. Thus, computational models seek to represent the disorder present in the material by other means. The

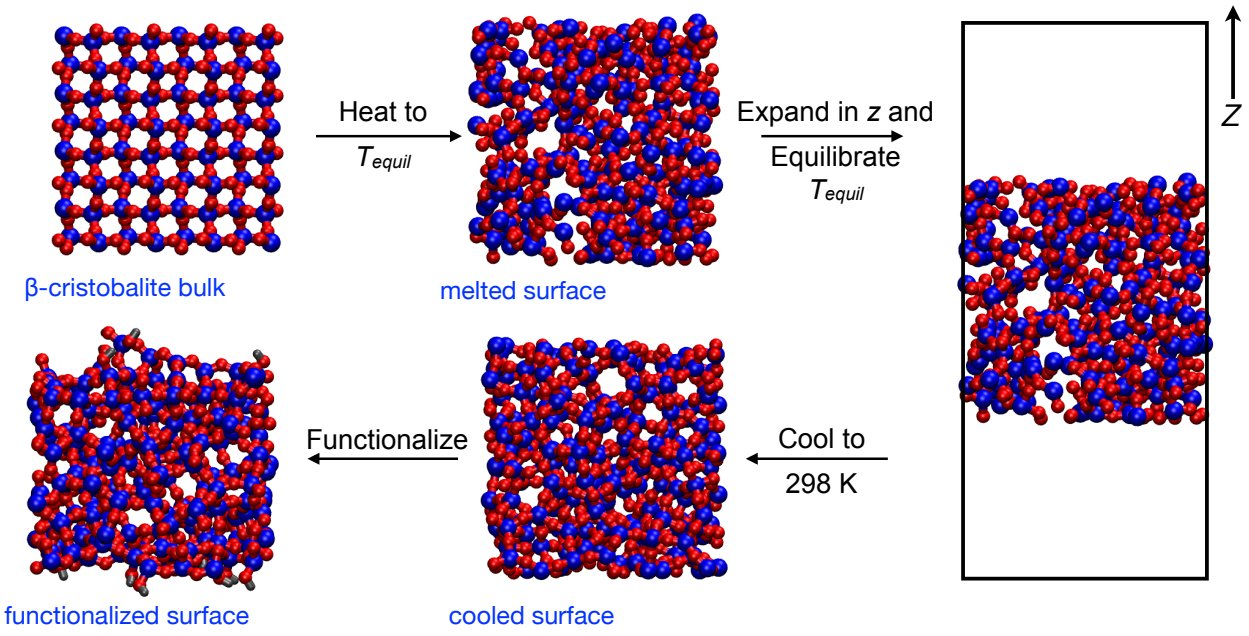

Figure 2.1: Schematic illustration of the simulation procedure for the generation of silica slabs.

most straightforward approach is to melt crystalline silica and then quench the resulting liquid by cooling to room temperature at a rate that is sufficiently fast to prevent crystallization. (Indeed, it is actually difficult within computer simulations to cool slowly enough to *allow* crystallization.)

Probably the most common melt-quench-based approach for generating slab or pore models is to subsequently "cleave" the amorphous solid to generate the desired planar or curved interface. This naturally results in a large number of undercoordinated silicon and oxygen atoms which are then terminated by addition of OH groups (or sometimes O atoms). This cutting method generally leads to relatively flat interfaces, which is likely not representative of many actual amorphous silica surfaces that are synthesized using sol-gel techniques.[8, 94–96] In the present work, we aim to avoid this issue, and even explicitly vary the surface roughness, by carrying out the cutting step in the molten silica before the quench process.

2.2.1 Melt-Quench-Functionalize Algorithm

We now describe in detail the algorithm for generating the amorphous silica slab (and bulk) models. This procedure is illustrated schematically in Fig. 2.1 and the detailed characterization of the

resulting models using different force fields (see Sec. 2.2.3) are the focus of Chapters 3, and 4. The melt-quench-functionalize process proceeds as follows:

1. A β-cristobalite structure is heated to a high temperature, T_{equil}, over 1 ns to form molten silica. The simulations are carried out in the NPT ensemble using a Berendsen thermostat with a damping constant of 1 ps (modulus parameter of 360,000 atm) to control the temperature while the pressure is maintained at 1.0 atm with a Berendsen barostat (time constant of 1 ps). The equilibration temperatures used are given in Table 2.1.

2. The size of the periodic simulation cell is expanded in the z-direction to 80 Å to create a molten silica slab. In generating bulk silica models, this expansion step is skipped. The resulting slab is then equilibrated for an adequate time, given in Table 2.1, to relax the silica after this "cutting" event. It is at this point that atomistically different slabs can be obtained by using different initial velocities (selected from a Boltzmann distribution) for this slab equilibration stage. The high T_{equil} temperature ensures that atoms can diffuse from one slab interface to the other multiple times during the equilibration. The equilibration is propagated in an NP_zAT ensemble in which the thermostat and barostat parameters are the same as in the melting stage, Step 1.

3. An amorphous silica slab is generated through cooling back to 298 K by ramping the temperature in the same NP_zAT ensemble at a specific cooling rate. Silica slabs with different properties can be generated by varying the cooling rate; the rates used for the different force fields are listed in Table 2.1. The slab is further equilibrated at room temperature for an additional 1.5 ns.

4. The surfaces of the resulting a-SiO_2 slabs are functionalized using an *ad hoc* procedure that is described in Sec. 2.2.2.

5. Finally, the functionalized slab is relaxed using either available, or modified, force field parameters for 1 ns at 298 K in the same NP_zAT ensemble.

	Parameters		
Force Field	T_{equil} (K)	Equilibration Time (ns)	Cooling Rates (K/ps)
BKS	8000	3	1, 5, 25, 100, and 1000
CHIK, Clayff, Takada	4000	6	1

Table 2.1: Equilibration temperature in melting the β-cristobalite initial structure and equilibrating the molten silica slab (Steps 1 and 2), the equilibration time used for the molten slab (Step 2), and the cooling rate parameters (Step 3) used for the different force fields.

Note that in the above, NVT refers to a simulation with fixed volume (*i.e.*, constant simulation box length in all three dimensions), number of particles, and temperature. The last is maintained by a Berendsen thermostat[97] as described above. In the NPT ensemble, the box dimensions are allowed to change (equally in all three dimensions) according to a Berendsen barostat.[97] For the slabs the NP_zAT ensemble is used in which the x and y dimensions (nominally parallel to the slab interfaces) are fixed and the volume of the simulation cell only changes through its z dimension, also according to a Berendsen barostat.[97] The length of equilibration at each stage was determined by checking convergence for a small number of slabs in initial testing. Similarly, the thermostat and barostat time constant (which determine how strongly the velocities and volume, respectively, are scaled at each timestep to match the desired temperature and pressure).[98]

Both bulk and slab a-SiO_2 models were generated using molecular dynamics simulations carried out with the Large-scale Atomic/Molecular Massively Parallel Simulator (LAMMPS) code.[98, 99] In all cases reported here, the initial structure is a β-cristobalite crystal consisting of 192 silicon and 384 oxygen atoms with periodic boundary conditions in all three dimensions of a cubic simulation cell of box length 19.912 Å in both x and y, and 20.844 Å in z. All simulations used a 1 fs timestep. A three-dimensional Ewald summation[100] with a tolerance of 1.0 x 10^{-4} was used to treat the long-range electrostatics; note that the vacuum phase is approximately three times larger than the z-dimension of the slab, minimizing slab-slab interactions in the Ewald sum. The secondary cutoff for the Buckingham potential was set to 8.0 Å.

Note that, when the BKS force field is used, the β-cristobalite was melted by heating to 8000 K; see Table 2.1. While this high temperature leads to more rapid randomization and equilibration of the molten silica, particularly after creation of a slab, few other force fields describe a stable

liquid above 4000–5000 K. Indeed, silica is likely not stable with respect to evaporation at such temperatures and this feature of the BKS model, while convenient for simulation, is unrealistic. However, this means that the same approach cannot be used for the other force fields considered here and a lower temperature, here 4000 K, must be used.

2.2.2 Surface Functionalization

2.2.2.1 Identification of Surface Atoms

The prelude to a functionalized surface is the identification of the surface atoms, which is accomplished by the following procedure. The $x-y$ plane is divided into a square grid with spacings of 0.3 Å in each dimension. At each point in this grid a probe atom of radius 1.4 Å is brought toward the slab from the vacuum phase until it makes contact with a slab atom. The latter is then identified as part of the surface. Contact is determined from the contact distance of the probe atom and the slab atom using a radius of 1.04 or 0.76 Å for Si and O atoms, respectively. These radii were determined by trial and error in which the correct identification of surface atoms was confirmed by visual examination for multiple test slabs.

2.2.2.2 Hydroxylation Algorithm

The bare SiO_2 surfaces were hydroxylated using the simple procedure developed previously in our group[6, 7] and illustrated schematically in Fig. 2.2. The approach is designed to ensure charge neutrality of the resulting functionalized surface by simulating the result of a hydrolysis reaction between a (neutral) H_2O molecule and an accessible Si–O bond. One of the water H atoms is added to the silica O atom while the remaining OH is bonded to the Si. As noted in Sec. 2.2.3.6, only the charges in the silanol O and H atoms are modified to maintain a zero net charge for the silica slab. We continue to select Si–O bonds for functionalization until the desired silanol density is achieved and an equal number of silanols are present on the top and bottom surfaces.

Once the surface atoms are identified, two algorithms were used for selecting the Si–O bonds

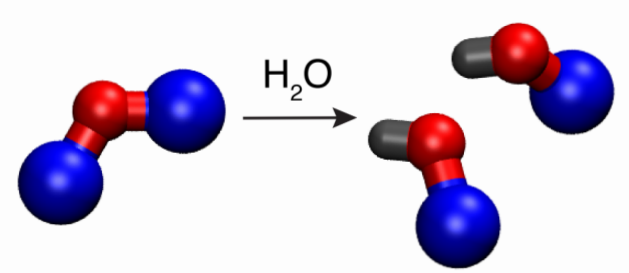

Figure 2.2: Illustration of the *ad hoc* silica surface functionalization in which a water molecule is added across an Si–O bond.

for functionalization. In the first, the surface Si–O bonds are ordered by increasing length. The Si–O bonds are chosen for functionalization according to their length, beginning with the longest bond and moving in decreasing order, until the desired silanol density is attained. The second method randomly picks surface Si–O bonds to be functionalized. With either method, a water molecule is added across the selected Si–O bond. A Monte Carlo algorithm is used to determine whether the O atom of the added silanol can functionalize the chosen Si atom without overlapping with any of the surrounding atoms by varying its orientation and checking for steric overlap with surrounding slab atoms. This ensures proper functionalization, for example, of Si atoms that are more "buried" within the silica surface. If the algorithm is unable to find a position for the oxygen atom of the silanol, that Si–O bond is deemed unfit for functionalization and the next Si–O bond is considered. The H atoms of the silanols are positioned directly above (in the z-direction) the determined O positions, pointing away from the surface.

It is important to note that the first approach tends to give a silanol surface distribution that is more clustered due to the spatial correlation between elongated Si–O bonds, *i.e.*, strained bonds are more likely to be found near each other. Thus, choosing strained Si–O bonds for functionalization assumes a spatially non-uniform silanol distribution. It is not clear if this is the reality for amorphous silica (or some, but not all, methods of preparing amorphous silica) and part of our motivation for using the two approaches is to generate models with different surface silanol distributions, a topic that has received relatively little attention.[101] A longer-term aim is to use such models to examine experimentally measurable differences in the silica surface properties of

	Silanol Density (OH/nm^2)	
Force Field	Target = 2.0	Target = 4.0
BKS	2.04 or 2.26	4.08 or 4.30
CHIK	2.11 or 2.34	
ClayFF	2.33–4.43	
Takada	2.11 or 2.34	

Table 2.2: Silanol densities obtained from the functionalization procedure described in the text and illustrated in Fig. 2.2.

the two distributions.

The algorithm has been further modified to generate more realistic surfaces. First, in slabs where a singly-coordinated O atom and a 3-coordinate Si atom are present, they are also functionalized by addition of an H atom to the O atom and an OH group to the Si atom. Second, in cases where the functionalization would result in an $Si(OH)_3$ group it is rejected. Note that the fraction of geminals could be straightforwardly controlled in an analogous way, but we have not done so here. In the present work, slabs with target silanol densities of 2 and 4 OH/nm^2 were generated. Precise silanol densities are provided in Table 2.2 for the particular force field.

The differences arise from the presence or absence of the undercoordinated sites on the surfaces. The variability of the resulting silanol density especially, with the ClayFF force field, is due the presence of significantly more undercoordinated sites as discussed in Chapter 4, Sec. 4.3.2.2.

2.2.3 Force Fields

2.2.3.1 Overview

The approach for generating slab models described above can be applied within any force field description of silica. In Chapters 3 and 4 we examine the results obtained by implementing the algorithm for several fixed-charge silica force fields. Each of these force fields is composed of two basic elements: 1) Electrostatic interactions and 2) van der Waals (repulsive core plus dispersion) interactions. Perhaps surprisingly, the competition between these two simple driving forces is sufficient to describe many of the phases of silica including the amorphous solid. The different

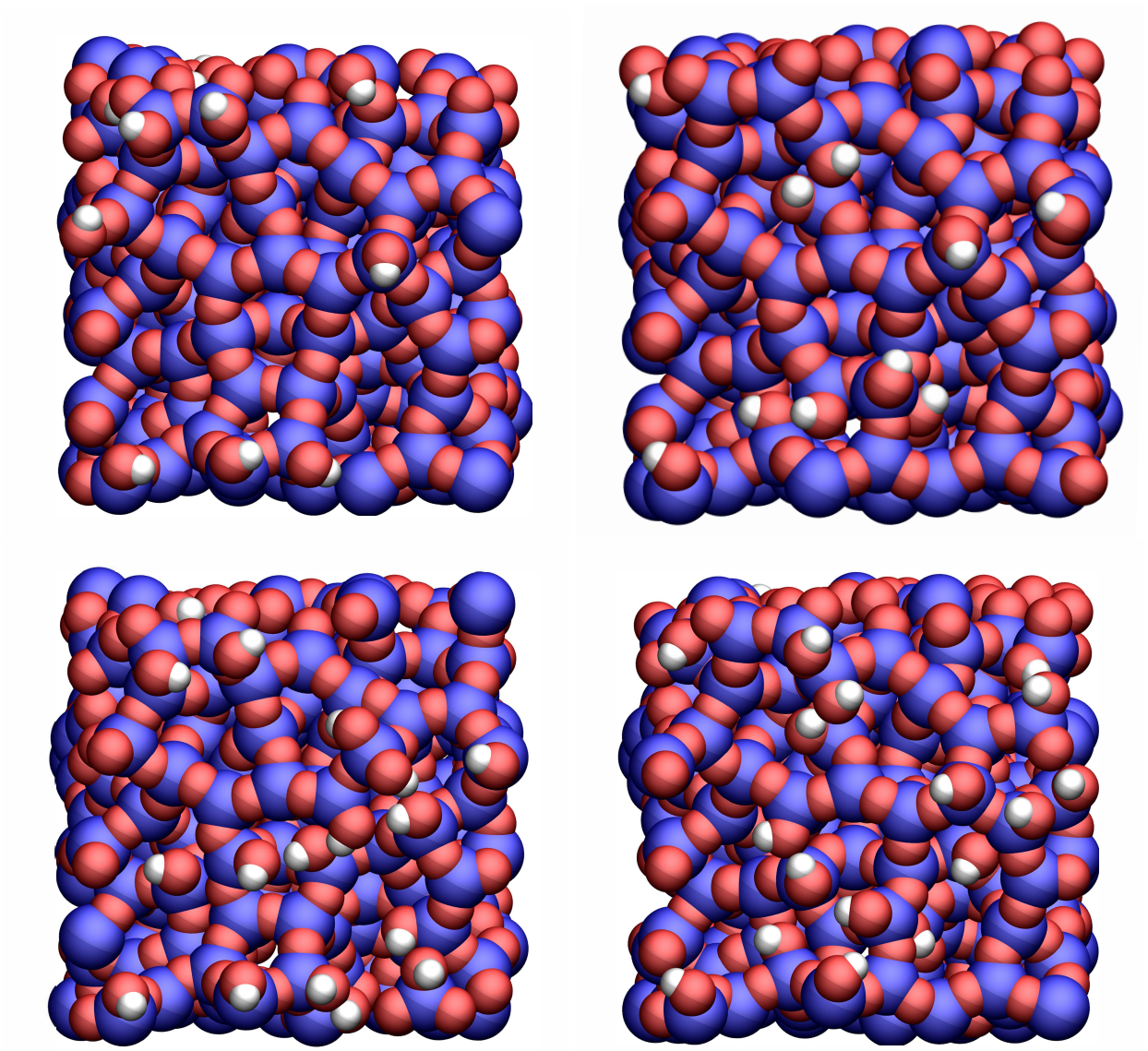

Figure 2.3: Snapshots of a single amorphous silica slab functionalized by the two algorithms described in the text to two different target silanol densities. Structures are shown obtained by adding H_2O across Si–O bonds selected by length (top left: 2 OH/nm^2; bottom left: 4 OH/nm^2) and randomly (top right: 2 OH/nm^2; bottom right: 4 OH/nm^2).

Force Field	vdW Form	q_{Si} (e)	Electrostatic Cutoff (Å)
BKS[1]	Buckingham	2.4	5.5
CHIK[2]	Buckingham	1.91	6.5
ClayFF[3]	Lennard-Jones	2.1	9.0
Takada[4]	Morse	1.3	9.0

Table 2.3: Key features of the four silica force fields considered in this work. Note that $q_O = -q_{Si}/2$.

force fields considered in this work vary primarily in the functional form used to represent the van der Waals term. However, this leads, upon fitting the parameters to measured structural and thermodynamic results, to widely varying pictures for the silica electrostatics. The most significant features of the force fields used in this work, the details of which are described in the following Sections, are listed in Table 2.3. We note that, with one exception, all of these were developed to describe bulk silica and thus lack parameters for surface silanol groups. We have developed a simple approach for including a consistent description of these hydroxyl moieties within each force field that is described in Sec. 2.2.3.6

2.2.3.2 van Beest, Kramer, van Santen (BKS) Force Field

The most widely utilized fixed-charge force field for silica, by far, is the BKS potential developed thirty years ago by van Beest, Kramer, and van Santen.[1]. It describes silica in terms of pairwise interactions between Si and O atoms given by the potential,

$$V(r_{ij}) = A_{ij}e^{-b_{ij}r_{ij}} - \frac{c_{ij}}{r_{ij}^6} + \frac{q_i q_j}{r_{ij}}, \tag{2.1}$$

where i and j denote two atomic sites. The first two terms are the Buckingham, or "exp-6," potential that represents the van der Waals interactions and the third term is naturally the Coulombic interactions. An important component of the BKS force field is that these Coulombic terms are included only at comparatively short distances by using an electrostatic cutoff that is only 5.5 Å. Increasing this cutoff leads to a significantly poorer description of key features of the amorphous solid, *e.g.*, the bulk silica density is overestimated by 10-15%.

	Buckingham Parameters			Atomic Charges	
$i-j$	A_{ij} (eV)	b_{ij} (Å^{-1})	c_{ij} (eV Å^6)	Site i	q_i (e)
Si-Si	0.0000	0.0000	0.0000	Si	2.4
Si-O	18003.7572	4.87318	133.5381	O	-1.2
O-O	1388.7730	2.76000	175.0000		
Si-O_{SiOH}	18003.7572	4.43016	133.5381	O_{SiOH}	-1.02
H-H	0.0000	0.0000	0.0000	H	0.42
O-O_{SiOH}	1388.7730	2.76000	175.0000		

Table 2.4: Parameters for the BKS silica force field.[1] The SiOH subscript denotes a silanol oxygen. All parameters for the silanol atoms were determined in the present work; see Sec. 2.2.3.6.

It is important to note an additional detail of the implementation of the BKS potential. At very small inter-site distances, r_{ij}, the Buckingham potential diverges to negative infinity (the exponential term approaches a constant value while the $1/r^6$ term continues to grow). Because a substantial barrier must be surmounted to reach this region, this is typically not an issue at room temperature, but it can be (and often is) at the high temperatures used in melting the silica. Thus, we add an additional Lennard-Jones potential to prevent this, but with a short cuttoff (1.2 Å) such that only the repulsive part of the potential is accessed. We used $\varepsilon_{Si-O} = 2.0$ eV, $\varepsilon_{O-O} = 2.6$ eV, $\sigma_{Si-O} = 1.2$ Å, and $\sigma_{O-O} = 1.6$ Å.

2.2.3.3 Carré, Horbach, Ispas, Kob (CHIK) Force Field

The Buckingham plus electrostatics form of the BKS model[1] was reparameterized by Carré, Horbach, Ispas, and Kob to match results from *ab initio* molecular dynamics.[2] The resulting CHIK force field thus uses the same site-site interaction model given in Eq. (2.1). The parameters for the CHIK model are given in Table 2.5. Carré used molecular-dynamics simulations to evaluate some of the equilibrium and dynamical properties of silica. They found that the pressure minimum (at fixed density) occurs at a lower temperature for the CHIK potential compared to BKS.[2] Additionally, because it was fit to *ab initio* MD results, the CHIK potential more accurately reproduced the pair radial distribution functions for molten silica compared to BKS. Both the CHIK and BKS force fields give similar activation energies for Si and O atom diffusion in molten silica with values in good agreement with experiment.[2] However, CHIK predicts diffusion coefficients that are

Buckingham Parameters				Atomic Charges	
$i-j$	A_{ij} (eV)	b_{ij} (Å^{-1})	c_{ij} (eV Å^6)	Site i	q_i (e)
Si-Si	3150.462646	2.851451	626.751953	Si	1.91
Si-O	27029.419922	5.158606	148.099091	O	-0.955
O-O	659.595398	2.590066	26.836679		
Si-O_{SiOH}	27029.419922	4.689642	148.099091	O_{SiOH}	-0.8975
H-H	0.0000	0.0000	0.0000	H	0.42
O-O_{SiOH}	659.595398	2.590066	26.836679		

Table 2.5: Parameters for the CHIK silica force field.[2] The SiOH subscript denotes a silanol oxygen. All parameters for the silanol atoms were determined in the present work; see Sec. 2.2.3.6.

approximately five times larger than those obtained from BKS.

In the implementation of the CHIK potential, the cutoff used for the interactions was taken to be 6.5 Å, somewhat longer than that for the BKS force field. The consequences of the divergence of the Buckingham potential at small distances, noted above for BKS, were also encountered with CHIK. We have corrected them in the same way, by adding a short-ranged (effectively only repulsive) Lennard-Jones potential. We used a cutoff of 2.0 Å with $\varepsilon_{Si-Si} = 0.2$ eV, $\varepsilon_{O-O} = 0.2$ eV, $\varepsilon_{Si-O} = 0.5$ eV, $\sigma_{Si-Si} = 2.15$ Å, $\sigma_{O-O} = 1.44$ Å, and $\sigma_{O-O} = 1.34$ Å for the CHIK force field. Note that these parameters differ from those for BKS because they are chosen to provide a smooth potential when added to the Buckingham potential for each force field.

2.2.3.4 ClayFF

Cygan *et al.* proposed a general framework for force fields of clay materials, which they named ClayFF.[3] While this force field is not designed specifically for silica or even amorphous materials, it has been used to describe amorphous silica in multiple studies.[49, 56, 57, 102] ClayFF describes the site-site interactions as a sum of Lennard-Jones and Coulombic potential terms as

$$V(r_{ij}) = \varepsilon_{ij}\left[\left(\frac{\sigma_{ij}}{r_{ij}}\right)^{12} - 2\left(\frac{\sigma_{ij}}{r_{ij}}\right)^{6}\right] + \frac{q_i q_j}{r_{ij}}. \tag{2.2}$$

Note the factor of 2 in the second term of this Lennard-Jones potential. The parameters for each atom (site) are given in Table 2.6. The intersite Lennard-Jones parameters used in Eq. (2.2) are

	LJ Parameters		Atomic Charges
Site i	ε_i (kcal/mol)	σ_i (Å)	q_i (e)
Si	1.8405 x 10^{-6}	3.7064	2.1
O	0.1554	3.5532	-1.05
O_{SiOH}	0.1554	3.5532	-0.95
H	0.0000	0.0000	0.425

Table 2.6: Parameters for the ClayFF.[3] The SiOH subscript denotes a silanol oxygen.

obtained by the standard Lorentz-Berthelot combining rules,[3]

$$\sigma_{ij} = \frac{\sigma_i + \sigma_j}{2} \qquad \varepsilon_{ij} = \sqrt{\varepsilon_i \varepsilon_j} \tag{2.3}$$

Unlike the other three force fields considered in this work, ClayFF was developed including a focus on the modeling of interfacial phenomena at mineral surfaces. Thus, parameters for the description of hydroxyl groups were provided and we use those as given.[3]

2.2.3.5 Takada Force Field

Takada *et al.* developed a model for silica parameterized to reproduce the densities of multiple silica phases (quartz, β-cristobalie, and coesite).[4] Their approach was to use significantly smaller charges on the Si and O atoms in order to better describe not only the silica densities but also the melting temperature. Indeed, the Takada force field predicts a β-cristobalite melting temperature of 2400 K, which is reasonably close to the measured value of 2000 K and particularly lower than the more than 3000 K given by BKS. In particular, Soules *et al.* compared the transition from liquid to solid using the BKS,[1] CHIK,[2] and Takada,[4] and their own, Soules, force field.[26] They concluded that the magnitude of the charges plays a key role in determining the melting point of β-cristobalite and the elastic constants of the solid.[26] In addition, the density maximum of silica predicted by the Takada is close to the experimental value.[4]

The Takada force field uses a Morse potential to describe the van der Waals interactions so that

	LJ Parameters			Atomic Charges	
$i-j$	A_{ij} (eV)	B_{ij} (Å^{-1})	C_{ij} (Å)	Site i	q_i (e)
Si-Si	0.007695	2.0446	3.7598	Si	1.3
Si-O_b	1.99597	2.6518	1.628	O	-0.65
O-O	0.023272	1.3731	3.791		
Si-O_{SiOH}	0.0458965	2.6598	2.3392	O_{SiOH}	-0.745
H-H	0.000	0.000	0.000	H	0.42
O_{SiOH}-O	0.023272	1.3731	3.791		
O_{SiOH}-H	0.0093589	3.2461	1.1766		

Table 2.7: Parameters for the Takada silica force field.[4] The SiOH subscript denotes a silanol oxygen. The parameters involving the silanol atoms in Si-O_{SiOH} and O_{SiOH}-H are taken from Pedone *et al.*[5]

the site-site interactions are given by

$$V(r_{ij}) = A_{ij}\left[1 - e^{B_{ij}(r_{ij}-C_{ij})}\right]^2 - A_{ij} + \frac{q_i q_j}{r_{ij}}, \tag{2.4}$$

where A_{ij} gives the depth of the interaction, C_{ij} the equilibrium distance for the van der Waals interactions alone, and B_{ij} the range of the Morse potential. The parameters for the Takada force field are given in Table 2.7. Note that the Coulomb interactions are evaluated using a cutoff of 9 Å; see Table 2.3.

2.2.3.6 Modifications to Describe Silanols

The inclusion of silanol groups requires three general modifications of the force fields. The first issue is to maintain charge neutrality of the slab when it is functionalized with hydroxyl groups as described in Sec. 2.2.2. The second modification is the addition of appropriate intramolecular potential terms and constraints to properly describe the structure of the silanol and geminal, $Si(OH)_2$, groups at the surface. A third issue can arise with the force field has site-site interactions that lead to unphysical behavior of the silanols in the presence of the other silica atoms.

The silanol atom charges are determined by requiring charge neutrality for the hydroxylation process illustrated in Fig. 2.2 in which an Si–O–Si group is converted, by addition of H_2O, to two Si–O–H groups.[6, 7] Because H_2O is neutral, the charge of the "reactants" in this process is

$q_{before} = 2q_{Si} + q_O$. The charge after functionalization of the Si–O bond is $q_{after} = 2q_{Si} + 2q_{O_{\mathrm{SiOH}}} + 2q_H$. We have chosen to minimize the atomic charges that are modified upon functionalization so we keep q_{Si} unchanged. Then, requiring $q_{before} = q_{after}$ gives $q_{O_{\mathrm{SiOH}}} = (q_O/2) - q_H$. We choose the hydrogen atom charge to be, $q_H = +0.42$, a value consistent with those used in water models. This then gives $q_{O_{\mathrm{SiOH}}} = (q_O/2) - 0.42$. For example, for the BKS model, $q_O = -1.2$ so this constraint yields $q_{O_{\mathrm{SiOH}}} = -1.02$ as given in Table 2.4.

The intramolecular potential is constructed using harmonic potentials for the bond stretches and angles. In particular, for the Si–O_{SiOH} and O_{SiOH}–H bonds, a stretching potential of the form

$$V_s(r_{ij}) = k_{ij}\,(r_{ij} - r_{ij}^0)^2, \tag{2.5}$$

is used where r_{ij}^0 is the equilibrium bond distance and k_{ij} is twice the force constant. However, in many simulations the vibration of these bonds are not important to the behavior of the silica interface in which case they can be held rigid using an algorithm such as SHAKE.[103] Constraining the O–H bond can also enable a larger timestep in some cases. The Si–O–H angle in silanol groups as well as the O–Si–O angle in geminal units are described by a harmonic bending potential,

$$V(\theta_{ijk}) = k_{ijk}\,(\theta_{ijk} - \theta_{ijk}^0)^2, \tag{2.6}$$

where θ_{ijk}^0 is the equilibrium angle and k_{ijk} is twice the force constant. The flexibility of these angles can be important in investigations of liquids, particularly those capable of hydrogen bonding, in contact with the silica interface. Thus, in Chapter 5 the silanol and geminal angles at the silica-water interface are described using this harmonic potential while the bonds are held rigid. For simplicity in constructing the slab models in the absence of a liquid, as described in Chapters 3 and 4, the SHAKE algorithm was used for both the bonds and angles of the silanols. Nevertheless, we have developed parameters for these intramolecular potentials for use with the BKS, CHIK, ClayFF, and Takada force fields and they are given in Table 2.8. Finally, we note that no torsional potential is used for the geminals, but 1–4 intermolecular interactions – those described by

Stretching		
$i-j$	k_{ij} (eV/Å^2)	r^0_{ij} (Å)
Si–O_{SiOH}	13.5437	1.49670
O_{SiOH}–H	23.9800	0.95000
Bending		
$i-j-k$	k_{ijk} (eV/°)	θ^0_{ijk} (°)
Si–O_{SiOH}-H	8.4124	118.5
O_{SiOH}–Si–O_{SiOH}	13.2095	118.0

Table 2.8: Silanol harmonic stretching and bending potential parameters for use with the BKS, CHIK, ClayFF, and Takada force fields.

Eqs. (2.1), (2.2), and (2.4) – scaled by 0.5, are included.[6, 7]

The final issue that can occur when adding silanols to a silica slab is related to the effect of the interactions with the surrounding pore atoms with the hydroxyl groups. We have found that, particularly for models like BKS with large partial charges, the interactions between the silanol oxygen atoms and silicon atoms can lead to unphysical arrangements of the silanols with respect to the surface atoms, *e.g.*, unrealistically small distances. This occurs primarily in the BKS and CHIK force fields that describe the van der Waals interactions with a Buckingham potential. We have found empirically that small modifications of the Si–O_{SiOH} and O–O_{SiOH} exponent in the Buckingham potential, Eq. (2.1) can avoid this issue. This is the origin of the differences in the b_{ij} term for those interactions compared to the Si–O and O–O ones given in Tables 2.4 and 2.5.

2.3 Water-filled Amorphous Silica Slit Pore Models

A key long-term goal of this work is to use the amorphous silica slab models with varying characteristics to better understand the relationship between the surface properties and experimental measurements of molecules and liquids at the interface. A first step in this direction is presented in Chapter 5 in which the OH reorientation dynamics of water in silica slit pores is investigated.

2.3.1 Generation of a-SiO_2 Slit Pores

Here, we describe the construction of these slit pore models based on the amorphous silica slabs discussed above. The slabs were used to generate slit pores that are filled with water. In concept, the approach is simple. We add water molecules between the two surfaces of one of the functionalized amorphous silica slabs, with periodic boundary conditions, and equilibrate to obtain the correct density of confined water. Our group has previously made use of Grand Canonical Monte Carlo (GCMC) simulations to determine the equilibrium density in roughly cylindrical slit pores,[50] but this can be a computationally slow procedure. Here a different, simpler approach is possible within the slit pore geometry:

1. A silica-water interface is first generated by placing a simulation cell of water molecules with dimensions 21.0155 x 21.0155 x 40.0 Å generated with Packmol[104] in close proximity to each silica interface while avoiding overlapping atoms. The system is then equilibrated with a vapor phase of $\sim$ 50 Å between the water layers for 4 ns in the NP_zAT ensemble. This is followed by a further 2 ns equilibration in the NVT ensemble. A Nosé-Hoover thermostat[105, 106] with a time constant of 1 ps was used to control the temperature while the pressure was maintained at 0.0 atm with a Nosé-Hoover barostat[98] with a damping constant of 1.5 ps.

2. The simulation cell was then reduced in size, eliminating the vapor phase. This was accomplished by deleting water molecules that had any atoms outside a 50 Å region in the z-direction (with the slab near the center of the cell). This generated a roughly 3 nm wide slit pore. The resulting system was then equilibrated for 5 ns in the NP_zAT ensemble to determine the equilibrium density of the slit pore (hence 3 nm is the nominal pore size and each slit pore model has a slightly different z dimension for its simulation cell).

3. Once the simulation cell size is determined by the above procedure, the system was further equilibrated for 1 ns in the NVT ensemble.

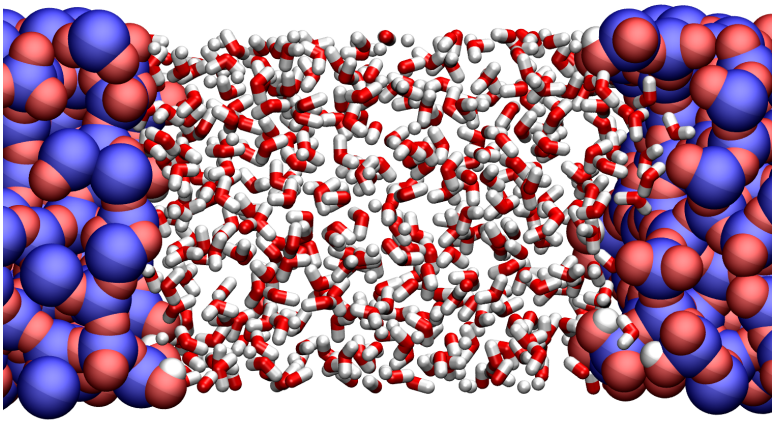

Figure 2.4: Snapshot of a $\sim$ 3 nm wide water-filled amorphous silica slit pore. The silica slab is formed using the BKS potential and has a surface silanol density of 2.26 OH/nm^2. (Si=blue; O=red; H=white)

All slit pore models were generated using molecular dynamics simulations carried out with the LAMMPS code.[98, 99] All slabs have x and y dimensions of 21.0155 Å and were generated with the procedure outlined in Sec. 2.2.3.2 with the BKS force field.[1] However, the interactions with water in this slit pore generation procedure are described by the force field developed by Gulmen and Thompson, described in detail below, for use in simulations of liquids confined within nanoscale silica pores.[6, 7] The water molecules were represented by the SPC/E model.[107]

All simulations used a 1 fs timestep. Water and silanol bonds are held rigid using the SHAKE algorithm[103] with a tolerance of 1×10^{-4}. Lennard-Jones and electrostatic interaction were evaluated with a cutoff of 10.5 and 10.5 Å, respectively; note that the silica framework is held rigid so the short electrostatic cutoff required by the BKS potential is not necessary here. Long-range electrostatic interactions were described using a Particle-Particle-Particle-Mesh approach[108, 109] with a tolerance of 1×10^{-4}. All simulations were run at room temperature with the temperature maintained by a Nosé-Hoover thermostat[105, 106] with a time constant of 1 ps.

A snapshot of one of the slit pores generated with this algorithm is shown in Fig. 2.4. The characteristics of the slit pores and particularly the water confined within them is examined in Chapter 5.

	LJ Parameters		Atomic Charges
Site i	ε_i (kcal/mol)	σ_i (Å)	q_i (e)
Si	0.00010	2.500	1.28
O	0.45686	2.700	-0.64
O_{SiOH}	0.16995	3.070	-0.74
H	0.00037	1.295	0.42

Table 2.9: Parameters for the Gulmen-Thompson force field.[6, 7] The SiOH subscript denotes a silanol oxygen.

2.3.2 Force Field

As noted above, the simulations of water-filled slit pores make use of the Gulmen-Thompson (GT) force field for interactions of silica with liquids.[6, 7] The SPC/E model[107] was utilized for the interactions of water. The GT force field uses a Lennard-Jones potential to describe the van der Waals interactions and has the form

$$V(r_{ij}) = 4\varepsilon_{ij}\left[\left(\frac{\sigma_{ij}}{r_{ij}}\right)^{12} - \left(\frac{\sigma_{ij}}{r_{ij}}\right)^{6}\right] + \frac{q_i q_j}{r_{ij}}, \tag{2.7}$$

which differs slightly from that of ClayFF. The parameters for the GT force field are given in Table 2.9.

A key feature of the Gulmen-Thompson model is that the Si charge is $+1.28$ with the bridging O charge then -0.64. These are notably smaller than those for the BKS force field[1] that is widely used for silica structure and phase behavior and, in fact, smaller than all the other force fields discussed in this Chapter except that of Takada *et al.* With the H atom charge taken to be $+0.42$, the silanol oxygen atoms have a charge of -0.74, which is slightly more negative than the bridging oxygen atoms but less negative than the water O atoms ($q_O = -0.8476$) in the SPC/E model. Note that this force field was designed primarily to describe the interactions of liquids with a silica interface and has been used successfully to model the behavior of liquid structure, dynamics, and spectroscopy in nanoscale silica pores.[7, 51, 52, 54, 55, 110, 111]

In MD simulations of the water-filled slit pores, the SHAKE algorithm[103] was used to hold rigid the Si–O and O–H bonds of the silanol units and the O–H bonds and H–O–H angles of the

	Bending	
$i-j-k$	k_{ijk} (eV/°)	θ^0_{ijk} (°)
$Si–O_{SiOH}–H$	1.0624	118.50
$O_{SiOH}–Si–O_{SiOH}$	1.6546	118.00

Table 2.10: Silanol harmonic bending potential parameters for the Gulmen-Thompson force field used in the simulations in Chapter 5.

water molecules. A harmonic bending potential, Eq. (2.6), was used to describe the silanol bending angles; the bending parameters are given in Table 2.10. No dihedral potential was used for the geminal, $Si(OH)_2$, groups but the intermolecular electrostatic and Lennard-Jones 1–4 interactions, scaled by 0.5, were included.

Chapter 3

Model Amorphous Silica Slabs for Use in Simulations of Dynamics and Catalysis

3.1 Introduction

The properties of a-SiO_2 make it highly attractive in applications to catalysis, where it is widely used as a catalyst support material,[8–12, 17, 112, 113] to separations, where its can serve as a versatile adsorbent,[20, 21] and to drug delivery, where its biocompatibility and chemical tunability are advantageous;[22–24] see Sec. 1.2. Thus, significant effort has been exerted on understanding the properties of amorphous silica (a-SiO_2) as an interface. This has provided a strong impetus for atomistic simulations that can provide insight into the structure of a-SiO_2 and its relationship to the interfacial physical and chemical properties.

As a result, numerous models of amorphous silica have been proposed that range from simple pairwise potentials[1, 2, 4, 6, 25, 27] to density functional theory descriptions.[69, 73, 74] The various approaches have different advantages and disadvantages that generally represent the trade-off between accuracy and computational cost. As discussed in Sec 1.3, none of the descriptions are able to directly model the actual synthetic processes for forming a-SiO_2, as these take at least minutes or hours (not to mention the chemical complexity involved in the wet-synthesis approaches).

The use of amorphous silica in all of the applications mentioned above is based primarily on its interfacial properties. Thus, these have been given special attention in simulation studies, but with models that do not necessarily represent the experimental reality. For example, while most

experiments make use of amorphous silica, either in a planar or a nano-confining geometry, many simulations have made use of a crystalline β-cristobalite surface model.[38–41, 44, 45, 47, 48, 114–118] Amorphous silica slab and pore models are most frequently created by a melt-quench process – melting silica and subsequently quenching it down below its melting temperature at a particular cooling rate – followed by "cutting" atoms to create an interface with the desired geometry. This results in a large number of undercoordinated Si and O atoms that are then saturated by addition of OH and H moieties, respectively. By the nature of the cutting step, this procedure generates relatively flat interfaces, albeit ones that are more disordered than the β-cristobalite surfaces. At present, it is not clear whether these choices have a significant impact on the behavior of the models and their ability to accurately describe experimental measurements.

One of the earliest silica models is the pairwise, fixed charge force field developed by van der Beest, Kramer, and van Santen,[1] (BKS). It has been demonstrated to provide a reasonable description of multiple solid phases of bulk silica.[93, 119, 120] Despite its simplicity, the BKS force field is still regarded one of the better ones available and remains widely used. For example, Cowen and El-Genk explored the accuracy of several force fields[1, 2, 5, 29, 121, 122] in predicting the crystal phases of silica.[58] They found that the BKS potential is the most accurate of the force fields they examined and also has among the lowest computational cost.[58] The BKS force field has also been used as the basis for models that include three-body effects[123] or describe other oxide materiasl such as $ZrSiO_4$ and ZrO_2.[124] BKS has also been used to determine structural features of glass at the densification limit of silica.[125] They explored short-ranged order (coordination), and long-ranged order (distribution of ring structures) and were able to accurately predict the pressure at which the irreversible densification of silica occurs.

These studies motivate the use of the BKS force field as a starting point for understanding the structure of amorphous silica slabs formed with the melt-quench-functionalize method and this is the focus of this Chapter. Additional force fields are considered in Chapter 4 and compared to the BKS results presented here.

Therefore, we employ the BKS potential in developing a large number of a-SiO_2 slabs that

can be used in simulations. We use an approach that does not involve cleaving and show that it provides flexibility in both the density and distribution of silanol groups on the surface. We explore the cooling rate in the quench step and demonstrate that it represents a route to generate silica slabs of varying roughness[126] – a key variable that is largely absent in the models derived using the methods outlined in Sec 2.2.1 and one that is significantly understudied. (The 2,000 *a*-SiO_2 slabs generated in the study, each characterized in terms of defects, rings, silanol density, silanol distribution, and surface roughness.)

3.2 Computational Methods

The melt-quench-functionalize method is used with the BKS force field. The procedure for slab generation can be found in Chapter 2 Sec. 2.2.1, and the functionalization procedure in Sec. 2.2.2. Multiple cooling rates are used (Tab. 2.1). The force field parameters are specified in Sec. 2.2.3.

3.3 Results & Discussion

In this Section, we present the results from analyzing the amorphous silica slabs, and to a lesser extent bulk silica, that are generated according to the procedures described in Sec. 2.1. The aim is to understand in detail the features of the resulting models and the effect of the simulation parameters, especially cooling rate. Thus, we thoroughly characterize the generated slabs in terms of their geometric properties, coordination defects, ring structures, and surface roughness.

In all, we have generated 2,000 amorphous silica slab samples. Specifically, we have generated 100 slabs for each of twenty cases; errors in the results presented represent 95% confidence intervals based on the Student's *t*-distribution[127] using block averaging with ten blocks of 10 slabs each. We have used five different cooling rates in quenching molten silica to the amorphous solid, 1, 5, 25, 100, and 1000 K/ps, two target silanol densities, 2 and 4 OH/nm^2, and two methods of functionalization, stretched and random Si–O bond selection. It is these properties that we now discuss.

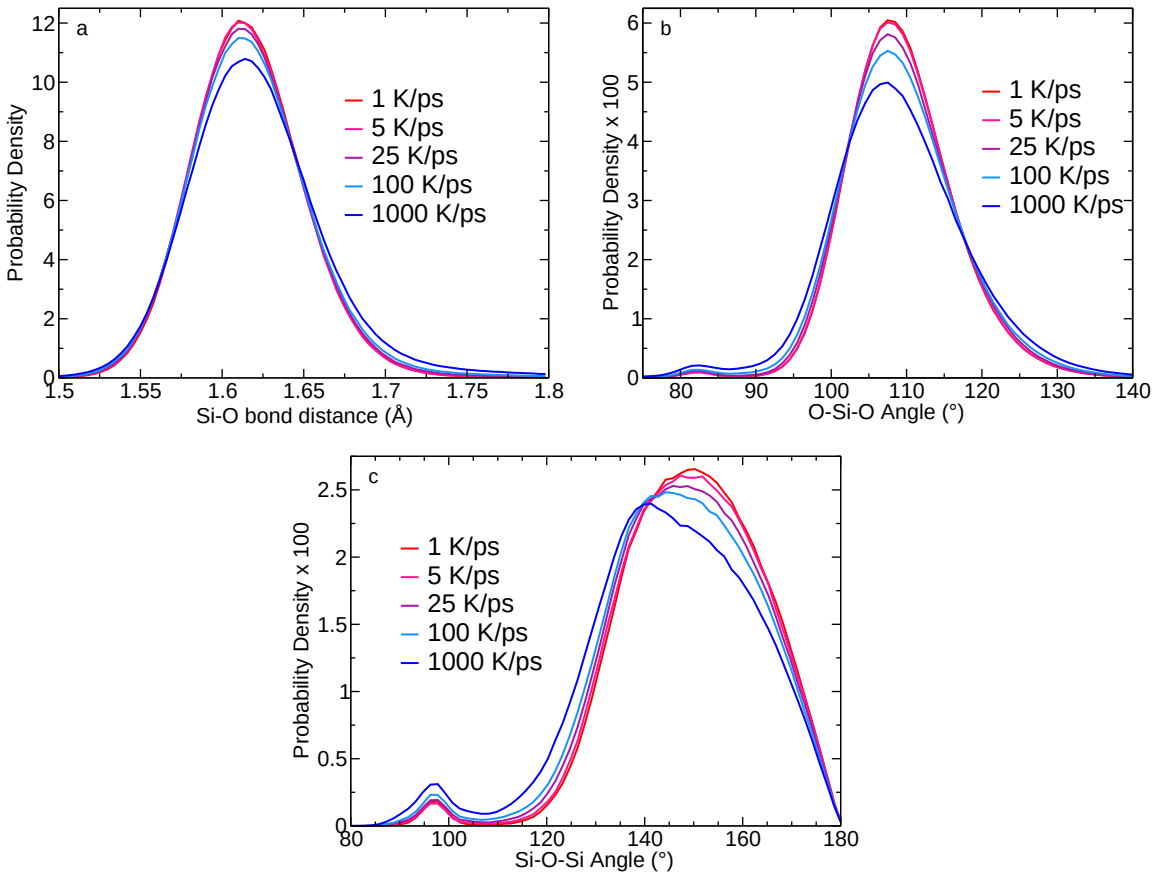

Figure 3.1: Distributions for the (a) Si–O bond distance, (b) O–Si–O angle, and (c) Si–O–Si angle distributions for the functionalized slabs generated with the strained Si–O method with a silanol density of 2 OH/nm^2

3.3.1 Bond Distance and Angle Distributions

We first examine the most basic elements of the silica structure as represented by bond and angle distributions. Specifically, we have calculated the distribution of Si–O bond distances, Si–O–Si angles, and O–Si–O angles and these are plotted in Fig. 3.1 for each of the five cooling rates; bonds and angles were calculated only for Si–O pairs that were within the 2.2 Å distance that is the position of the first minimum in the corresponding radial distribution function. The average for the bond distance and each angle is listed in Table 3.1. This analysis was carried out in order to understand the silica structure within the functionalized slabs and thus the silanol oxygens were not included in the calculations. The results are not sensitive to the functionalization method so results are only presented for the 2 OH/nm^2 surfaces which were functionalized by selecting strained Si–O

Cooling Rate	1	5	25	100	1000	Experimental
Si–O (Å)	1.6158_4	1.6160_3	1.6170_4	1.6184_2	1.6223_4	1.62[a]
O–Si–O (°)	109.324_9	109.324_4	109.300_7	109.273_9	109.19_1	109.4,[b] 109.5,[a] 109.7[c]
Si–O–Si (°)	149.5_2	149.2_1	148.3_2	147.4_2	145.1_2	144,[a,c] 153,[b] 152[c]

[a]Ref. [128] [b]Ref. [129] [c]Ref. [130]

Table 3.1: Average values of the bond and angles obtained from the distributions calculated for 2 OH/nm^2 functionalized silica surfaces (strained Si–O method) for different cooling rates (in K/ps) compared to experimental values reported in the literature. Subscripts indicate 95% confidence intervals in the trailing digit(s).

bonds.

The distribution of Si–O bond distances is only weakly affected by the cooling rate, as can be seen from Fig. 3.1a. The distribution becomes slightly broader as the cooling rate is increased, suggestive of increasing disorder. However, the peak position is shifted, though not substantially, to longer distances and the average bond distance changes by less than 0.01 Å between the fastest and slowest cooling rates (Table 3.1). For all cooling rates, the average Si–O bond distance is in excellent agreement with the experimental value of 1.62 Å. The broadening is more prominent for longer bond distances, suggesting a greater proportion of weak Si-O bonding in surfaces generated with faster cooling rates.

The distribution of O–Si–O angles is plotted in Fig. 3.1b and displays a bimodal behavior. The dominant peak is centered around 109°, consistent with a tetrahedral coordination structure, but a small peak is also found near 82°. The large peak shifts slightly to smaller angles as the cooling rate is increased and broadens modestly. This is reflected in the average angle which decreases by only a little more than 0.1° between the 1 and 1000 K/ps cooling rates; the values are in good agreement with the measured angle of $109.4 - 109.7°$. The magnitude of the smaller peak increases with cooling rate.

The Si–O–Si angle distribution also has a bimodal structure as shown in Fig. 3.1c, but differs substantially from the O–Si–O case. Namely, the dominant part of the distribution peaks at $\sim 140 - 150°$ and is roughly twice as broad as the main peak in the O–Si–O distribution. The minor peak appears around 97°. As with the O–Si–O angle, as the cooling rate is increased the Si–O–Si

angle distribution shifts to smaller angles, but it does so more strongly. At the same time, the smaller peak increases in magnitude.

Slab models developed by from Du and Cormac using a three-body potential have a similar Si–O–Si angle distribution, including a feature at small angles.[131] They also provide evidence that this minor peak is associated with the smaller Si–O–Si angles that occur within strained 2-membered rings (counting by Si atoms). Additionally, they suggested the shifting of the Si–O-Si angle distribution to small angles to be representative of increased populations of 3- and 4-membered rings. This interpretation is consistent with a ring analysis presented in Sec. 3.3.3.

3.3.2 Coordination Number

The coordination structure of the amorphous silica models can also be examined using the pair radial distribution functions (RDFs). The positions of the first and second peaks in the Si–O, Si–Si, and O–O RDFs are given in Table 3.2; plots of the RDFs shown in Fig. 3.2. The peak positions are in good agreement with measured values, with deviations typically less than 0.05 Å and no larger than 0.1 Å. Considering the Si–O RDF, the first peaks of each of the RDFs for the cooling rates occur at the experimental value of 1.62 Å. With increasing cooling rate, modest changes are observed in the silica structure because the peak height decreases. The width of the first peak increases when the cooling rate is increased (Fig. 3.2) which is consistent with all RDFs. The structural changes persist to about 9 Å with the different cooling rates but not further. As noted above, we have used the first minimum to determine the cutoff of 2.2 Å for bonded Si–O pairs. The location of this minimum is essentially independent (Fig. 3.2) of the cooling rate and is consistent with previous studies of both bulk and slab models.[91, 132–134] We now use this cutoff to investigate the distribution of coordination numbers of Si and O atoms in the different silica models, which provide insight into the defects present.[135]

A tetrahedral arrangement of oxygens around a silicon atom is the energetically favorable arrangement making 4-coordinate silicon the dominant species. There is no evidence for a significant fraction of 5-coordinate Si in amorphous silica except at high pressures. Thus such defects

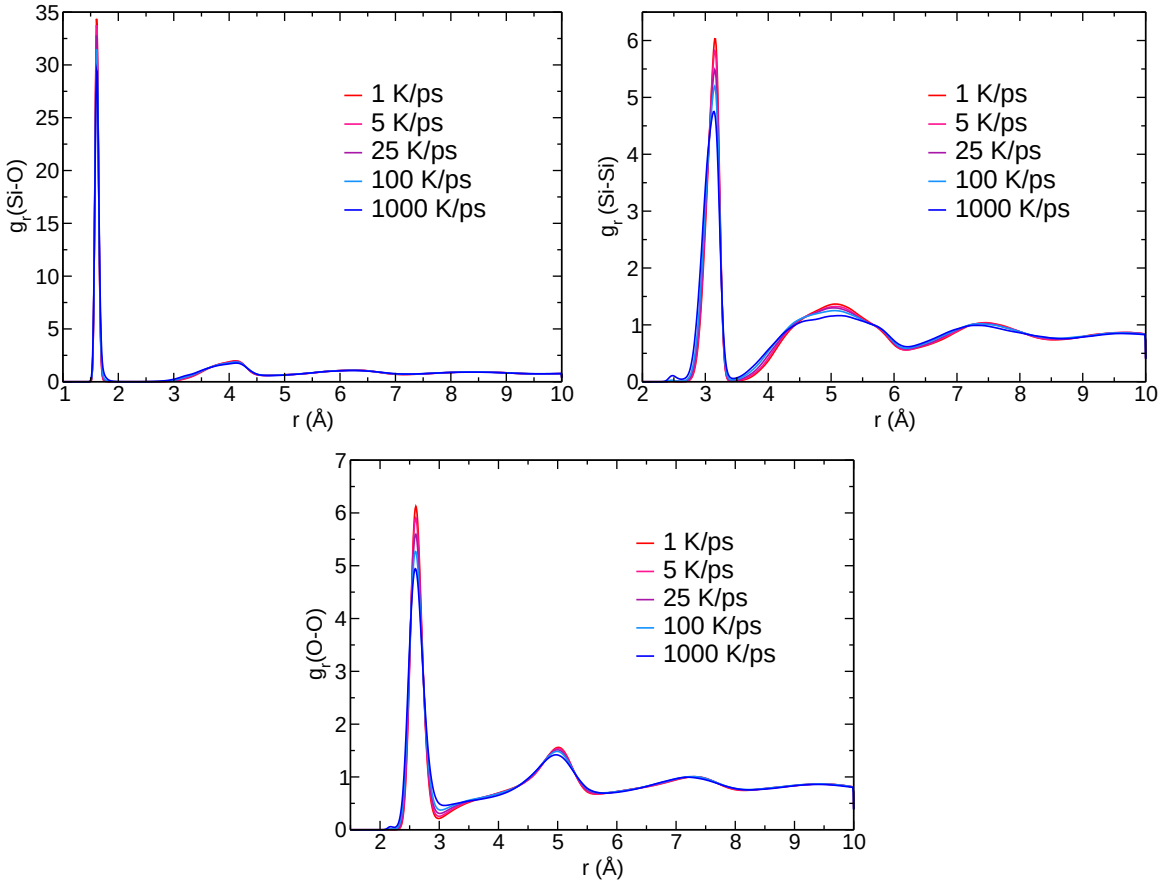

Figure 3.2: Distributions for the (a) Si–O bond distance, (b) O–Si–O angle, and (c) Si–O–Si angle distributions for the functionalized slabs generated with the strained Si–O method with a silanol density of 2 OH/nm^2

	Peak	Simulation		
Si–O	first	1.607	1.620	1.608
	second	4.116	4.15	
O–O	first	2.604	2.65	2.626
	second	5.008	4.95	
Si–Si	first	3.150	3.12	3.077
	second	5.082	5.18	

Table 3.2: Location of the first- and second-nearest neighbor peaks in the pair radial distribution functions for bulk silica.

are generally considered as unrealistic, though their effect on the properties of the silica have not been fully explored.

The fractions of 3-, 4-, and 5-coordinate silicon atoms as a function of the cooling rate are shown in Fig. 3.4 for bulk silica and the 2 OH/nm^2 functionalized slabs. In all cases the slowest cooling rate of 1 K/ps yields few coordination defects, with $\sim$ 99.8% of the Si atoms 4-coordinate and the remainder 5-coordinate. As the cooling rate is increased, the fraction of 4-coordinate Si decreases while the 5-coordinate population increases. The number of 3-coordinate Si atoms is small, less than 0.25%, for all cooling rates. The 1000 K/ps cooling rate results in approximately 4-5 Si atoms in each sample in a 5-coordinate environment.

The 5-coordinate Si atoms are found predominately in the interior of the slabs rather than at the surface. One example is shown in Fig. 3.3. Such defect sites occurring on the surface can lead to an artificially reactive slab, which is not realistic. Although we have discussed the formation of 5-coordinate defect sites in BKS slab models, they show up preferentially in the bulk, *i.e.*, away from the slab surface, and therefore the models appear to correctly describe the correct silica coordination state at the interface. Further, the 3-coordinate Si and singly-coordinated O defects are treated by functionalization (See Sec. 2.2.2) when they occur as pairs, reducing the surface defects in the functionalized surface of the slab.

We note that Garofalini and coworkers observed a coordination of >99.5% for slab models generated using a three-body potential.[91] The present results indicate that a comparable fraction of 4-coordinate Si is obtained with the BKS pair potential by using a slower cooling rate or, conversely, defects in melt-quench amorphous silica models may be a result of too rapid cooling.

The results shown in Fig. 3.4b for the slab models are very similar to that for bulk silica, which is in agreement with other simulations.[91, 133, 134]. The key differences are that there are slightly more coordination defects at the slowest cooling rate and slightly fewer at the highest cooling rate. The selection of Si–O bonds for functionalization based on bond length yields a few more 4-coordinate Si than that based on random selection. However, the two approaches are not significantly different.

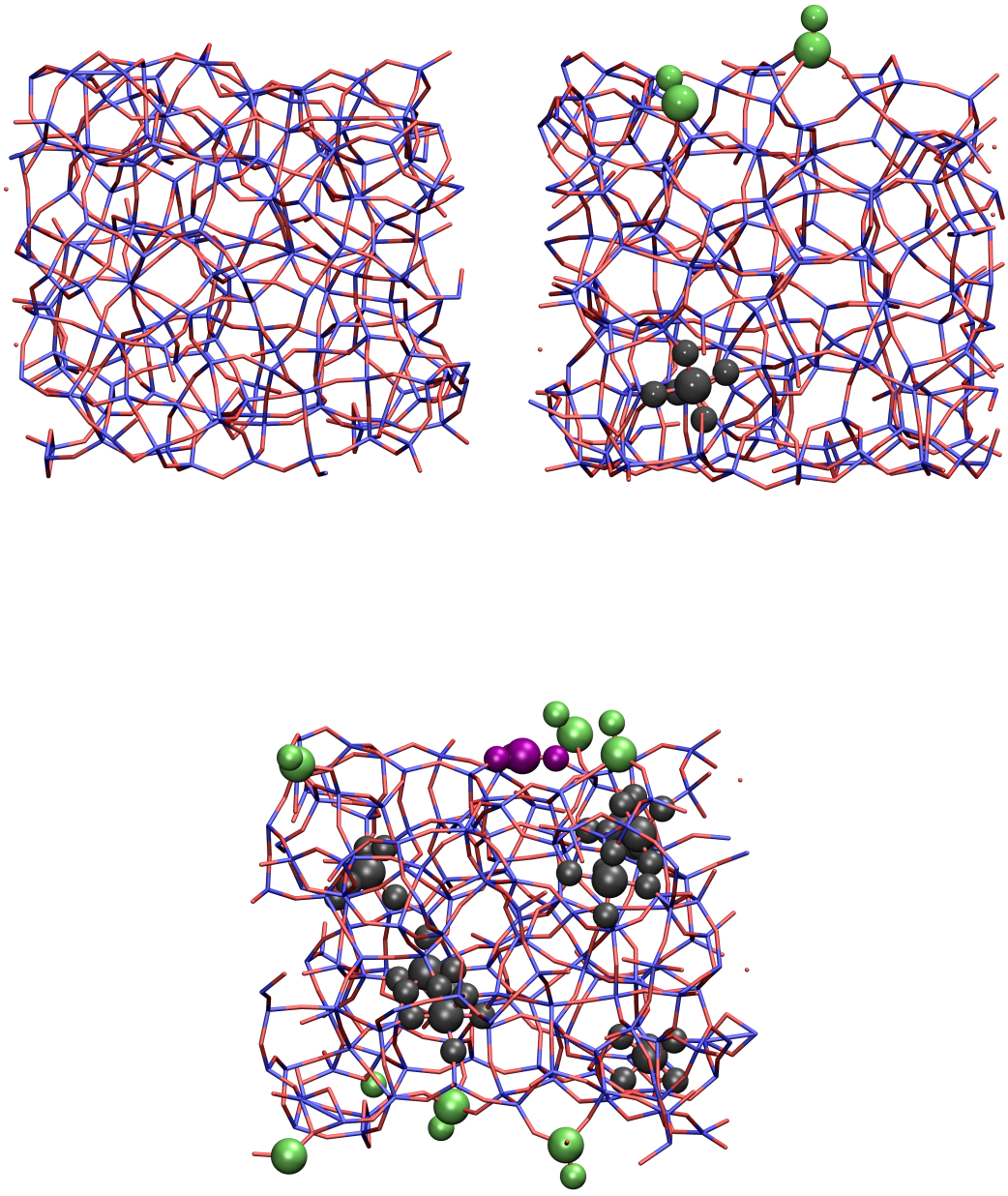

Figure 3.3: Unfunctionalized slab models depicting 5-coordinate Si (grey), 3-coordinate Si (violet), and singly coordinated O (green) defects. The defect-free slab (top left) and low-defect slab (top right) were created with a 1 K/ps cooling rate while the slab with numerous defects (bottom) was generated using a 1000 K/ps cooling rate. Note that there is a distribution of defects and these slabs are not necessarily typical, but rather illustrations of how those defects appear.

The results for oxygen coordination are shown for bulk silica and the 2 OH/nm^2 functionalized slabs in Fig. 3.5. The behavior for bulk silica closely mirrors the Si coordination results in Fig. 3.4a. The dominant arrangement is 2-coordinate oxygen, as expected, with a high fraction, $\sim 99.8\%$, observed at the slowest cooling rate. This fraction decreases to $\sim 97.5\%$ as the cooling rate is increased with a concomitant increase in the 1-coordinate and 3-coordinate O atom fractions. The latter represents the larger defect population and mirrors the behavior of the 5-coordinate Si.

A more significant difference between the bulk and slab results is observed for the O coordination in Fig. 3.5 compared to that for Si coordination. Namely, the minor defect population, 1-coordinate O atoms, increases notably in moving from bulk Si to the slabs. This suggests that the introduction of the interface has a larger effect on the O atom coordination. This is consistent with visualization of the slabs, which indicates that the 5-coordinate Si atoms are primarily found away from the interfaces.

3.3.3 Ring Distribution

Viewing a generated amorphous silica slab as a three-dimensional random network of silicon and oxygen, one can characterize this network by the distribution of ring sizes. This provides additional information about the strain in the local coordination structure of the atoms. As is evident from the angle distributions, particularly that for the Si–O–Si angle shown in Fig. 3.1c, a wide range of ring sizes is present. Note that we define the ring size by an integer n that equals the number of Si atoms in a cycle through Si–O bonds, defined as those with a distance less than 2.205 Å, based on the radial distribution function.

To calculate the 2-membered rings (a ring with two Si atoms and two O atoms) we used a Si–O adjacency matrix which is a matrix with elements equal to 1 (0) for an Si and O pair that are bonded (not bonded). The 2-membered rings are identified by searching the adjacency matrix for any two Si atoms that are bonded to the same two O atoms.

To identify rings with three or more Si atoms ($n = 3 - 7$) in the silica structure, we used the depth first traversal method. This is a recursive algorithm that uses the idea of backtracking.

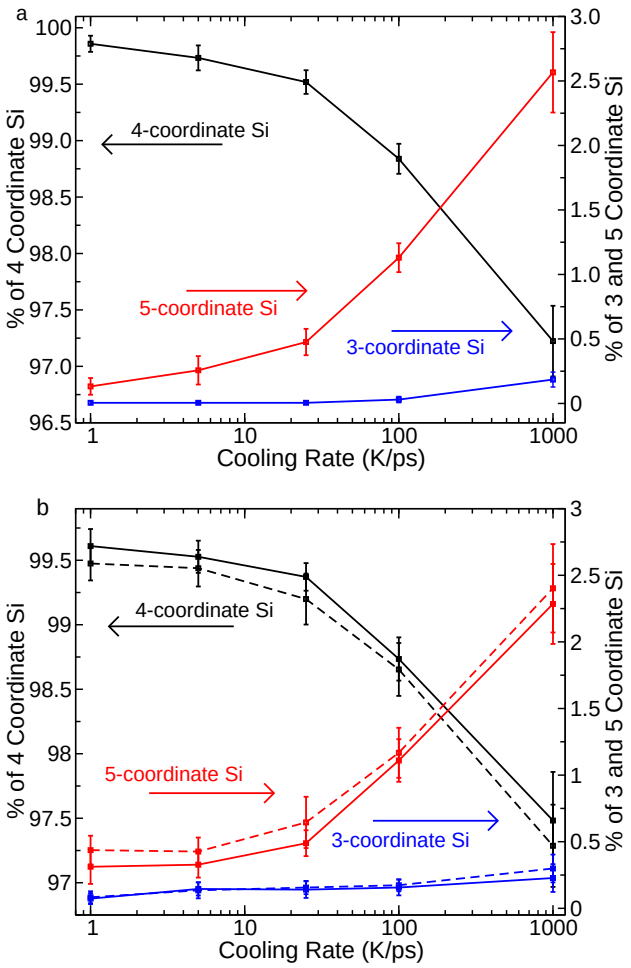

Figure 3.4: Comparison of the coordination of silicon atoms for (a) bulk silica and (b) 2 OH/nm^2 functionalized silica slabs using functionalization based on strained Si-O bond (solid lines) and random Si-O bonds (dashed lines).

Namely, the algorithm starts a traversal at a random Si atom and visits the adjacent Si atoms. An adjacent Si atom is one connected through an Si–O–Si linkage, defined as an edge. Each such Si atom found by the algorithm is marked as visited and the previously visited Si atom on the other end of the linkage is identified as its parent atom. The algorithm continues to traverse through new adjacent Si atoms randomly without revisiting the previously identified linkages. In this process, if an already visited Si atom is found that is not the parent, this represents a cycle and the final linkage is marked as a "back edge." The two Si atoms linked by this back edge are then stored in an array to be used later to calculate the rings. The algorithm continues to search for back edges until all Si atoms have been visited.

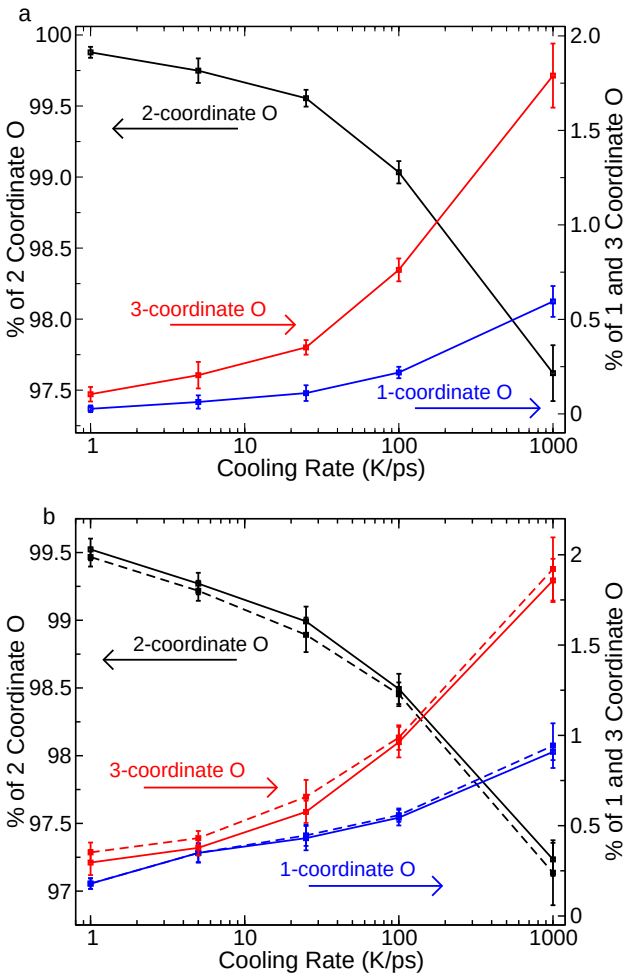

Figure 3.5: Same as Fig. 3.4 but for coordination of oxygen atoms.

When the depth first traversal calculation is completed, the method proposed by Albehairy *et al.* is used to count the rings.[136] This algorithm loops through all the pairs of Si atoms corresponding to back edges and calculates unique rings as follows. The algorithm starts from one of the Si atoms of a back edge and traverses through its adjacent Si atoms until the other Si atom of the back edge is found. The Si atoms along the route together with the two Si atoms of the back edge define a ring. This is repeated for each back edge to calculate all possible rings. Each resulting ring can be primitive or non-primitive, where a primitive ring is one that cannot be decomposed into two or more smaller rings. The rings calculated by this method can have higher-membered non-primitive rings in which one or more primitive rings are embedded; we remove these non-primitive rings.

To provide a simpler measure of the ring structures, we only consider the shortest ring associ-

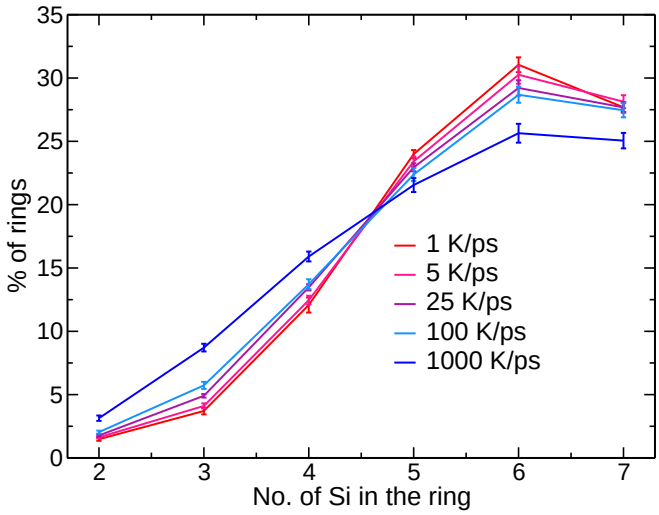

Figure 3.6: Distribution of ring sizes in unfunctionalized silica slabs for different cooling rates.

ated with each O–Si–O linkage. Because each Si atom can have six O–Si–O linkages (assuming the Si atom is 4-coordinate) we find the six shortest primitive rings for each Si atom. This method has two characteristic features. First, this method can include a ring not just once, but several times, in connection with different silicon atomic sites, because the shortest ring picked for one O–Si–O linkage could be the shortest ring for other O–Si–O linkage in the same ring. Hence, in the final step those overlapping rings are also removed to calculate the unique ring count. Second, the distribution decreases rapidly for $n \geq 6$ instead of growing indefinitely with increasing n. This method has been frequently used to characterize the structure of amorphous silica.[137–140]

The ring distributions obtained this way for the unfunctionalized silica slabs are shown in Fig. 3.6 for the five different cooling rates. Independent of cooling rate, the generated slabs contain small membered rings, *i.e.*, 2- and 3-membered rings). This is consistent with the observation of small angle peaks in the Si–O–Si and O–Si–O angle distributions in Fig. 3.1. Also at all cooling rates, 6-membered rings are the dominant population followed by $n = 7$, 5, and then smaller rings in decreasing order of size.

The distribution of rings depends quantitatively on the cooling rate. Increasing the cooling rate leads to fewer 6-membered rings and a larger fraction of strained, 2-, 3-, and 4-membered rings. These rings, particularly the smallest ones can be considered a kind of structural defect, different

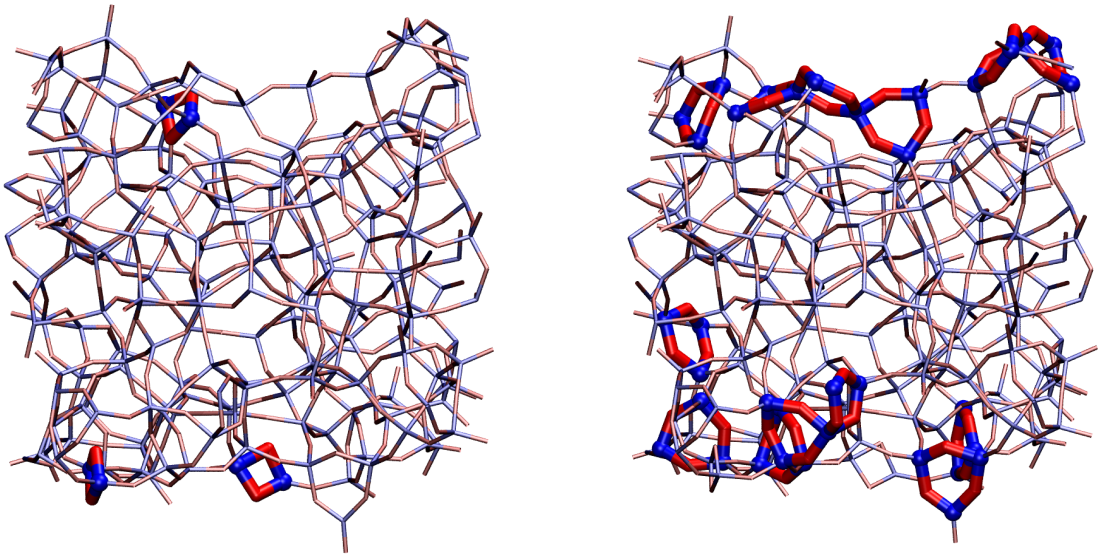

Figure 3.7: An unfunctionalized silica slab structure (wireframe) is shown with the 2-membered (left) and 3-membered (right) rings (ball-and-stick) indicated.

from the coordination defects discussed above, that is intrinsic to a-SiO_2. The results show clearly that the population of the more strained rings can be decreased, but not eliminated, by quenching the silica melt at a slower rate.

It is also interesting to consider the location of the rings (which is also discussed further below). A typical snapshot of an unfunctionalized silica slab is shown in Fig. 3.7 with the 2- and 3-membered ring structures indicated. It is clear from these pictures that these strained ring structures are found primarily at the surface. All of the 2-membered rings have at least one Si atom that is at the slab interface while the majority of 3-membered rings do. This suggests that the appearance of strained rings is induced by the creation of the silica-vapor interface.

Zeitler and Cormack observed that the Si–O bonds in 6-membered rings are the most stable of all rings when reacted with a water molecule.[141] This suggests that slabs generated with the faster cooling rates show a reactivity of the surface that will not be present in slabs of the slower cooling rates.

3.3.4 Density

We now turn to an examination of the silica density within the slab models. This mass density is plotted as a function of the position along the z-coordinate, defined as the surface normal, in Fig. 3.8. The density is obtained by binning atoms (in 1 Å increments) by their value of z and dividing the total mass present in each bin by the bin volume.

We find that the average density in the center of the slab is approximately 2.25 g/cm^3 and is effectively independent of cooling rate. This is in good agreement with the measured density of 2.2 g/cm^3 for a-SiO_2. Except for the highest cooling rate, the density is not uniform across the slab and it is found to increase as the silica-vapor interface is approached. This densification at the slab surfaces appears to increase as the cooling rate is slowed. Comparing Figs. 3.6 and 3.8 suggests that this behavior may be associated with the presence of different ring structures. In addition, the 1000 K/ps cooling rate gives rise to a broader interface as indicated by the slower decrease in density toward larger $|z|$ values. These results suggest that higher cooling rates prevent the densification of the silica at the interface, but it is important to note that this greater interface width for the fast cooling rate may be a consequence of increased surface roughness, which is examined in detail in Sec. 3.3.5.

The density of atoms involved in 2-membered rings is also shown in Fig. 3.8a. This shows quantitatively the same result illustrated in Fig. 3.7. Namely, these strained rings occur almost exclusively at the surface of the silica slabs. Only for the fastest cooling rate is there any significant population of 2-membered rings in the slab interior.

Similarly, Fig. 3.8b shows the density of 3-membered ring atoms as a function of z. These rings show a preference for the silica interface at all cooling rates. However, they are also found in the slab interior with a lower density. The overall density increases with cooling rate, consistent with the averaged 3-membered ring population in Fig. 3.6. The density associated with 3-membered rings grows more quickly in the slab interior than at the interface when the rate of cooling is accelerated. Thus, while we see a preference for positions at the interface for the two smallest ring structures, this behavior depends on the ring size with the more strained, 2-membered rings more

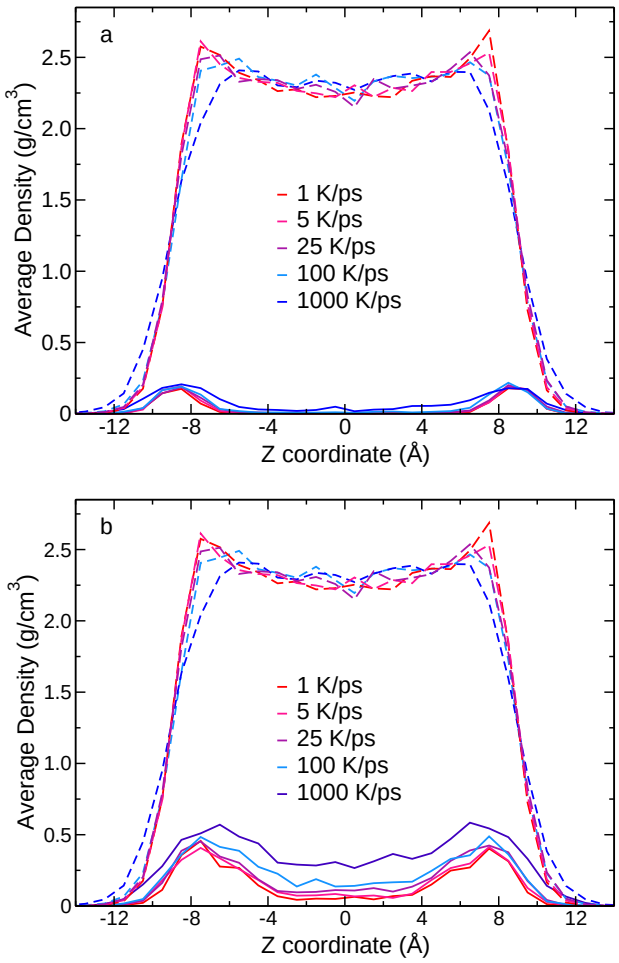

Figure 3.8: The total density of unfunctionalized silica slabs is plotted as a function of the z-coordinate in the direction of the nominal surface normal. The densities that correspond to atoms in (a) 2-membered and (b) 3-membered rings are also shown.

strongly partitioned to the surface.

3.3.5 Surface Roughness

One area in which little remains known relates to the atomistic surface roughness of amorphous silica and its impact on the interfacial properties. It is possible, even likely, that the roughness depends on the synthetic method, but systematic studies are absent. From the modeling side, the issue has attracted limited attention.[110] A large number of simulation studies have used crystalline models, such as α-quartz[67, 68] or β-cristobalite,[38–41, 44, 45, 47, 48, 114–118]

that are atomically smooth. In addition, models of amorphous silica have frequently been based on "cutting" an solid sample and then saturating the resulting undercoordinated atoms, a procedure that also leads to a comparatively flat interface.

Some insight into how surface roughness can impact liquids at the silica interface is offered by vibrational sum-frequency generation (SFG) measurements that compare amorphous silica and crystalline quartz interfaces. Specifically, Shen and co-workers observed significant differences in the SFG spectra at the water/fused silica and water/(0001) quartz interfaces with this surface-sensitive technique.[86, 142] This indicates that, at a minimum, the water structure next to the two surfaces is different. It is not clear if this is related to surface roughness or other atomistic details, *e.g.*, silanol density or distribution.

Research in the Thompson group, in collaboration with Prof. Damien Laage, has previously examined the OH reorientation dynamics of water in ~ 2.4 nm diameter roughly cylindrical a-SiO_2 pores.[52, 110] We found that the dynamics are dramatically slowed relative to bulk water and exhibit a long-time decay out to ~ 1 ns that is best described by a power law. The reorientation dynamics can be directly related to that for exchanging hydrogen-bond (H-bond) partners[143, 144] and we mapped this exchange time to the local topology of the pore surface.[110] The results showed that faster H-bond exchanges were observed near regions of the silica surface which protruded out into the pore and substantially slowed dynamics were found for water molecules in recesses within the pore wall. Hence, the H-bond and reorientation dynamics are strongly affected by the surface structure and particularly the roughness.

These results motivated one objective of this work: To investigate whether a-SiO_2 slabs with varying surface roughness can be generated. The approach is based on the hypothesis that the cooling rate modulates the roughness, with slower rates giving rise to smoother surfaces and faster rates preventing the relaxation of the surface. We now examine this prediction.

We have used two methods to characterize the atomistic surface roughness of the generated silica slabs. First, we calculated the root mean-squared deviation (RMSD) of the surface atoms from a plane determined by fitting to their positions (to avoid including the presence of a slope of

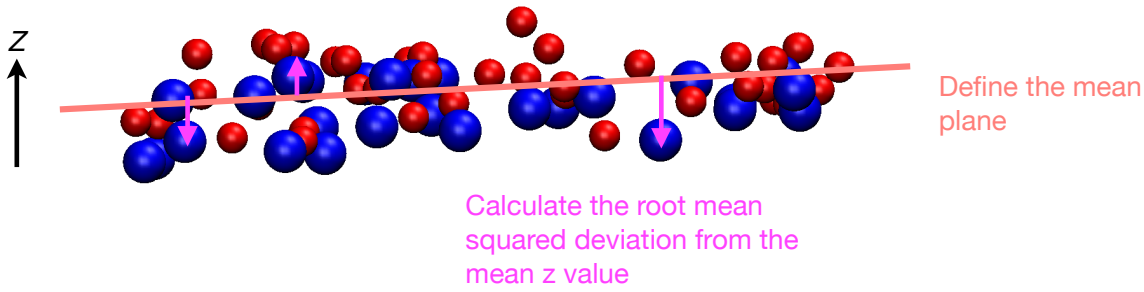

Figure 3.9: Schematic illustration of the root mean-squared deviation calculation of surface roughness.

the surface in the calculation). The surface atoms are fit to a plane (Fig. 3.9) of the form,

$$z_p = ax + by + c, \tag{3.1}$$

where a, b, and c are constants. The RMSD is then calculated as,

$$RMSD = \sqrt{\frac{1}{N}\sum_{i}^{N}(z_p(x_i, y_i) - z_i)^2}, \tag{3.2}$$

where N is the number of surface atoms and x_i, y_i, and z_i are the Cartesian coordinates of the i^{th} surface atom. The calculation was carried out on each slab model and was averaged, and the error is reported to 95% confidence interval.

Second, we calculated the solvent-accessible surface area (SASA) using the FreeSASA[145] code, and calculated the excess SASA by subtracting the $x-y$ cross-sectional area. The FreeSASA code calculates the area of all six sides of the slab model so we carried out an additional calculation of the slab replicated multiple times in x and y direction so that we could algebraically solve for the average SASA of only the top and bottom surfaces. The six faces of the slab are divided into three types, a, b, and c as shown in Fig. 3.10. Our goal is to solve for c, and one can do that with,

$$c = \frac{C_2 - C_1}{12}. \tag{3.3}$$

where C_1 is the solvent-accessible surface area obtained for the slab alone (left side of Fig. 3.10)

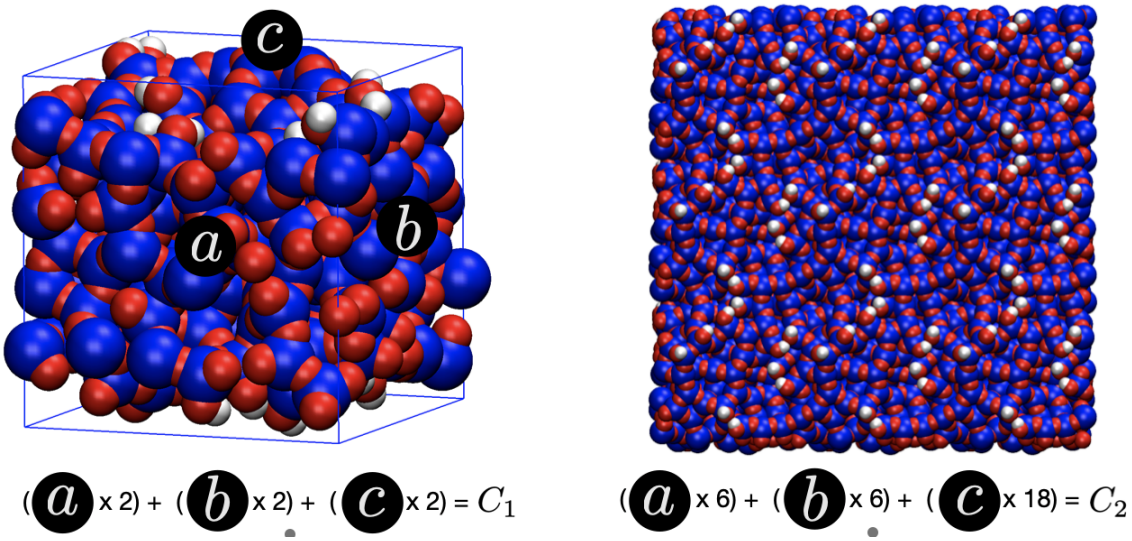

Figure 3.10: Schematic illustration of the free solvent-accessible surface area calculation of surface roughness.

and C_2 is the SASA obtained for the replicated slab (right side of Fig. 3.10). The factor of 12 comes from multiplying the equation on the left of Fig. 3.10 by six to solve for c. The error is reported as 95% confidence intervals from ten blocks, each containing ten slabs.

Individual roughness calculations for the two methods of functionalization in each roughness measure are shown in Fig. 3.11. In both cases, the RMSD and the free SASA increase with cooling rate, which was expected. It is clear that the silanol distribution on the surface of the slab does not affect the roughness of the surface for the most part, but rather it arises primarily from the cooling rate. The free SASA distributions resulting from the two functionalization procedures for the 5 K/ps result shows two distinct populations although it is not reflected in the RMSD result.

The results from these two methods are plotted as a function of cooling rate in Fig. 3.12, where the vertical scales have been chosen to match the values at the fastest (1000 K/ps) and slowest (1 K/ps) rates. The results show a consistent trend toward greater roughness as the cooling rate is increased. At the slower cooling rates, the change is more gradual before a significant increase in roughness between 100 and 1000 K/ps. Interestingly, both methods for determining the surface roughness give quantitatively similar results when scaled to match at the highest and lowest cooling rates.

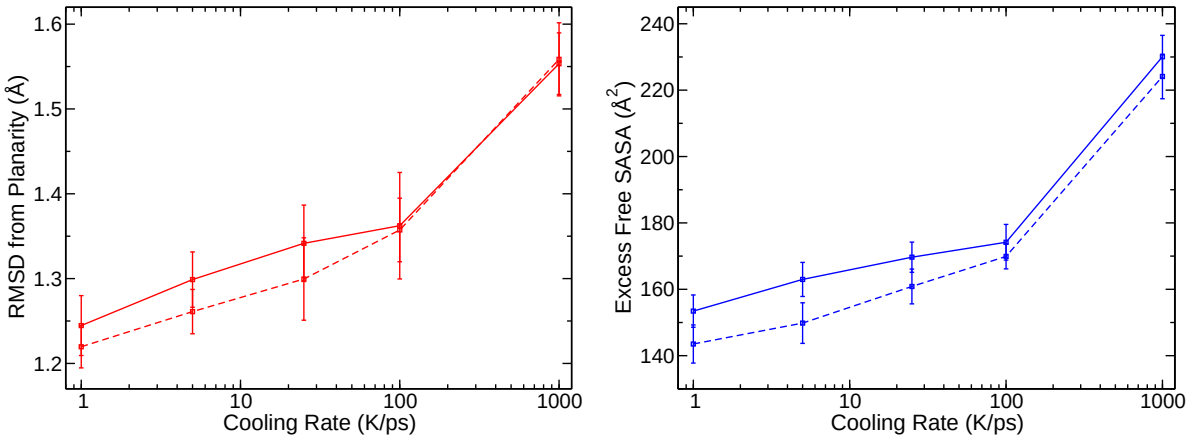

Figure 3.11: Resulting surface roughness measurements. (blue) RMSD from planarity, (red) free SASA calculations from slab models functionalized to 2 OH/nm^2 with strained Si–O method (solid lines), and random Si–O method (dashed lines).

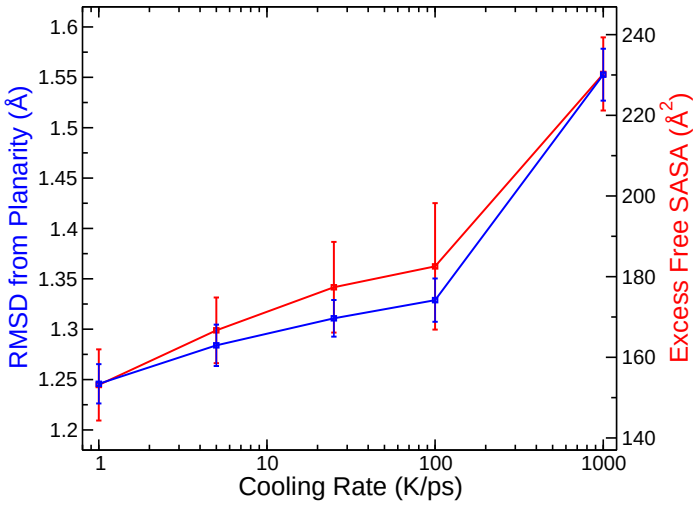

Figure 3.12: Comparison of the RMSD of surface atoms from planarity and the excess solvent-accessible surface area (SASA) for functionalized slabs generated with the strained Si–O method with a silanol density of 2 OH/nm^2. Error bars indicate one standard deviation of the result over 100 slabs.

The data in Fig. 3.12 clearly indicate that the surface roughness can be modulated in the melt-quench procedure by changing the cooling rate. This trend in the roughness with cooling rate is generally consistent with the behavior of the slab mass density profiles in Fig. 3.8. It is important to note, however, that these changes in surface roughness are accompanied by shifts in defect density and ring structure so that these cannot be considered as separate variables in the present approach.

3.4 Conclusion

We have presented a detailed investigation of a melt-quench method to generating amorphous silica slabs with varying properties. The approach was implemented to generate slabs using different cooling rates between 1 and 1000 K/ps during the quench and varying surface hydroxyl densities and distributions based on an *ad hoc* functionalization method. We have thoroughly characterized the resulting 2,000 silica slab models constructed using the BKS pairwise force field. The results show a clear effect of the cooling rate on the *a*-SiO_2 slab characteristics, though the quantitative behavior varies between different properties.

The characterization of the local geometric features, Si–O bond distance and Si–O–Si and O–Si–O angles, demonstrates excellent agreement with available experimental data. The results show modest effects of the cooling rate on these properties indicative of greater heterogeneity with faster quenching. The Si and O atom coordination numbers indicate a stronger effect of cooling rate, with increases in 5-coordinate Si and 3-coordinate O with more rapid cooling. The results show that these defects can be effectively annealed out of the structures for sufficiently slow cooling.

Examination of the distribution of rings in the silica structure also shows increased defects, in this case small, strained rings, with faster cooling rate. In contrast to the coordination defects, however, the most strained, 2-membered rings are found almost exclusively at the slab interface. The 3-membered ring population is predominantly localized at the slab interface, but with a broader distribution that extends over the full width of the slab.

Of particular interest is the surface roughness of the generated slabs. We have demonstrated that the the cooling rate modulates the atomic scale roughness of the slab surface, which can

have important implications for the interfacial dynamics.[52, 86, 110, 142] Thus, the silica slab models generated in this work can be used to prove the effect of surface roughness on measurable interfacial properties of silica. At present, little is understood about the roughness of *a*-SiO_2, its dependence on synthesis method, and its implications for chemistry in applications such as catalysis.

Insights into the structure of silica materials and the resulting reactivity can be challenging to determine experimentally. Thus, molecular simulation can play an important role in elucidating the underlying structure-function relationships for amorphous silica. The work presented here should assist these efforts through the development of a library of atomistic *a*-SiO_2 models that have been characterized in detail, are consistent withe experimental measurements, and can be readily implemented in simulations. The slabs vary in silanol concentration, silanol distributions, coordination and ring defect densities, and surface roughness.

Chapter 4

Comparison of Fixed-Charge Force Fields for the Generation of Amorphous Silica Slab Models

4.1 Introduction

The wide range of practical applications for amorphous silica (a-SiO_2), discussed in Sec. 1.2), has naturally led to the development of a large number of force fields for describing it. The simplest of these force fields use a fixed-charge description of the electrostatics balanced by shorter range van der Waals interactions. While these are not able to describe reactive processes (outside of rearrangements within the solid) they have the advantage that they are computationally inexpensive and can thus be used to model long timescale dynamics of silica itself, *e.g.* phase transformations, or its interaction with fluids. These force fields are typically parameterized based on a set of experimentally measured properties and vary in both the elements of that set as well as the form assumed for the interatomic silica interactions. The primary focus of these force fields has been the correct description of the different phases of bulk silica.

In this study we instead investigate the characteristics obtained for amorphous silica slab models that can be used in simulations of silica-supported catalysts and silica-fluid interfaces. We examine three force fields, in addition to the BKS model discussed in detail in Chapter 3, that vary in both the form of the potential used and the quantitative balance between electrostatic and van der Waals interactions. Specifically, we consider the Carré, Horbach, Ispas, Kob (CHIK),[2] ClayFF,[3] and Takada[4] force fields that are described in detail in Secs. 2.2.3.3, 2.2.3.4, and 2.2.3.5, respectively. We focus on the structural features, including coordination defects and ring

distributions, generated with each of these force fields using the melt-quench-functionalize procedure outlined in Chapter 2.

4.2 Computational Methods

The force fields of interest of this study, as well as the methodology used to generate slab models with each force field is described in Sec. 2.2.3. The procedure of both bulk and slab generation has been outlined in Sec. 2.2.1.

4.3 Results & Discussion

In this Section we present the results of an analysis of both the amorphous silica bulk and the slabs generated. The primary aim is to understand the properties that differ between the different force fields used in this study. It is important to point out the similarities and differences of these force fields. The CHIK and ClayFF models have similar charge schemes (see Tables 2.5 and 2.6) with charges that are significantly larger in magnitude that those used in the Takada (Table 2.7) force field. Thus, Takada is generally considered to be a "soft" potential whereas CHIK and ClayFF are "hard" potentials; not that BKS, which has the largest charges of all the models considered (Table 2.4), also falls into the latter category. The van der Waals contribution to the potentials are represented by a different functional form in all the force fields except CHIK and BKS. However, there is no clear metric to determine *a priori* if one force field is a better description of "real" silica than another. Thus, comparisons of the amorphous silica slab models generated here are aimed at developing a better understanding of the consequences of these differences in the force field in the bulk and slab characteristics.

With each force field, we have generated 20 bulk models and 20 slab models. The latter have a hydroxyl density of 2 OH/nm^2; the slabs are functionalized using the strained Si–O bond criterion, described in Sec. 2.2.2, until the required silanol density is reached. The cooling rate of 1 K/ps was used in all cases to generate models that have fewer coordination defects.

4.3.1 Bulk a-SiO_2 Models

4.3.1.1 Radial Distribution Function (RDFs)

The radial distribution function (RDF) is a measure of relative arrangement of the atoms in the amorphous solid. In Fig. 4.1 the RDFs for the bulk samples obtained with each force field are shown. Considering the Si–O RDF first, we see that there are clear differences between the ClayFF result and those for the other force fields. Specifically, the first peak in the RDF is shifted to smaller distances, less than ~ 1.55 Å, compared to the other models. Experimentally, the peak position for the Si-O RDF falls at 1.62 Å,[128] and thus, unlike the other three force fields, ClayFF fails to agree with experiment in this feature.

The Si–O RDF of the CHIK, BKS, and Takada force fields are in good agreement with each other; only slight differences observed in the first peak position and height. ClayFF also predicts a shorter distance for the second peak in the RDF near 4 Å, nearly 0.5 Å smaller than that found for the other three models. At Si–O distances greater than ~ 4.5 Å, the RDFs of all four force fields are nearly indistinguishable.

The same general behavior is observed for the Si–Si and O–O RDFs in Fig. 4.1b,c. Namely, ClayFF predicts more tightly structured silica with the first and second peaks occurring at smaller positions and with narrower widths than the other force fields. The CHIK and BKS models are in good agreement with one another while Takada predicts smaller peak heights and slightly longer peak positions for the first and second peaks of both the Si–Si and O–O RDFs.

4.3.1.2 Bond Distance and Angle Distributions

Further characterization was carried out by calculating the bond and angle distributions for the bulk silica models generated with the three force fields, which are shown in Fig. 4.2. BKS results for 20 bulk samples are also presented for comparison. Average values for each case were calculated and are given in Table 4.1.

Considering first the Si–O bond distance, we can see from Fig. 4.2a and Table 4.2 that the BKS,

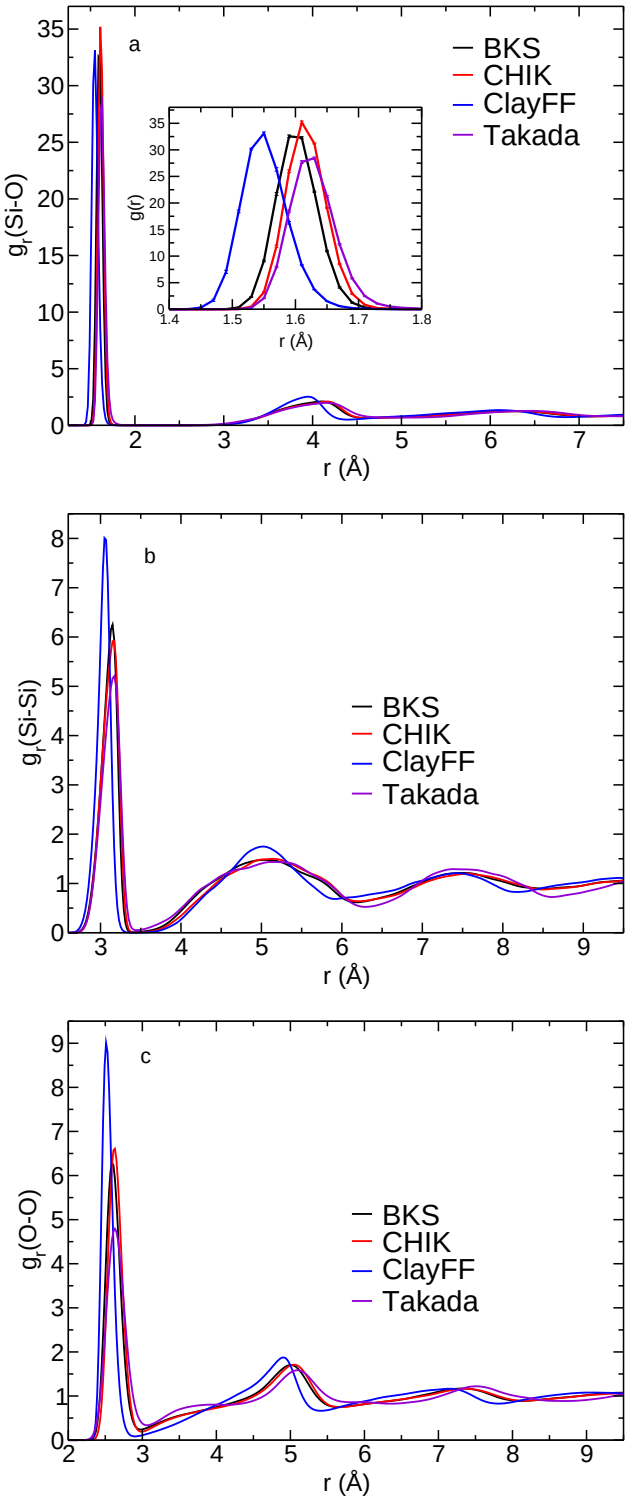

Figure 4.1: Pair radial distribution functions for bulk amorphous silica obtained using the four force fields considered in this study. Results are shown for the (a) Si–O, (b) Si–Si, and (c) O–O RDFs.

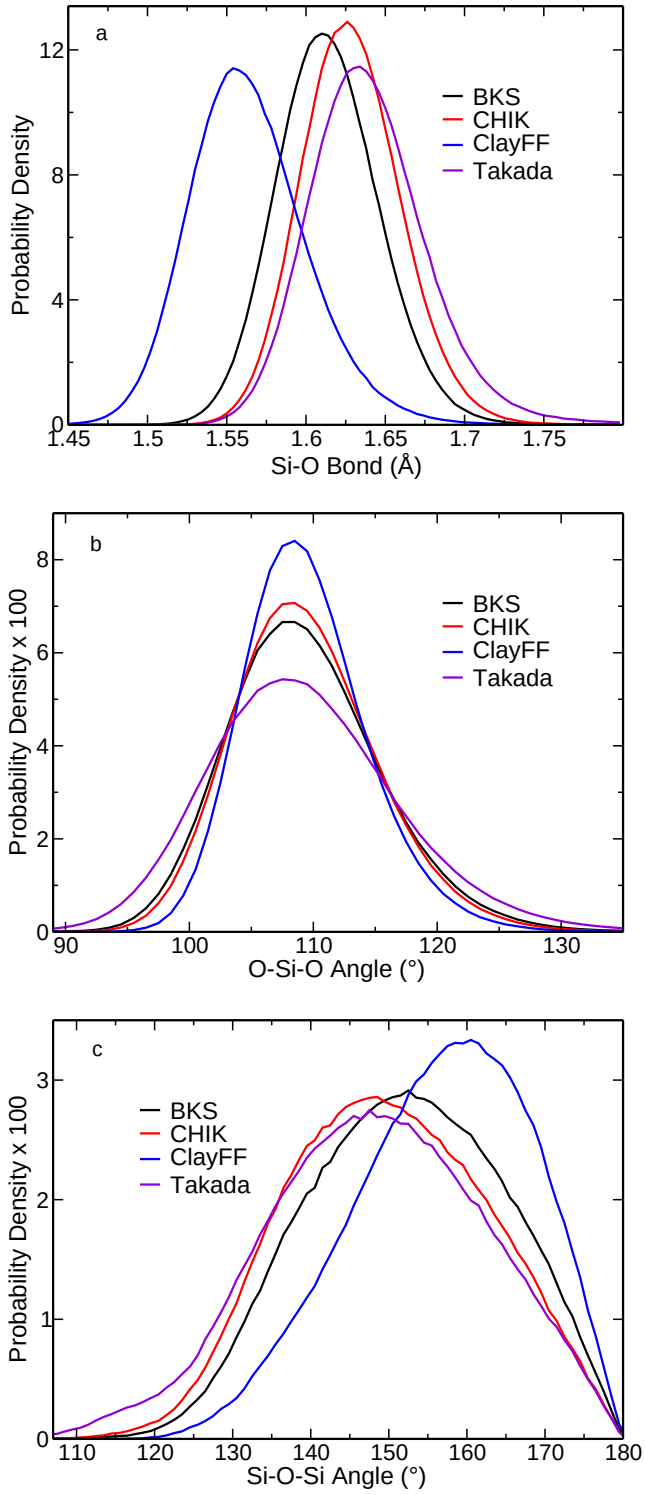

Figure 4.2: Distributions for the (a) Si–O bond distance, (b) O–Si–O angle, and (c) Si–O–Si angle for bulk silica generated with different force fields.

Force Field	BKS	CHIK	ClayFF	Takada	Experimental
Si–O (Å)	1.6140_2	1.6287_1	1.5639_3	1.6401_3	1.62[a]
O–Si–O (°)	109.382_5	109.398_6	109.44_1	109.32_1	109.4,[b] 109.5,[a] 109.7[c]
Si–O–Si (°)	152.0_3	149.6_1	156.5_3	148.1_2	144,[a,c] 153,[b] 152[c]

[a]Ref. [128] [b]Ref. [129] [c]Ref. [130]

Table 4.1: Averages of the distributions for bulk silica with different force fields. Experimental values have also been included for comparison. Subscripts indicate 95% confidence intervals in the trailing digit(s).

CHIK, and Takada force fields all give an average bond distance in good agreement with the 1.62 Å experimental value.[128] While the first two give a result within 0.01 Å of the measurements, Takada predicts an average Si–O bond distance that is just ~ 0.02 Å too long. However, ClayFF much more significantly underestimates, by ~ 0.06 Å, the average bond distance.

Examining the angle distributions we see from Fig. 4.2b that similar O–Si–O bond angles are predicted by all four force fields, in good agreement with the measured values.[128–130] The range of O–Si–O angles found in the silica models do vary, however, with ClayFF and Takada predicting narrower and broader distributions, respectively. The Si–O–Si angle distribution is significantly broader than that for the O–Si–O angle[128–130] and this is reflected in the results for all four force fields presented in Fig. 4.2c. As with the other structural measures, ClayFF gives an Si–O–Si angle distribution that is narrower than that predicted by the other force fields, indicative of a more tightly structured silica framework. The other three force fields are in general accord, with BKS showing a small shift to larger Si–O–Si angles and Takada giving a slightly longer tail to small angles.

Overall, these measures of the local (bond and angle) silica structure indicate that ClayFF, which was designed for the simulation of hydrated and multicomponent mineral systems including, but not limited to, silica, is not as accurate in reproducing experimental benchmarks within the present melt-quench simulations of bulk a-SiO_2. The other three force fields are in general agreement with each other and measurements and thus all appear to be viable descriptions of a-SiO_2.

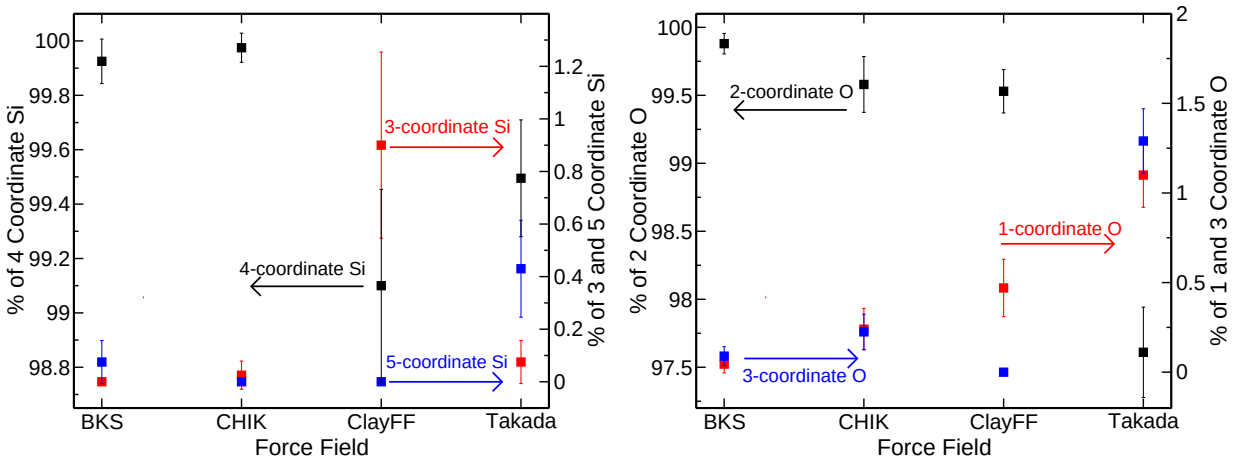

Figure 4.3: Percentage of Si atoms (left)) and O atoms (right) with different coordination numbers in bulk a-SiO_2 generated with the different force fields. Results are averaged over 20 slabs for each case and the error bars represent the standard deviation within this set.

4.3.1.3 Coordination Number

The coordination numbers for Si and O atoms in bulk silica were determined using an Si–O bond distance cutoff of 2.2 Å, and the results obtained for the bulk silica samples are presented in Fig. 4.3. The BKS an CHIK force fields both generate bulk silica models with >99.8% of the Si atoms four-coordinate an $>$ 99.5% of the O atoms two-coordinate. In contrast, the ClayFF and Takada force fields yield significantly more coordination defects. ClayFF gives silica models with the largest fraction of three-coordinate Si atoms, nearly 1%, but no five-coordinate Si atoms. Takada, on the other hand, produces more than 0.4% five-coordinate, but less than 0.1% three-coordinate, Si atoms. Similarly, the ClayFF models have no three-coordinate O atoms, but $\sim$ 0.5% one-coordinate O atoms, while the Takada force field gives the largest number of both O atom coordination defects with more than 1% of both one- and three-coordinate O atoms. Experimentally, five-coordinate Si atoms in amorphous silica are rare except for silica under high pressures,[146] though they are a common defect in atomistic silica models. The BKS, CHIK, and ClayFF force fields agree well with this experimental observation in that they have little or no five-coordinate Si atoms. The Takada force field, in contrast, has the largest density of five-coordinate Si atoms. Similarly, the Takada force field generates a considerable number of O atoms with coordination

defects compared to the other models.

4.3.2 a-SiO_2 Slab Models

With this characterization of the properties of the bulk a-SiO_2 models obtained from the three force fields in hand, we now turn to an examination of the amorphous silica slab models. The functionalization method is described in Sec. 2.2.3.6 and we particularly point out that we have detailed our modifications of each force field to describe the silanols. For the remainder of this Chapter we consider only functionalized slab models with a silanol density of 2 OH/nm^2 generated by choosing strained Si–O bonds for hydroxylation.

4.3.2.1 Bond Distance and Angle Distributions

We begin by considering the local silica coordination structure represented by the Si–O bond and Si–O–Si and O–Si–O angle distributions. The O–Si–O and Si–O–Si angle distributions for the functionalized silica slabs are presented in Fig. 4.4 and the average values of all three quantities are given in Table 4.2. The distributions of Si–O bond distances for the four force fields are nearly identical to those for the bulk solid shown in Fig. 4.2a and is thus not shown here; comparison with the average Si–O bond values for the bulk solid in Table 4.1 shows minimal differences with these functionalized slab results.

Clear differences in the angle distributions for the functionalized slab results in Fig. 4.4 and the bulk results can be observed. One significant difference is the appearance of a peak at low angles, $80-100^\circ$, for both angle distributions; this angle region is not shown in the bulk silica results in Fig. 4.2b,c because those peaks are absent or minimal. As discussed in Chapter 3, these small angles are associated with the presence of two- and three-membered rings. The formation of these rings is important due to the fact that they are highly strained and are preferentially found on the surface of the a-SiO_2 slabs. Thus, they have implications for the potential reactivity of the slab structures if they are adapted for modeling that permits it, *e.g.*, reactive force field or electronic structure-based descriptions. It was noted in Sec. 3.3.3 that the BKS force field, at the 1 K/ps

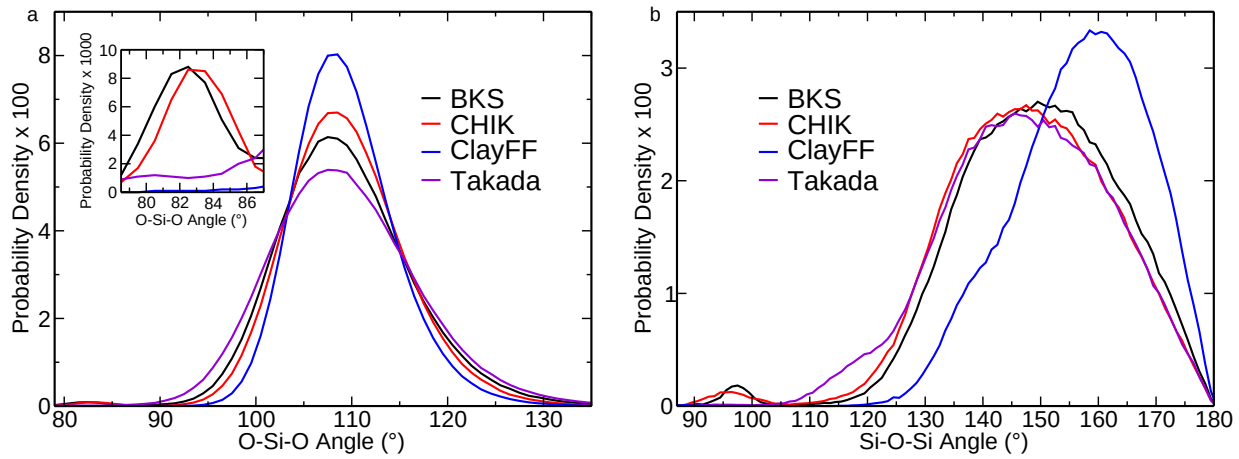

Figure 4.4: Distributions for the (a) O–Si–O angle and (b) Si–O–Si angle for functionalized a-SiO_2 slabs generated with different force fields. The inset in panel (a) highlights the small O–Si–O angle region that corresponds to strained, two- and three-membered rings.

Force Field	BKS	CHIK	ClayFF	Takada	Experimental
Si–O (Å)	1.6159_5	1.6313_3	1.568_1	1.6411_5	1.62
O–Si–O (°)	109.32_1	109.367_8	109.400_7	109.32_2	109.7, 109.4
Si–O–Si (°)	149.5_4	147.8_2	156.6_5	147.5_3	153,[a] 144,[b] 142[c]

[a]Ref. [128] [b]Ref. [129] [c]Ref. [130]

Table 4.2: Average bond Si–O bond distance, O–Si–O angle, and Si–O–Si angle for amorphous silica slabs functionalized at a hydroxyl density of 2 OH/nm^2 with different force fields and compared to experimental results in the literature. Subscripts indicate 95% confidence intervals in the trailing digit(s).

cooling rate used here, forms two-membered rings almost exclusively at the slab interface and three-membered rings preferentially at the surface. The CHIK force field also behaves in the same manner, which is clear from the presence of the small angle peaks in both the O–Si–O and Si–O–Si angle distributions (particularly note the inset in Fig. 4.4a).

Associated with the appearance of this peak at small angles, the average values for the Si–O–Si angle for the BKS and CHIK force fields are $\sim 2°$ smaller than that found for bulk a-SiO_2 in Table 4.1. In contrast, no peak at small angles is observed for the Takada force field or ClayFF, which can be clearly seen in the inset of Fig. 4.4a and in Fig. 4.4b. The Takada slab models show a slightly narrowed O–Si–O angle distribution compared to bulk silica, Fig. 4.2b, whereas the other force fields are otherwise unchanged from their bulk behavior.

4.3.2.2 Coordination Number

The coordination states of Si and O atoms in the slab models was characterized both before and after functionalization and the results are shown in Fig. 4.5. As with bulk *a*-SiO_2, a cutoff of 2.2 Å was used for the Si–O bond distance.

The trend for the Si coordination of unfunctionalized slabs, Fig. 4.5a, is similar to the bulk, Fig. 4.3, in that the bare slabs from the BKS and CHIK force fields are >99.5% four-coordinate Si atoms, with smaller fractions predicted by ClayFF and Takada. Notably, the percentage of four-coordinate Si atoms for ClayFF is significantly smaller (<94%) than the bulk percentage (>98.7%). This decrease in four-coordinate Si atoms is compensated exclusively by three-coordinate defects.

However, after functionalization (which also includes an equilibration stage after the addition of silanol groups) all force fields have more than 99.3% four-coordinate Si atoms, which can be seen in Fig. 4.5b. The occurrence of three-coordinate defects is also reduced significantly. The absence of five-coordinated Si for CHIK and ClayFF is present for both unfunctionalized and functionalized slab models, as it is in the bulk solid (Fig. 4.3), in agreement with experimental observations.[146]

The unfunctionalized slabs from the Takada force field, Fig. 4.5c, have the most O atom coordination defects in the form of one- and three-coordinate atoms. ClayFF also has a signfiicant percentage of one-coordinate O atoms, nearly 3.5%. However, this is significantly reduced in the functionalized slabs, in which the ClayFF models actually contain a smaller fraction of O atom coordination defects than those from the CHIK force field, Fig. 4.5d.

It is important to revisit the functionalization algorithm outlined in Sec. 2.2.2 to better understand the significant improvement in the coordination defect density, particularly in the case of ClayFF, when the slabs are functionalized. The first step in the algorithm is to functionalize one-coordinate O atoms and three-coordinate Si atoms as a pair to minimize the number of coordination defects on the slab surface. Comparing the pre- and post-functionalization results in Fig. 4.5 shows that this part of the algorithm heals a significant number of such defect sites in the ClayFF slabs.

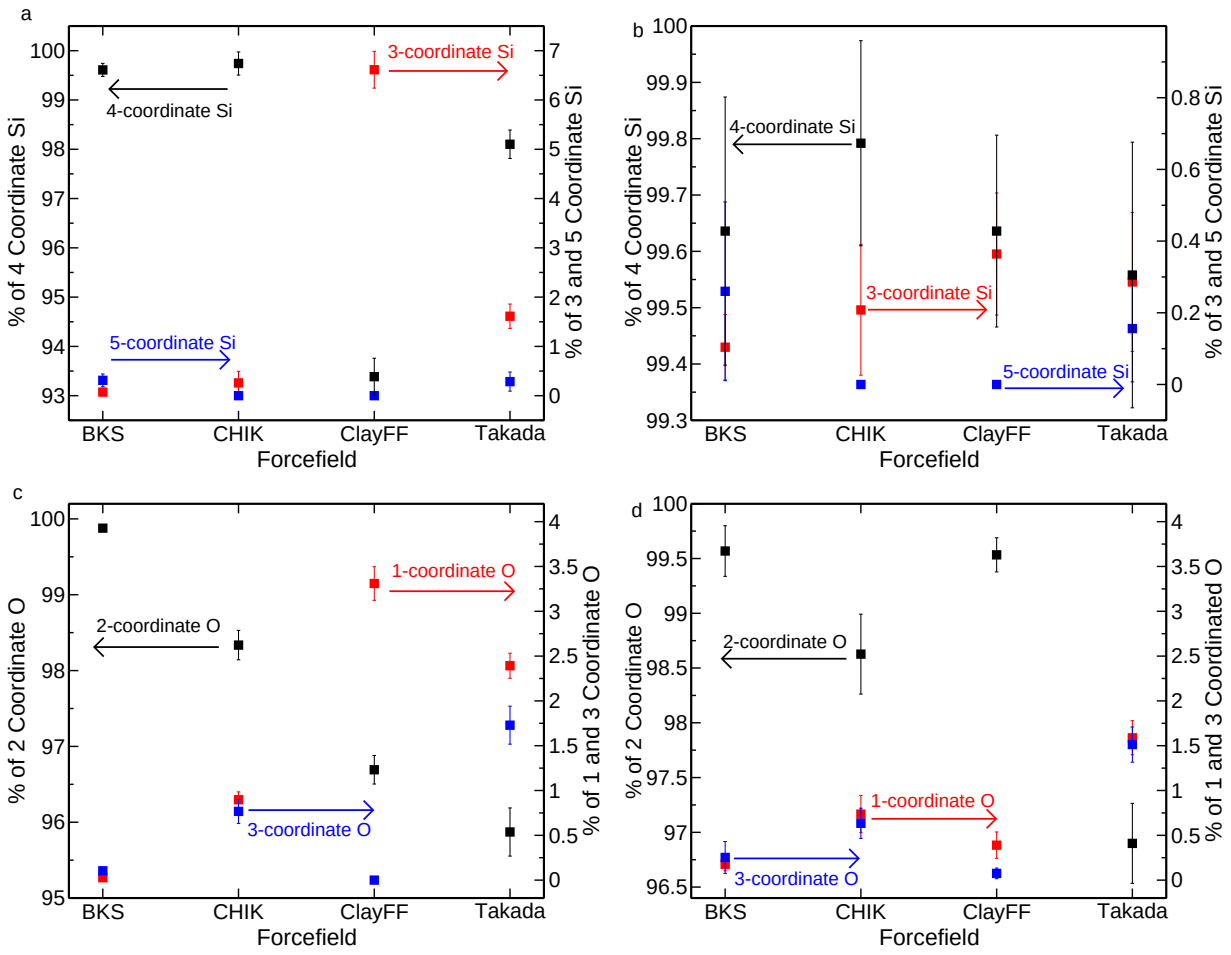

Figure 4.5: Percentage of each coordination state of Si atoms (a) before and (b) after functionalization and O atoms (c) before and (d) after functionalization in a-SiO_2 slabs generated with the different force fields. Results are averaged over 20 slabs for each case and the error bars shown the standard deviation within this set.

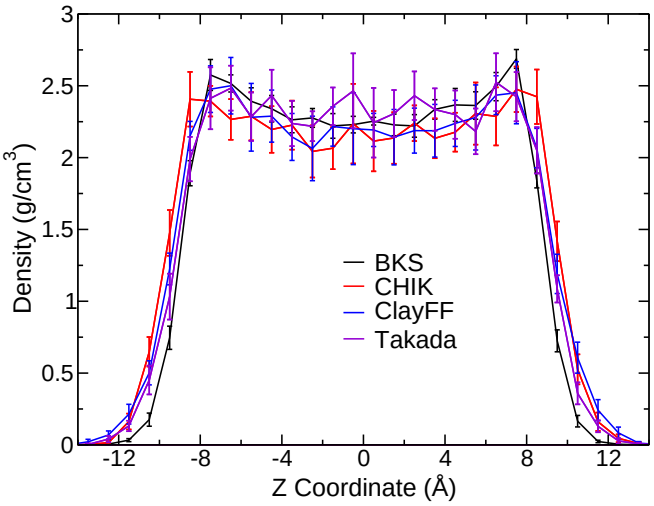

Figure 4.6: Total density of unfunctionalized a-SiO_2 slabs generated with the different force fields. These results are averaged over 20 slabs for each case and the error bars shown the standard deviation within the set.

This result suggests that the ClayFF coordination defects are localized at the surface and occur in the kind of Si and O atom defect pairs required by the functionalization algorithm.

4.3.2.3 Density

Now we consider the density of the slab models, determined using the same procedure described in Sec. 3.3.4. The results for the four force fields are shown in Fig. 4.6 using a bin width along the z axis of the slab of 1.0 Å. The average density in the interior of the slabs (small $|z|$ values) is approximately 2.25 g/cm^3 for the BKS, CHIK, and ClayFF slabs, but is slightly higher for the Takada models.

For all of the force fields the density is non-uniform across the slab, indicative of a similar densification (or lack of surface roughness) at the surface of the slabs, as is discussed in Sec. 3.3.4. Thus, this feature appears to be characteristic of the cooling rate and not specific to a particular force field. However, it does appear that the effect is most prominent in the BKS slabs compared to the other three force fields. An examination of the surface roughness of these slabs will be carried out and should provide additional insight into this feature of the density profiles.

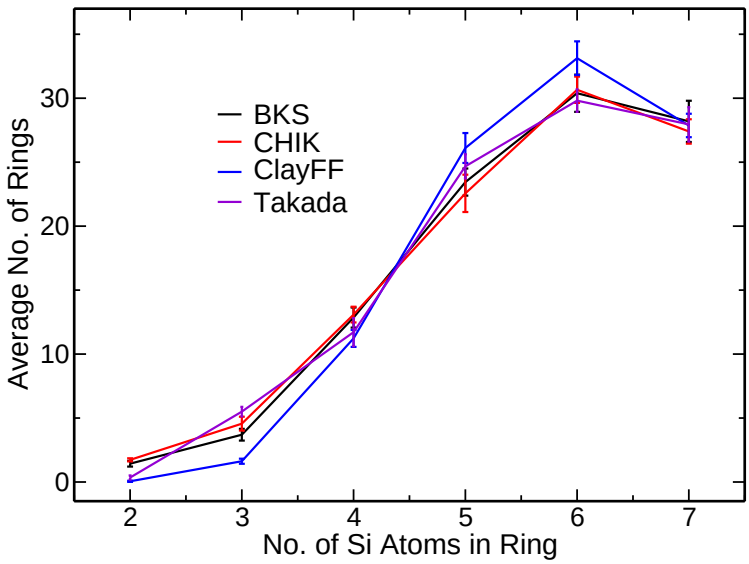

Figure 4.7: Ring distributions for unfunctionalized silica slabs of different force fields

4.3.2.4 Ring Distribution

Finally, we turn to an examination of the ring structures predicted by the four force fields in the *a*-SiO_2 slab structures. For simplicity, we consider only the unfunctionalized slab models. The rings are calculated using the procedure detailed in Sec. 3.3.3 and the results for the four force fields are shown in Fig. 4.7. In Chapter 3 we found that, for the BKS force field, the presence of strained, two- and three-membered, rings is diminished as the cooling rate decreases. Thus, because the slabs considered here are formed using the smallest, 1 K/ps, cooling rate we have considered, they represent the smallest fraction of these small rings for the BKS model.

The results in Fig. 4.7 show that the CHIK and Takada force fields give ring distributions that are in qualitative and quantitative accord with those for the BKS slabs. One slight difference is observed in the near absence of two-membered rings in the Takada slabs, which is accompanied by a slightly higher occurrence of three-membered rings. This is consistent with the angle distributions shown in Fig. 4.4 that show a small, but non-zero probability of finding the strained, $80-100^{\circ}$, O–Si–O angles that are associated with the smallest rings; both BKS and CHIK models exhibit a distinct peak at these small angles, consistent with the presence of two-membered rings.

ClayFF gives a distribution of ring sizes that is distinctly different than the other three force

fields. It is particularly characterized by an absence of two-membered rings and a distinctly smaller fraction of three-membered rings. This result was foreshadowed by the complete absence of amplitude in the small angle region of the O–Si–O angle distribution in Fig. 4.4. This relative absence of the small, strained rings gives the ClayFF slabs a ring distribution that is more strongly peaked around the more stable, five- and six-membered, rings.

4.3.2.5 Conclusions

We have generated twenty silica slab models for each of three force fields – CHIK, ClayFF, and Takada – and characterized their structural properties in detail, comparing to the analogous results for the BKS force field considered in even greater detail in Chapter 3. This analysis shows that varying the force field does indeed produce surfaces with different properties, *i.e.*, pair radial distribution functions, bond distance and angle distributions, coordination numbers, and ring distributions.

The bond and angle distributions are the only ones we have that are quantitatively determined by measurements. In these characteristics, the BKS, CHIK, and Takada force fields are in accord with one another and also agree well with the experimental benchmarks. In contrast, ClayFF does not reproduce the measured Si–O average bond distance and appears to overestimate the average O–Si–O angle. This suggests that ClayFF is not the best description of these local coordination geometry metrics for amorphous silica, while the other three force fields provide a satisfactory representation of the measured results.

The force fields show additional differences in the density of Si and O atom coordination defects as well as the distribution of ring structures. In the case of the former, CHIK and BKS exhibit the smallest number of coordination defects, while slabs created using ClayFF and Takada have higher defect densities. A functionalization algorithm that hydroxylates surface coordination defects reduces the number in functionalized slabs, particularly for the ClayFF models. In the ring distributions, the CHIK and BKS force fields are again very similar to one another. Takada is also in good agreement with these two force fields, except that it generates slabs with virtually no two-

membered rings but more three-membered rings. ClayFF, on the other hand, has no two-membered rings and few three-membered rings and instead favors larger, more stable ring structures. This is generally consistent with the features of the coordination geometry discussed above, *i.e.*, ClayFF appears to predict silica that is more structured than that produced by the other force fields. An examination of the tetrahedrality of the silica structure in the future would be insightful in further elucidating these differences.

Understanding the differences between a-SiO_2 models is important in developing simulation methods that are representative of experiments and can thus be used to make predictions about real silica materials. The challenges of characterizing these amorphous systems experimentally requires that simulations span a wide range of potential structural features, examine their effects on the interactions and function of the materials, and connect them with the properties of silica that are measurable. It is in this context that we hope the realistic silica slab models reported here can further advance our understanding of and ability to simulate amorphous silica materials.

Chapter 5

Water Reorientation in Amorphous Silica Slit Pores and the Relationship to Surface Roughness

5.1 Introduction

The structural and dynamical properties of confined water play an integral role in many fields including materials and biology.[147–150] Mesoporous silicates such as MCM-41, SBA-15, and controlled-pore glasses are being used in applications for catalysis[151, 152] and separations[21] as well as for models of water confined in rock and mineral materials in geology. The modified thermodynamics of confined water and selective adsorption of solute species, both of which are influenced by the interactions with the pore walls, are some of the key properties that affect the reaction kinetics and mechanisms in these systems.[153] Potential applications of porous silica nanoparticles in drug delivery[22, 23] require greater exploration of the silica-water interface to understand their behavior in biological environments. This interest in silica nanoparticles has grown primarily due to their ability to stabilize molecules, that are otherwise poorly soluble in water, within the confining framework of their mesopores.[154] In each of these applications, understanding the water structure and dynamics at and near the silica surface is crucial to rational design of the materials.

The OH reorientational dynamics in water can be measured directly in experiments using either ultrafast infrared pump-probe or nuclear magnetic resonance techniques as discussed in more detail in Sec. 5.3 below. Previous theoretical studies on water reorientation in hydrophilic silica pores (with cylindrical geometries) found a non-exponential reorientational dynamics.[42, 52, 110]

It is now well understood that OH reorientation in water can be understood in terms of large-angle “jump" associated with the exchange of the hydrogen-bond acceptor for the OH group and a minor “frame" component associated with reorientation of the hydrogen-bonded pair between such exchanges.[143, 144] In this sense, the reorientational dynamics parallels closely (and reports on) hydrogen-bond exchanges, which represent its fundamental underlying process. Both the reorientation and hydrogen-bond dynamics in roughly cylindrical amorphous silica pores have been previously investigated in our research group in collaboration with Prof. Damien Laage.[52, 110] They found that the observed non-exponential dynamics was associated with static heterogeneity associated with the widely varying local environments of individual hydrogen bonding sites on the pore surface. These mostly entropic effects can be understood in terms of two effects. The first is how the topology of the surrounding silica framework prevents water molecules that can serve as new hydrogen-bond acceptors from approaching the OH group. The second is how the silica surface constrains the arrangement of the hydrogen-bond network in its vicinity, which also modulates the ways in which a hydrogen-bond exchange can occur.[110] Both of these effects are determined by the heterogeneity of the pore surface and a key hypothesis that arises from this work is that a rougher surface will exhibit a different non-exponential decay than an atomically flat one. The former would present a wider array of environments that each modulate the hydrogen-bond exchange rate constant differently while the latter would have hydrogen-bonding sites that are all effectively equivalent. This is one of the motivations of the work presented in Chapters 2-4 in which we demonstrated we can generate realistic silica models of varying roughness.

The main focus of this Chapter is the relationship between the amorphous silica surface structure and the dynamics of the liquid water next to it. The investigation centers on a-SiO_2 slit pore models of about 3 nm in diameter and special attention is given to the surface roughness of the pore surface. We make use of the ability to control the atomic scale roughness of the silica slab surfaces, described in Chapter 3, through the cooling rate in the melt-quench-functionalize procedure. This advance enables the investigation described in this Chapter in which the water reorientational dynamics are explored for several surfaces with varying roughness; to our knowledge the connection

between surface roughness and water dynamics has not previously been studied, though, as noted above, previous work has suggested it could be important.[52, 110] It is hoped that the insight gained in this work will advance the design of a-SiO_2 materials for future applications.

5.2 Computational Methods

In this Chapter, we present the results of MD simulations of water confined within slit pores obtained from the amorphous silica slabs described in Chapter 3. The creation of the slit pores is described in detail in Sec. 2.3. A key feature of this approach is the cooling rate in the melt-quench-functionalize method for generating the slabs as described in Chapter 2, which we have shown in Chapter 3 can be used to tune the surface roughness. In the present studies, an ensemble of five surfaces each from the two extreme cooling rates, 1 K/ps and 1000 K/ps, using the BKS potential, were used. For both cooling rates, slabs with the smallest number of defects were selected. The smoother slabs (1 K/ps) involve only four-coordinate Si atoms. The rougher (1000 K/ps) slabs contain coordination defects, primarily five-coordinate Si, as we do not find any slabs generated at this cooling rate that are free of coordination defects. Each slab has a hydroxyl coverage of approximately 2 OH/nm^2; the precise densities are 2.26 OH/nm^2 for both 1 K/ps case, and 1000 K/ps slabs, where the difference from the nominal density arises from the presence or absence of the under-coordinated sites on the surfaces that are functionalized with OH groups.

The water-filled slit pores are generated as described in Sec. 2.3, where the details of the Gulmen-Thompson force field[6, 7] for silica are also provided. The SPC/E model,[107] which accurately describes the OH reorientation timescales of water[144] is used to represent the H_2O interactions.

Each water-filled slit pore model was propagated for five 20 ns production trajectories in the NVT ensemble following 1 ns NVE and 0.5 ns NVT equilibration stages with the trajectories differing in the initial velocities. These trajectories were used to calculate the reorientation dynamics. Error bars are given as 95% confidence intervals based on the Student's t-distribution using block averaging with each trajectory as a block.

5.3 Reorientation Dynamics

The OH reorientational dynamics of water are typically characterized by reorientational time correlation functions (TCFs) of the form

$$C_n(t) = \langle P_n[\vec{e}_{OH}(0) \cdot \vec{e}_{OH}(t)] \rangle, \tag{5.1}$$

where $P_n(x)$ is the n^{th} Legendre polynomial, $\vec{e}_{OH}(t)$ is the unit vector along the OH bond (pointing from O to H) at time t, and $\langle \cdots \rangle$ indicates a thermal average.

Different orders n of this TCF are relevant to various measurements. For example, the $C_1(t)$ time correlation function appears as part of the infrared (IR) absorption lineshape while the $C_2(t)$ TCF is a component of the Raman lineshape. Most importantly, the $C_2(t)$ time correlation function can be directly measured in IR pump-probe anisotropy measurements. In these experiments, OH modes are excited by a pump pulse from the ground, $n = 0$, vibrational state to the $n = 1$ excited state. At a time t later a probe pulse is sent through the sample and the intensity is measured (corresponding to absorption from $n = 1$ to $n = 2$). The experiment is carried out with two polarization combinations, the first where the pump and probe pulses are parallel giving signal $S_{\parallel}(t)$ and the second where the probe pulse is perpendicular to the pump pulse yielding signal $S_{\perp}(t)$. The anisotropy decay is then given as

$$r(t) = \frac{S_{\parallel}(t) - S_{\perp}(t)}{S_{\parallel}(t) + 2S_{\perp}(t)}. \tag{5.2}$$

It is possible to show that under modest assumptions,[155] which are typically valid for liquid water (see, *e.g.*, Ref. [111]), this anisotropy decay, $r(t)$, is directly proportional to the 2^{nd}-order reorientational TCF as

$$r(t) = \frac{2}{5} C_2(t), \tag{5.3}$$

which can be directly calculated from MD simulations as we do here.

In addition, information about the reorientational dynamics can be obtained from NMR spin-

echo measurements. In particular, they can be used to determine the integrated reorientational time[156]

$$\langle \tau_2 \rangle = \int_0^\infty C_2(t)\, dt. \tag{5.4}$$

Because of the connection to both IR pump-probe anisotropy and NMR measurements, $C_2(t)$ is generally regarded as the most relevant reorientational TCF and, for the same reason, it is the one we consider in this work.

In bulk water, $C_2(t)$ decays with three timescales that can be attributed to inertial or ballistic dynamics, librational motion, and reorientation associated with hydrogen-bond (H-bond) dynamics (in order of increasing length of the timescale). Thus, the TCF can be accurately fit by

$$C_2(t) = \sum_\alpha A_\alpha\, e^{-t/\tau_\alpha}, \tag{5.5}$$

where $\alpha = iner$, $libr$, and 2 and A_α is the amplitude of decay associated with the α timescale, τ_α. For bulk water (specifically HOD in D_2O or HOD in H_2O which avoid resonant vibrational coupling effects associated with H_2O) these timescales are $\tau_{iner} \simeq 15$ fs, $\tau_{libr} \simeq 450$ fs, and $\tau_2 \simeq 2.6$ ps.[157–162] As we will see, this description no longer holds when water is confined in silica pores. These bulk water timescales can still be observed, but additional slower dynamics appear.[52, 110]

It is also important to note that the OH reorientational dynamics are directly related to H-bond exchanges, or “jumps." Specifically, Laage and Hynes have shown[143, 144] that the OH reorientation time τ_2 can be quantitatively expressed in terms of contributions from H-bond jumps and from the “frame" reorientation of the intact H-bonded pair (the OH group and its H-bond acceptor) between jumps,

$$\frac{1}{\tau_2} = \frac{1}{\tau_{2,jump}} + \frac{1}{\tau_{2,frame}}. \tag{5.6}$$

In bulk water the jump contribution is the dominant one. In confined water, the same assumption cannot necessarily be made, but it is true for OH groups that are H-bonded to silica. In that case, clearly the silica and H-bonded water cannot reorient so that the frame reorientation is negligible

	Cooling Rate			
	1 K/ps		1000 K/ps	
Pore	RMSD (Å)	SASA (Å^2)	RMSD (Å)	SASA (Å^2)
1	1.47	193.8	1.75	197.7
2	1.29	152.7	1.95	276.2
3	1.30	158.6	1.64	243.5
4	1.27	145.9	1.30	189.1
5	1.43	174.9	1.80	218.6
Avg.	1.35	165.2	1.69	225.0

Table 5.1: Calculated surface roughness, by both the root mean-squared deviation (RMSD) from the mean plane and the free solvent-accessible surface area (SASA), for the 10 slit pores used in this work. Note that the roughness is averaged over both surfaces of each pore.

for such OH groups. At the same time, OH moieties H-bonded to silica oxygens can make jumps to other potential acceptors that are also part of the silica surface but such H-bond exchanges cannot lead to full reorientation. Thus, jumps from a silica oxygen acceptor to a water acceptor are a key component of OH reorientation for water molecules at the interface.[110]

5.4 Results and Discussion

5.4.1 Surface Roughness

We first discuss the surface roughness of the two sets of five slit pore models, obtained with different cooling rates, used in the simulations. The roughness of each slit pore has been characterized using the two methods described in Sec. 3.3.5, *i.e.*, the root mean-squared deviation (RMSD) from the mean plane and the free solvent-accessible surface area (SASA). The results for the individual pores are plotted in Fig. 5.1 and are listed in Table 5.1.

The results show that the pores formed from 1 K/ps-cooled slabs are lower than those from 1000 K/ps slabs with the exception of Pore 4 in the latter category. In Sec. 3.3.5 we showed that the average roughness for silica slabs obtained by quenching the liquid at 1 K/ps were significantly different than those produced using 1000 K/ps and that the standard deviations did not overlap. These results demonstrate that the distributions of surface roughness for the two cooling rates do

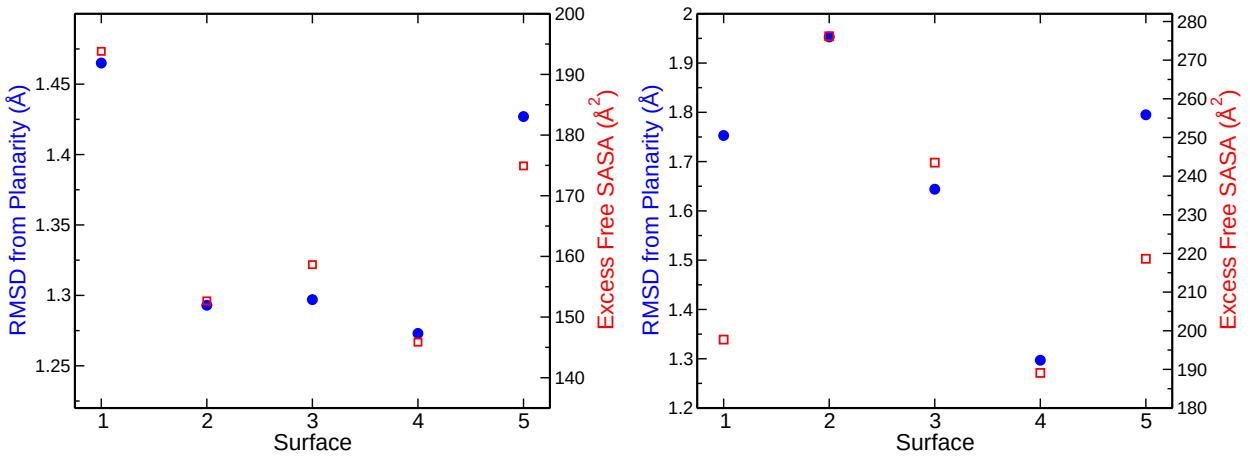

Figure 5.1: Surface roughness (averaged over both surfaces) of the 10 slit pores used in this work. Results are shown for pores constructed with slabs generated with cooling rates at 1 (left) and 1000 K/ps (right). Roughness results calculated with by the surface RMSD (filled blue circles) and SASA (open red squares) are shown.

still overlap, *i.e.*, at least the 1000 K/ps case has a roughness distribution that includes surfaces with large deviations from the mean. It is also interesting to note from Fig. 5.1 that for the majority of the slabs, including all the 1 K/ps ones, the RMSD and SASA measures of surface roughness are in excellent agreement. However, for the 1000 K/ps case Pores 1 and 5 exhibit significant differences, with the RMSD indicating significantly greater roughness than the SASA. This may be an indication of roughness that is too small for the probe particle in the SASA calculation to penetrate or curvature effects that influence the RMSD from the mean plane; both possibilities which would suggest the lower SASA values may be more relevant to understanding how water interacts with the surface. In the future, this will be investigated by additional SASA calculations as a function of probe particle radius as well as visual inspection of the slab surfaces.

5.4.2 Water Density Profiles

Before considering the OH reorientation dynamics, it is useful to first consider some of the basic elements of the water structure within the slit pores. The simplest of these is the water (mass) density as a function of z, the coordinate that lies in the nominally surface normal direction. The density profiles for the five slit pores used in the simulations for each cooling rate used to obtain

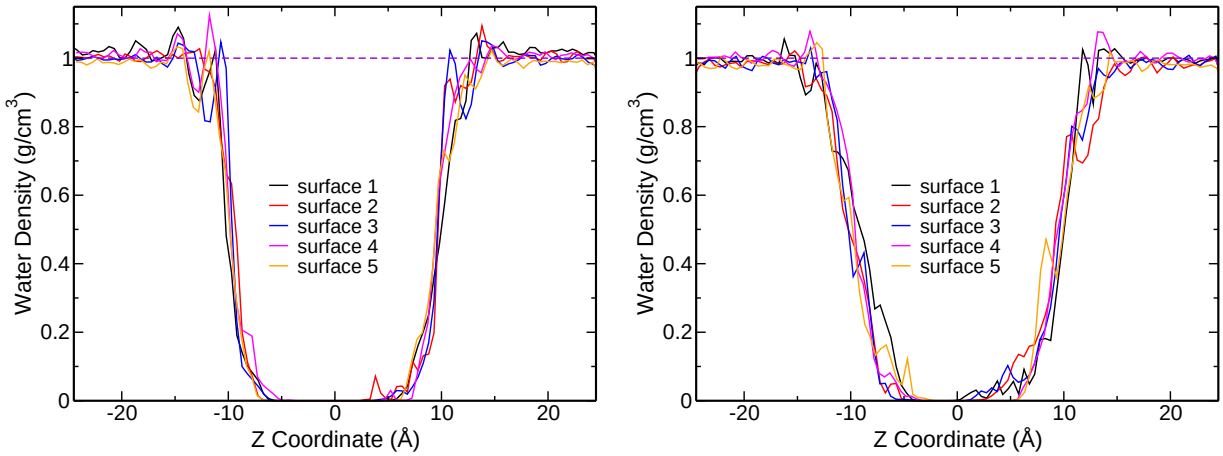

Figure 5.2: Water mass density as a function of the z coordinate that is perpendicular to the nominal surface normal. Results are shown for each of the $\sim$ 3 nm slit pores formed from silica slabs generated from cooling at 1 K/ps (left) and 1000 K/ps (right).

the silica slab are shown in Fig. 5.2. The results allow a comparison between the water density around the slabs generated using the slow 1 K/ps cooling rate and the rapid cooling, 1000 K/ps, that does not permit as much relaxation of the silica structure. To facilitate the comparison between slit pores, each silica slab was centered at $z = 0$.

First, we note that far from the silica interface the water density is ~ 1.0 g/cm^3, which is the same as that observed for bulk SPC/E water. This indicates that the confinement at this 3 nm length scale yields bulk-like water in the pore interior at least with respect to the liquid density.

Second, near the silica interface the density profiles for a given cooling rate vary somewhat between the different individual slit pores. This demonstrates that these pore surfaces are atomistically distinct. However, the general features of the rise in water density moving across the interface are consistent within each cooling rate. In particular, a distinctly sharper rise from zero density toward the bulk density is observed for the slit pores formed with slowly cooled (1 K/ps) slabs compared to the rapidly cooled (1000 K/ps) ones. This indicates a rougher silica-water interface for the latter.

The density profiles in Fig. 5.2 suggest that this difference in roughness has consequences for the water structure at the slit pore interfaces. In particular, a considerable amount of water molecules are able to sit in divots which occur on the rougher surfaces, but not as much in smoother

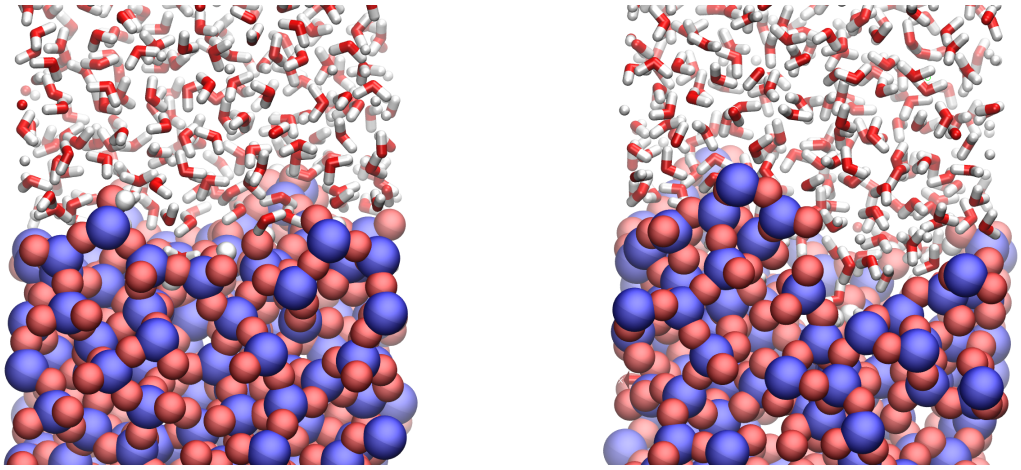

Figure 5.3: Simulation snapshots of the silica-water slit pore interface: Pore 2 from the 1 K/ps pores (left) and Pore 1 from the 1000 K/ps pores (right).

slab surfaces, where these divots are not present. To illustrate this notion, we have included two snapshots from the pores generated in Fig. 5.3, where we have chosen the pore surfaces that showed the most slowed reorientational dynamics (*vide infra*) from each set of pores. We stress that the water is not penetrating into the silica structure itself, but only the valleys accessible from the water pool of the slit pore.

Third, not only do these two slabs differ in roughness which is evident by visual examination of their structures and their density profiles, their surface curvatures are also quite different. The pore from the 1 K/ps rate shown in Fig. 5.3 has a much smoother surface while the pore from the 1000 K/ps rate shown in Fig. 5.3 exhibits significant curvature. In addition, in the rougher pore, there is a huge divot located in the center of the pore which is filled by water molecules that must experience a quite different environment than those at a flat silica interface. Pore curvature has long been one of the components that influence nano-confined liquid dynamics, and we are able to observe it in our simple slit pore models since our slab generation does not involve cleaving, which results in an artificially flat surface.

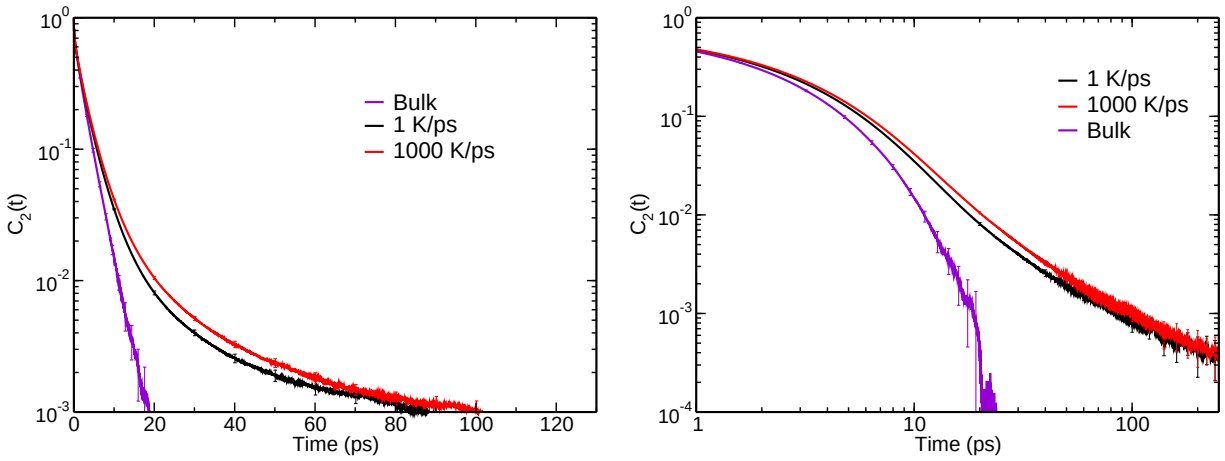

Figure 5.4: Reorientational TCF $C_2(t)$ averaged over all five 1 K/ps slit pores (black line) and over all five 1000 K/ps slit pores (red line). Bulk water results are shown for comparison (violet line). The results are shown on a semi-log (left) and log-log (right) scale to emphasize different regions of the decay.

5.4.3 Overall Reorientation Dynamics

5.4.3.1 Dynamics versus Cooling Rate

We now turn to an examination of how the OH reorientation dynamics depends on the cooling rate used to form the silica slabs making up the pores. To this end, the OH reorientational time correlation functions, $C_2(t)$, obtained from the MD simulations, are shown in Fig. 5.4 where the results are averaged over all five slit pores of each cooling rate. The bulk water result is also shown for comparison.

The bulk water $C_2(t)$ is well described by fitting to a tri-exponential decay as described in Sec. 5.3 with timescales of approximately 25 fs, 0.5 ps, and 2.6 ps, for the inertial, librational, and hydrogen-bond making and breaking components (τ_2), respectively.[163] This longest timescale can be understood as primarily associated with a 3.1 ps (for SPC/E water) "jump" time, *i.e.*, the inverse of the rate constant for the exchange of hydrogen-bond acceptors for the OH, and an ~ 6 ps timescale for the "frame" reorientation of the intact hydrogen-bond.

The same three approximate timescales also describe the shorter-time dynamics of the confined water $C_2(t)$ in pores with both cooling rates, though we find the librational and H-bond

making and breaking times are somewhat longer ($\sim$ 0.7 and 3.5 ps, respectively) in the pores. This indicates that bulk-like water is present in these 3 nm pores.

The significant effect of confinement on the reorientational dynamics is found in the long-time behavior of $C_2(t)$ indicating the silica surface, and perhaps the confinement effects associated with the presence of both silica surfaces, acts to retard the OH reorientation. Because this long-time reorientational dynamics is related to H-bond exchanges, it is natural to infer that it is determined by H-bonding of water molecules to the silica framework and more likely as H-bond donors than as acceptors. The slower dynamics of the confined water is significant. From Fig. 5.4 we can see that the bulk water $C_2(t)$ decays to 10^{-3} (from its starting value of 1) by 20 ps, while the same degree of decay takes $\sim$ 90 ps for the 1 K/ps pores and $\sim$ 100 ps for the 1000 K/ps pores. Moreover, from the log-log plot in Fig. 5.4 even the decay beyond these times is qualitatively different between the bulk and confined liquids; this behavior will be examined in greater detail below. It is these slower dynamics that are the primary focus of the remainder of this Chapter.

It is interesting to examine the effect of the cooling rate used to generate the pores given the relationship to surface roughness as detailed in Table 5.1. The $C_2(t)$ results in Fig. 5.4 show that the 1 K/ps pores exhibit OH reorientational dynamics that are distinguishably faster than that in the 1000 K/ps pores. These differences appear for times between 5 and 50 ps, while at longer times the two $C_2(t)$ are within error bars of each other. This suggests that, at least on average, the cooling rate used to generate the silica slabs affects the confined water reorientational dynamics of the pores. These differences are small, however, and the results in Fig. 5.4 do not clearly show whether they are due to the surface roughness or other features affected by the cooling rate.

5.4.3.2 Dynamics versus Surface Roughness

We can further investigate the role of surface roughness in the slowing of the OH reorientational dynamics of confined water by looking at the results for individual pores. We have shown above, Table 5.1 that the pores for both cooling rates exhibit a range of atomic-scale roughness. Here we examine whether that roughness is correlated with the water reorientational dynamics in the pores.

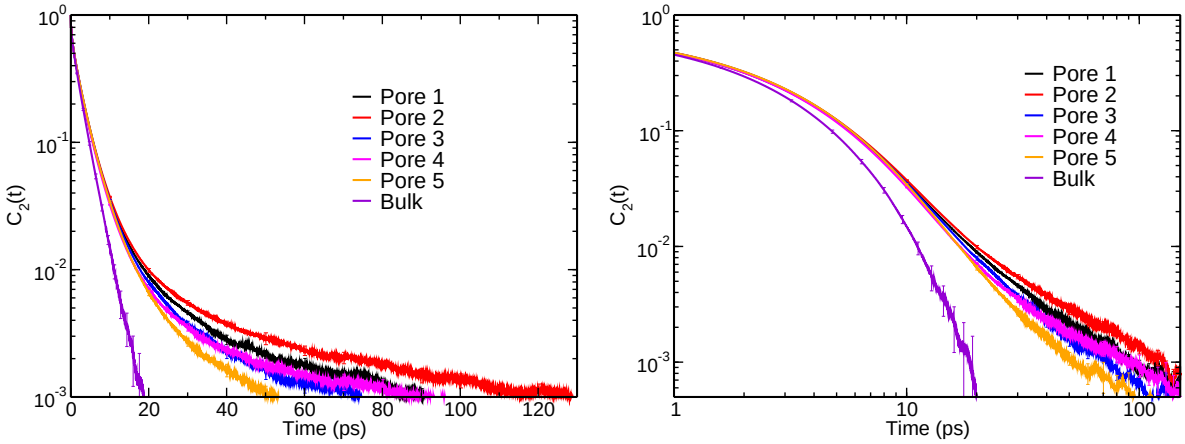

Figure 5.5: Total OH reorientational TCF, $C_2(t)$, for each of the 1 K/ps water-filled slit pores investigated. Results are shown on a semi-log (left) and log-log (right) scale to emphasize different regions of the decay. The $C_2(t)$ for bulk water is shown for comparison (violet line).

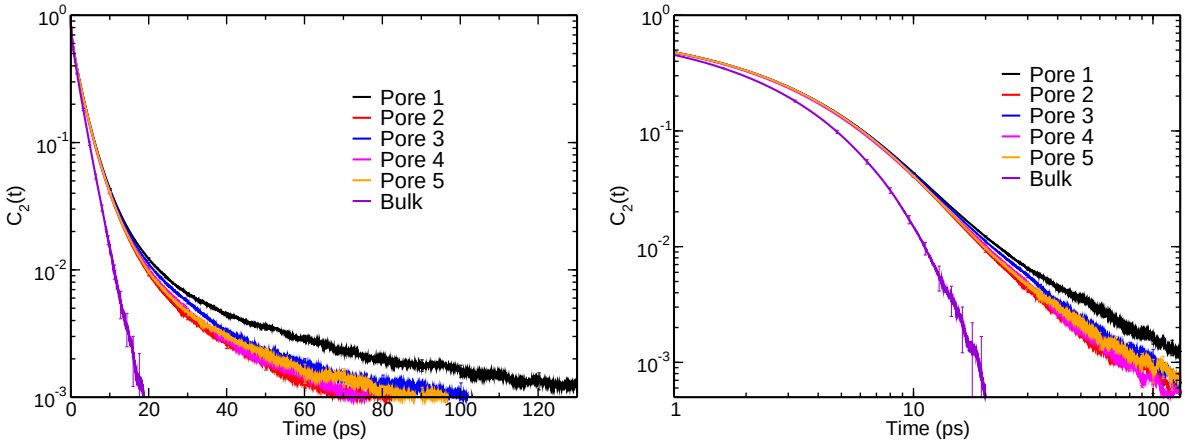

Figure 5.6: Same as Fig. 5.5 but for the five 1000 K/ps water-filled slit pores investigated.

The $C_2(t)$ for each of the five pores created from 1 K/ps cooled slabs are shown in Fig. 5.5 on both semi-log and log-log plots. Analogous results are shown for the 1000 K/ps pores in Fig. 5.6.

We can see from Figs. 5.5 and 5.6 that the $C_2(t)$ for the individual pores exhibit the same qualitative behavior as the results in Fig. 5.4 that are averaged over all five pores of each cooling rate. That is, they have a short-time decay (for times less than 5 or 10 ps) that is similar to bulk water, but dramatically slowed dynamics for longer times that extend well into the tens of ps.

Consider first the results for the 1 K/ps pores shown in Fig. 5.5. We see that there are variations between the $C_2(t)$ obtained with the different pores with Pore 2 exhibiting the slowest dynamics

and Pore 5 showing the fastest. The other three pores have dynamics that are relatively similar with the decay of $C_2(t)$ slightly slower for Pore 1 and the Pore 3 $C_2(t)$ decaying more slowly than that of Pore 4 at early times (< 40 ps) but more quickly at longer times.

We can examine this behavior in the context of the surface roughnesses determined by the RMSD and SASA calculations presented in Table 5.1. Those results found that Pores 1 and 5 were the roughest by both measures; they have nearly equivalent RMSD (1.47 and 1.43 Å) but Pore 1 has a larger SASA (194 vs 175 $Å^2$). On the other hand, Pores 2-4 have quite similar, and smaller, roughnesses by both measures; within the series, if the differences in calculated roughness is significant, Pore 4 is the smoothest and Pore 3 the roughest of this subset. Clearly, in the context of these characterizations of the surface roughness of the pores, the results in Fig. 5.5 do not show any correlation of the long-time OH reorientational dynamics with the pore roughness. If the two were correlated we would expect Pores 1 and 5 to have the slowest dynamics, but $C_2(t)$ for the water in Pore 5 exhibits the fastest decay and Pore 1 is only the second slowest. Instead, the slowest reorientational dynamics is observed in Pore 2, which is relatively smooth and effectively the same roughness of Pores 3 and 4, which do have faster dynamics.

We can carry out the same comparison for the 1000 K/ps pores. The results in Table 5.1 indicate that Pore 2 in that group is the roughest followed by Pores 1, 3, and 5 (which are ranked differently depending on whether one uses RMSD or SASA). Pore 4 has silica surfaces that are the smoothest. We do find that $C_2(t)$ for water in Pore 4 decays effectively as fast as any of the other pores. However, the dynamics in that, smoothest pore, are effectively the same as those in Pore 2, the roughest pore. The slowest dynamics is found for water in Pore 1, which is characterized as intermediate in roughness along with Pores 3 and 5 which have reorientation only slightly slower than that of Pores 2 and 4.

These results indicate that the data in Fig. 5.4, which shows that the 1000 K/ps pores exhibit water reorientational dynamics that is slower than that in the 1 K/ps pores, cannot be interpreted in terms of the surface roughness. An examination of the dynamics on a pore-by-pore basis shows no correlation between the decay the reorientational TCF and the surface roughness. In other words,

surface roughness, at least as we have characterized it in Sec. 5.4.1 is not fully determinative of the reorientational dynamics. This indicates that the dynamics have more complex origins. In previous work on roughly cylindrical pores we found that subtle entropic effects were partly responsible for slowdowns in the H-bond jump dynamics.[110] We traced these to the constraints of the silica interface placed upon the arrangement of the H-bond network, which limited the number of ways interfacial water molecules could undergo an exchange of H-bond acceptors. While these factors are related to the surface roughness, the current results suggest they may be identifiable only by more sophisticated definitions of "roughness" or by a more wholistic picture of the additional factors that are modified by cooling rate, *e.g.*, distribution of silanol sites, size and number of surface undulations, local curvature.

5.4.4 Distance-dependent Water Reorientation

Molecular dynamics simulations allow detailed insight into the influence of the silica surface on the water dynamics. One key measure is the spatial extent of the perturbation of the water which we can measure by examining the distance dependence of the OH reorientational dynamics. We measure this as the distance, d, of an H atom (in the OH of interest) from the nearest pore oxygen atom. Note that the division based on position is carried out only for $t = 0$ in the calculation of $C_2(t)$, *i.e.*, based on the initial position only, and the long timescales observed in the reorientational dynamics of the interfacial waters means that some waters can exchange positions as the TCF is calculated.

The reorientational dynamics of OH groups that are at $d = 2$ Å from the surface in the 1 K/ps and 1000 K/ps pores are shown in Fig. 5.7. The slow dynamics of these interfacial water molecules is immediately apparent, with $C_2(t)$ continuing to decay out to hundreds of ps. Note that this distance, within the histogramming approach, corresponds to OH groups with the hydrogen atom $1.5 - 2.5$ Å from a silica oxygen atom (either bridging or silanol as is discussed below). Thus, these are OH groups that are donating an H-bond to the silica surface. These would be expected to be significantly affected by the silica and they are. There are not any notable qualitative differences

between the results for the two different cooling rates, though we find the average result over all pores for $d = 2$ Å (not shown) exhibits the same behavior as the total $C_2(t)$ shown in Fig. 5.4, *i.e.*, the 1000 K/ps pores show slightly slower dynamics.

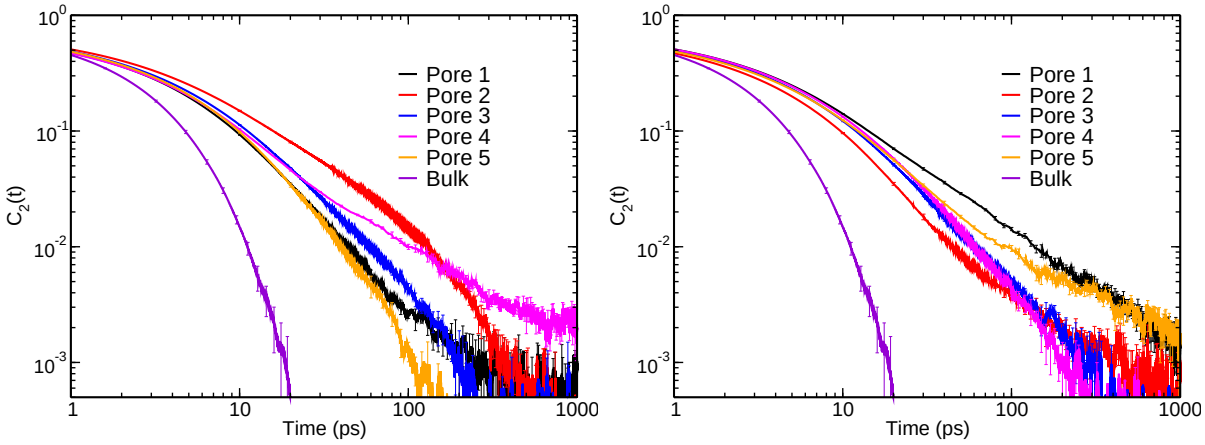

Figure 5.7: Reorientational TCF, $C_2(t)$, for OH groups that are a distance $d = 2$ Å from a silica oxygen atom at $t = 0$. Results are shown for the five pores formed from slabs using 1 (left) and 1000 K/ps (right) cooling rates. The $C_2(t)$ for bulk water is shown for comparison (violet line).

As in the previous section, we can examine the trends in the reorientational dynamics of these interfacial waters with the pore surface roughness. When all water molecules in the pore are considered, Figs. 5.5 and 5.6, we found that Pore 2 gives the slowest dynamics of all the 1 K/ps pores while for the 1000 K/ps pores it is Pore 1. This is also largely the same when only the OH groups closest to the interface are considered in Fig. 5.7. However, we do see that the 1 K/ps Pore 4 has an even slower long-time decay for times longer than ~ 150 ps. Similarly, the 1000 K/ps Pore 5 decays similarly to Pore 1 at very long times. These differences indicate the complexity of the non-exponential behavior of the $C_2(t)$ for these confined water systems. Despite some shuffling of this type, the general behavior found when averaging over all of the water molecules in the pore is preserved for the interfacial OH groups and, more accurately, likely arises from their behavior. Thus, the results in Fig. 5.7 further suggest at best a greater complexity in the relationship between surface roughness and interfacial reorientational dynamics and perhaps even no clear causative connection between the two.

The distance-dependent reorientational dynamics for two pores are shown in Fig. 5.8. Results

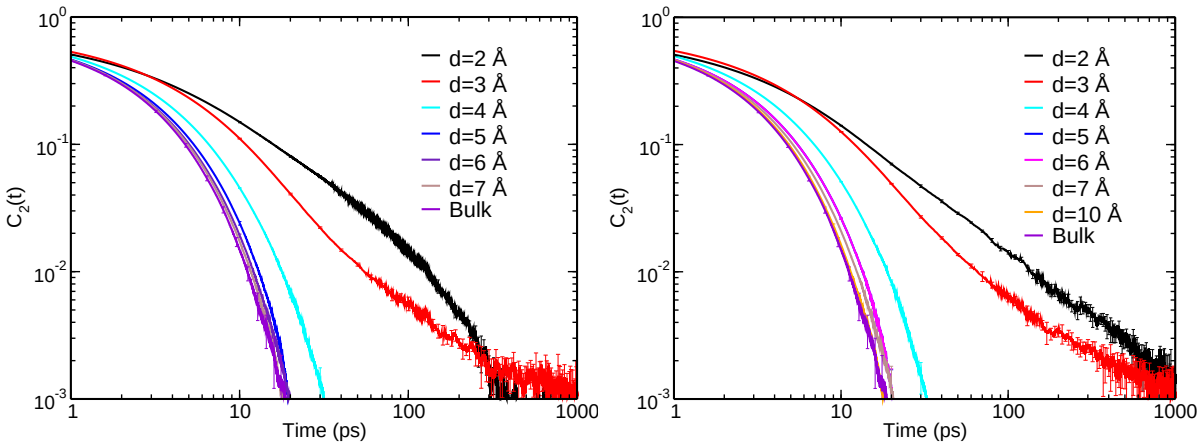

Figure 5.8: Reorientational TCF, $C_2(t)$, for OH groups as a function of the initial d from a silica oxygen atom at $t = 0$. Results are shown for the the 1 K/ps Pore 2 and the 1000 K/ps Pore 1, the pore for each cooling rate that yields the slowest reorientational dynamics. The $C_2(t)$ for bulk water is shown for comparison (violet line).

are presented for the pore with the slowest dynamics for each cooling rate, Pore 2 and Pore 1 for the 1 and 1000 K/ps ensembles, respectively. The two pores have $C_2(t)$ that are in general agreement with one another. The $d = 2$ and 3 Å reorientational TCFs are dramatically slowed and decay out to hundreds of ps or even 1 ns. There is then a qualitative transition in the behavior for larger d, where the $C_2(t)$ more closely resemble the bulk water result but with elongated timescales. This distance ($d = 4$ Å) is consistent with the layered water structure next to silica interfaces; the Lennard-Jones diameter of SPC/E water is $\sigma_O = 3.166$ Å so that the first water layer extends approximately this distance from the interface. Thus, the reorientational dynamics show dramatic, qualitative slowing only for this first water layer and molecules in the second layer and beyond are slowed but their dynamics is not qualitatively different than that of bulk water. The results for $d = 7$ Å is quite close to the bulk water result, indicating that bulk-like behavior is found at distances of less than 1 nm from the silica pore surface. This is a reasonably short lengthscale for the effects of the silica on the water dynamics, but is consistent with previous observations in cylindrical silica pores for both the reorientational dynamics[52, 110] and the spectral diffusion.[111]

It is interesting to note that for the 1 K/ps Pore 2 case the 2 Å reorientational TCF is larger than that for 3 Å for times less than $\sim$ 300 ps, but smaller for later times. A similar behavior

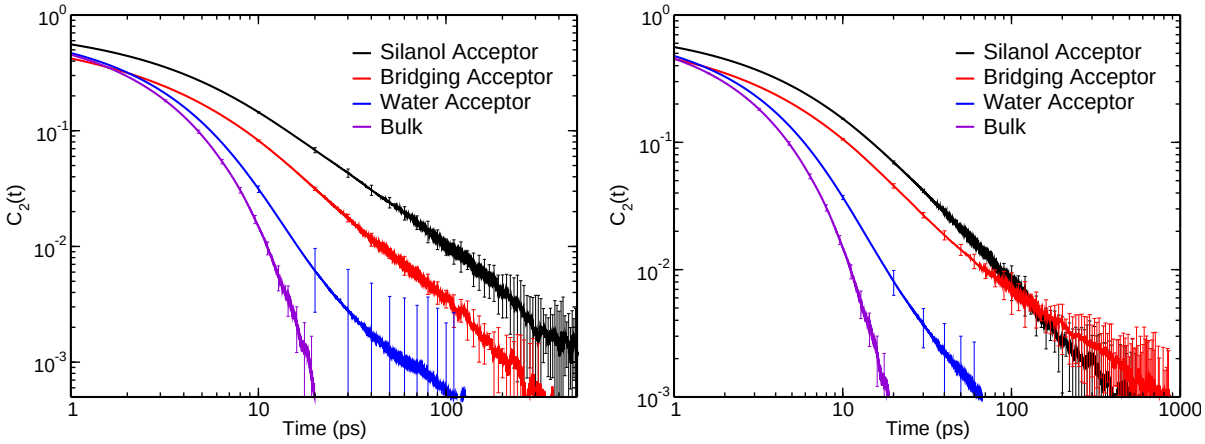

Figure 5.9: Reorientation decomposition into populations of different hydrogen bonding partners in pores: top: 1K/ps pores, bottom: 1000 K/ps pores

is observed for the 1000 K/ps pore, but the $C_2(t)$ for the two distances only cross toward the end of the correlation time, near 900 ps. This is, however, a counter-intuitive result. One would expect the closest waters to display the slowest dynamics, but that is not what is observed here. We hypothesize that this behavior is associated with exchange of OH groups within these two categories during the correlation time, but additional analysis is required to confirm this.

5.4.5 Reorientation Dependence on Hydrogen-bond Partner

Another method of decomposing the silica-water behavior is through the dependence of the water reorientation as a function of the type of hydrogen-bond partner. Specifically, we consider three classes of H-bonds in which an OH group can engage in the confined environment of the silica pores: *i)* a silanol, Si–OH, oxygen atom, *ii)* a bridging, Si–O–Si, oxygen atom, and *iii)* a water oxygen atom. (Note that we do not differentiate between silanols and geminals.) The reorientation for each category was carried out for every pore, and the resulting TCFs averaged over all the pores of each cooling rate are shown in Fig. 5.9.

The behavior is similar for the two cooling rates. Namely, the OH groups donating an H-bond to a silanol oxygen exhibit the slowest reorientation, followed by those H-bonded to a bridging oxygen. The OH moieties that donate an H-bond to a water oxygen have the fastest dynamics,

which is expected given that they include in the average molecules both close to and far from the interface. In the case of the 1000 K/ps pores the reorientational dynamics of OH groups H-bonded to bridging oxygens display a longer decay time so that their $C_2(t)$ is larger than that for those H-bonded to silanols for $t > 130$ ps. In contrast, the $C_2(t)$ for these two categories in the 1 K/ps pores appear to exhibit the same timescale for the long-time decay.

It is not obvious that the silanol acceptors should lead to slower dynamics. On one hand, they have larger partial charges than bridging oxygens (-0.74 versus -0.64; see Sec. 2.3). On the other hand, by definition they tend to extend out from the silica surface and are more accessible to water molecules, which would tend to make the approach of a new water H-bond acceptor easier than for buried bridging oxygens thereby accelerating OH reorientation. The results suggest that the larger charge is the more important effect. Because this electrostatic interaction effect is enthalpic in origin and the accessibility to new water H-bond acceptors is entropic, the balance between these two effects should be strongly temperature dependent. This suggests an interesting avenue for future studies.

5.5 Conclusion

In this study, we have utilized our previously generated *a*-SiO_2 models to generate slit-pores and used them to investigate the behavior of water in nanoconfinement. A key aspect of the study was the comparison of two sets of slit pores that have different surface roughness as measured by the root mean-squared deviation from planarity and the solvent-accessible surface area. This was accomplished in the development of models using different cooling rates to quench the molten silica into the amorphous solid. We showed in Chapter 3 that more rapid cooling leads to rougher surfaces and this is true of our pore models constructed with 1 and 1000 K/ps cooling rate slabs.

The total OH reorientational TCF, $C_2(t)$, was calculated for five slit pore models constructed of silica slabs generated from each cooling rate. We find the reorientation dynamics averaged over all the pores of each cooling rate do show differences. Namely, the rougher silica interfaces lead to slower OH reorientational dynamics than the smoother surfaces. The differences are quantitatively

small and appear primarily in the amplitude of the long-time decay. This suggests that they would probably not be observable in, *e.g.*, pump-probe IR anisotropy measurements, which can only be taken out to several picoseconds due to the comparatively short lifetime of the OH $n = 1$ vibrational state. Similarly, it is not clear if NMR measurements are sufficiently sensitive to distinguish between the two. On the other hand, there is ample evidence that mesoporous silica synthesized by different procedures could have much larger differences in surface roughness than that generated in these models.[150] In addition, surface-sensitive spectroscopies such as vibrational sum-frequency generation may readily observe the differences that originate in the interfacial water layer.

However, the differences we observe in the averaged $C_2(t)$ for each cooling rate cannot be attributed to the surface roughness. Examination of the $C_2(t)$ for each individual pore shows no correlation between the reorientational dynamics and the surface roughness. The same is observed when only the interfacial water OH groups, those close enough to donate an H-bond to the silica surface, are considered. It is these waters that exhibit the most significant slowdown of the water dynamics. Indeed, the influence of the surface is greatest in the first layer of water molecules next to the silica and water molecules that are $\sim 7-10$Å from the interface are nearly bulk-like in their reorientational dynamics. This suggests a relatively short-ranged effect of the silica surface on the water reorientational dynamics.

In summary, the present results do not support the hypothesis that greater surface roughness leads to slower water reorientational dynamics. The observed cooling rate effect, while small, must be associated with other surface features such as the distribution of silanols or perhaps even more specific topological features of the surface (*e.g.*, if our measures of surface roughness are too blunt to be meaningful for dynamics). This indicates a more nuanced relationship between the silica surface properties and the water dynamics.

Chapter 6

Summary and Future Directions

6.1 Summary

6.1.1 Amorphous Silica Slab Models with Tunable Properties

In this work we have proposed a general melt-quench-functionalize method for generating amorphous silica (a-SiO_2) slab models. We have successfully demonstrated that this approach can be used to develop models based on different force fields and with multiple tunable properties. Specifically, an *ad hoc* functionalization approach allows the total surface density of silanols to be controlled. Moreover, we showed that the spatial distribution of silanols on the surface can be modified by the criteria used to selected Si–O bonds that are hydroxylated. This procedure is general and can be extended well beyond the two cases considered here (strained Si–O bond selection and random Si–O bond selection), as is discussed below. However, the silanol distribution is a property that has been widely overlooked and represents an open question about silica surfaces, *i.e.*, it is still unknown if amorphous silica has a uniform or clustered distribution of silanols or whether this depends on the method of synthesis. Finally, the cooling rate of the quenching step was used to modulate the defect composition, ring formation, and surface roughness of the slabs. The surface roughness is a key feature that has been given little attention, but may have important consequences in the activity of catalyst active sites that are grafted on or doped in mesoporous silica supports. The present work demonstrates, for the first time, that the surface roughness can be systematically tuned within slab models. An important caveat, however, is that not all of these slab characteristics can be tuned individually, *e.g.*, coordination defects, ring structures, and surface

roughness are all correlated with the cooling rate.

6.1.2 Dynamics of Water Confined in Amorphous Silica Slit Pores

The effect of a key slab property, surface roughness, on the dynamics of water confined in amorphous silica slabs was investigated for the first time. The aim was to understand how the properties of the silica surface are manifested in spectroscopic measurements. In this case we focused on OH reorientation in water, which is directly probed by infrared pump-probe anisotropy or spin-echo nuclear magnetic resonance experiments. The hypothesis at the origin of the work was that the surface roughness of the slit pore surfaces will be correlated with the dynamics of the nano-confined water. Pore models created from amorphous silica slabs generated with different cooling rates in the quench step did exhibit distinctly different surface roughness. Moreover, the total reorientation dynamics, averaged over multiple pores for each cooling rate, show an effect of the cooling rate on the OH reorientational dynamics. However, examination of the dynamics for the individual pore models showed no correlation between the surface roughness of the pore surfaces and the reorientational dynamics. This suggests a more complex relationship between the water dynamics and silica surface structure. This may be a consequence of the relatively blunt measures of roughness used to characterize the surfaces, influence of the distribution of silanols, or more subtle effects of the cooling rate on the surface structure. Regardless, it points to interesting avenues for more detailed analysis and future investigations of this structure-dynamics relationship.

6.2 Future Directions

6.2.1 Improvements to the *a*-SiO_2 Slab Generation Procedure

A key aspect of the present approach that is ripe for improvement is the *ad hoc* functionalization procedure. The central feature in this respect is the method of choosing Si–O bonds for functionalization. It will be helpful and interesting to use electronic structure modeling, *e.g.*, within cluster models, to compare the energetics of functionalizing different Si–O bonds, which can lead to im-

proved algorithms for functionalizing the silica slab models. Similar approaches involving ReaxFF directly within the current slab models will also be of interest.

One clear direction for exploration is the relationship of the ring structures at the surface to the propensity for hydroxylation. Two-membered rings are strained structures that primarily occur on the surface of the slab. Chemical intuition suggests that these highly strained two-membered rings will be functionalized upon exposure to water, resulting in vicinal silanols. It is straightforward to modify our algorithm to select strained rings for functionalization, instead of strained Si–O bonds, and compare the distribution and stability of the resulting silanols.

6.2.2 An Opportunity: *a*-SiO_2 Nano-particles for Drug Delivery

One of the novel applications that has received growing interest is the use of *a*-SiO_2 nano particles in biology. A few of the attractive properties of these materials for drug delivery are mentioned in Sec. 1.2. A recent review by Croissant *et al.* discusses the ability to optimize properties such as the particle size, shape, pore sizes, and pore surface chemistry which have made these materials attractive for biomedical applications. However, there are conflicting reports of the observed toxicity.[164] Siloxane frameworks containing small, strained rings (see Chapter 3 and 4) have been suggested as one contributor to this toxicity.[165] Specifically, bond strain in the two- and three-membered ring structures promote hydrolysis as well as homolytic cleavage, which can produce destructive hydroxyl radicals. These population of these strained rings vary with the synthetic methods and the number of surface silanols determines the surface hydrophilicity/hydrophobicity. Further, Croissant *et al.* suggests that even the pattern of hydroxyls on the surface will determine the interactions between silica nanoparticles and cells[164].

This represents an interesting problem where the *a*-SiO_2 slabs generated in this study can be used. For example, our studies show that if a slow cooling rate is used, the amount of two- and three-membered rings that occur are minimal. Therefore, we can choose surface models that have a variable number of strained rings and use them to model silica-cell interactions. The effect on silica-cell interactions of the silanol coverage can also be examined using the models produced

in this work. Such simulations involving large biomolecules, however, can be computationally challenging because of the length- and time-scales involved, making the classical force fields considered in this work well-suited to the problem. Further, exploring the free energy landscapes of biological systems needs advanced sampling techniques that allow an accurate determination of the relevant free energy surface.

Also of importance is the effect of the surface properties in interactions with electrolyte solutions present in the biological media. This will require further development of silica models that can describe deprotonated silanol sites (Si–O^-) with accurate descriptions of the electrostatic interactions between silica an both water and ions. However, it is evident from the literature that the interest in a-SiO_2 nano-particles in biomedical applications is growing exponentially. This represents just one of the areas, beyond the catalysis applications that motivated it, in which the work of this thesis will be beneficial by permitting detailed, systematic examinations of the interactions that govern the behavior of amorphous silica materials in different environments.

6.2.3 Investigating the Amorphous Silica-Water Interface

The results presented in Chapter 5 showed that water molecules at the silica interface exhibit significantly slowed dynamics due to their interactions with the surface. One interesting observation was that, for some of the pore models, the water molecules closest to the surface displayed faster dynamics at longer times than molecules that were initially further away. This counter-intuitive result also contrasts with previous studies of water in cylindrical pore models that found a monotonic acceleration of the dynamics with distance from the silica surface.[52, 110] Hence, further investigation into the interfacial water dynamics in these slit-pore models are need to reconcile these results and better understand the surface features that are determining the water dynamics.

In addition, there are other interesting directions for future studies of these water-silica interfaces. The effects on the water dynamics found in Chapter 5 are relatively short range; bulk-like behavior is observed at distances of ~ 1 nm from the silica surface. This suggests that the dynamics are associated with interfacial, rather than confinement, effects. In order to examine this

it would be interesting to simulate the water-silica interface in a non-confining geometry using a simulation cell that involves a vapor phase above the water, *i.e.* a silica-water-vapor system. In addition, future analyses should focus on dissecting the contributions to changes in the dynamics due to surface characteristics such as surface roughness, silanol density, silanol distribution, and even defect composition of the surface. The first three properties can be systematically, and independently, tuned within the melt-quench-functionalize approach presented in this work. Such studies will advance our understanding of the behavior of water at an a-SiO_2 surface, including at catalytic active sites relevant to silica-supported heterogeneous catalysts.

References

[1] van Beest, B. W. H.; Kramer, G. J.; van Santen, R. A. "Force fields for silicas and aluminophosphates based on *ab initio* calculations", *Phys. Rev. Lett.* **1990,** *64,* 1955–1958.

[2] Carré, A.; Horbach, J.; Ispas, S.; Kob, W. "New fitting scheme to obtain effective potential from Car-Parrinello molecular dynamics simulations: Application to silica", *Europhys. Lett.* **2008,** *82,* 17001.

[3] Cygan, R. T.; Liang, J.-J.; Kalinichev, A. G. "Molecular models of hydroxide, oxyhydroxide, and clay phases and the development of a general force field", *J. Phys. Chem. B* **2004,** *108,* 1255–1266.

[4] Takada, A.; Richet, P.; Catlow, C. R. A.; Price, G. D. "Molecular dynamics simulations of vitreous silica structures", *J. Non-Cryst. Solids* **2004,** *345–346,* 224–229.

[5] Pedone, A.; Malavasi, G.; Menziani, M. C.; Cormack, A. N.; Segre, U. "A new self-consistent empirical interatomic potential model for oxides, silicates, and silica-based glasses", *J. Phys. Chem. B* **2006,** *110,* 11780–11795.

[6] Gulmen, T. S.; Thompson, W. H. "Model silica pores with controllable surface chemistry for molecular dynamics simulations", *Dynamics in Small Confining Systems VIII, edited by JT Fourkas, P. Levitz, R. Overney, M. Urbakh (Mater. Res. Soc. Symp. Proc. 899E, Warrendale, PA, 2005)* .

[7] Gulmen, T. S.; Thompson, W. H. "Testing a two-state model of nanoconfined liquids: conformational equilibrium of ethylene glycol in amorphous silica pores", *Langmuir* **2006,** *22,* 10919–10923.

[8] Ramanathan, A.; Subramaniam, B.; Badloe, D.; Hanefeld, U.; Maheswari, R. "Direct incorporation of tungsten into ultra-large-pore three-dimensional mesoporous silicate framework: W-KIT-6", *J. Porous Mater.* **2012,** *19*, 961–968.

[9] Yan, W.; Ramanathan, A.; Patel, P. D.; Maiti, S. K.; Laird, B. B.; Thompson, W. H.; Subramaniam, B. "Mechanistic insights for enhancing activity and stability of Nb-incorporated silicates for selective ethylene epoxidation ", *J. Catal.* **2016,** *336,* 75–84.

[10] Maiti, S. K.; Ramanathan, A.; Thompson, W. H.; Subramaniam, B. "Strategies to passivate Brønsted Acidity in Nb-TUD-1 enhance hydrogen peroxide utilization and reduce metal leaching during ethylene epoxidation", *Ind. Eng. Chem. Res.* **2017,** *56,* 1999–2007.

[11] Ewing, C. S.; Bagusetty, A.; Patriarca, E. G.; Lambrecht, D. S.; Veser, G.; Johnson, J. K. "Impact of support interactions for single-atom molybdenum catalysts on amorphous silica", *Ind. Eng. Chem. Res.* **2016,** *55,* 12350–12357.

[12] Xu, C.; Chen, G.; Zhao, Y.; Liu, P.; Duan, X.; Gu, L.; Fu, G.; Yuan, Y.; N, Z. "Interfacing with silica boosts the catalysis of copper", *Nat. Commun.* **2018,** *9,* 3367.

[13] Jin, M.; Oh, D.; Park, J.; Lee, C.; Lee, S.; Park, J.; Lee, K.; Lee, D. "Mesoporous silica supported Pd-MnOx catalysts with excellent catalytic activity in room-temperature formic acid decomposition", *Sci. Rep.-UK* **2016,** *6,* 33502.

[14] Yan, W.; Ramanathan, A.; Ghanta, M.; Subramaniam, B. "Towards highly selective ethylene epoxidation catalysts using hydrogen peroxide and tungsten- or niobium-incorporated mesoporous silicate (KIT-6)", *Catal. Sci. Technol.* **2014,** *4,* 4433–4439.

[15] Patel, P. D.; Laird, B. B.; Thompson, W. H. "A density functional theory study of ethylene epoxidation catalyzed by niobium-doped silica", *J. Mol. Catal. A: Chemical* **2016,** *424,* 1–7.

[16] Peters, B.; Scott, S. L. "Single atom catalysts on amorphous supports: A quenched disorder perspective", *J. Chem. Phys.* **2015,** *142,* 104708.

[17] Goldsmith, B. R.; Peters, B.; Johnson, J. K.; Gates, B. C.; Scott, S. L. "Beyond ordered materials: Understanding catalytic sites on amorphous solids", *ACS Catal.* **2017,** *7,* 7543–7557.

[18] Roeffaers, M.; De Cremer, G.; Libeert, J.; Ameloot, R.; Dedecker, P.; Bons, A.-J.; Bückins, M.; Martens, J.; Sels, B.; De Vos, D.; Hofkens, J. "Super-resolution reactivity mapping of nanostructured catalyst particles", *Angew. Chem. Int. Edit.* **2009,** *48,* 9285–9289.

[19] Jystad, A.; Caricato, M. "Computational multinuclear NMR characterization of metal-doped amorphous silica catalysts", *Chem. Mater.* **2018,** *30,* 7813–7822.

[20] Mohan, D.; Pittman, C. "Arsenic removal from water/wastewater using adsorbents – A critical review", *J. Hazard. Mater.* **2007,** *142,* 1–53.

[21] Brady, R.; Woonton, B.; Gee, M.; O'Connor, A. "Hierarchical mesoporous silica materials for separation of functional food ingredients – A review", *Innov. Food Sci. Emerg.* **2008,** *9,* 243–248.

[22] Vallet-Regí, M.; Balas, F.; Arcos, D. "Mesoporous materials for drug delivery", *Angew. Chem. Int. Edit.* **2007,** *46,* 7548–7558.

[23] Manzano, M.; Vallet-Regí, "New developments in ordered mesoporous materials for drug delivery", *J. Mater. Chem.* **2010,** *20,* 5593–5604.

[24] De, M.; Ghosh, P.; Rotello, V. "Applications of nanoparticles in biology", *Advanced Materials* **2008,** *20,* 4225–4241.

[25] Woodcock, L. V.; Angell, C. A.; Cheeseman, P. "Molecular dynamics studies of the vitreous state: Simple ionic systems and silica", *J. Chem. Phys.* **1976,** *65,* 1565–1577.

[26] Soules, T. F.; Gilmer, G. H.; Matthews, M. J.; Stolken, J. S.; Feit, M. D. "Silica molecular dynamic force fields—A practical assessment", *J. Non-Cryst. Solids* **2011,** *357,* 1564–1573.

[27] Cygan, R. T.; Liang, J.-J.; Kalinichev, A. G. "Molecular models of hydroxide, oxyhydroxide, and clay phases and the development of a general force field", *J. Phys. Chem. B* **2004,** *108,* 1255–1266.

[28] Zeitler, T. R.; Greathouse, J. A.; Gale, J. D.; Cygan, R. T. "Vibrational analysis of brucite surfaces and the development of an improved force field for molecular simulation of interfaces", *J. Phys. Chem. C* **2014,** *118,* 7946–7953.

[29] Tsuneyuki, S.; Tsukada, M.; Aoki, H.; Matsui, Y. "First-principles interatomic potential of silica applied to molecular dynamics", *Phys. Rev. Lett.* **1988,** *61,* 869–872.

[30] Demiralp, E.; Çağin, T.; Goddard, W. A. "Morse stretch potential charge equilibrium force field for ceramics: Application to the quartz-stishovite phase transition and to silica glass", *Phys. Rev. Lett.* **1999,** *82,* 1708–1711.

[31] Garofalini, S. H. "Molecular dynamics simulation of the frequency spectrum of amorphous silica", *J. Chem. Phys.* **1981,** *76,* 3189–3192.

[32] Feuston, B.; Garofalini, S. "Empirical three-body potential for vitreous silica", *J. Chem. Phys.* **1988,** *89,* 5818–5824.

[33] Vashishta, P.; Kalia, R. K.; Rino, J. P.; Ebbsjö, I. "Interaction potential for SiO_2: A molecular-dynamics study of structural correlations", *Phys. Rev. B* **1990,** *41,* 12197–12209.

[34] van Duin, A.; Strachan, A.; Stewman, S.; Zhang, Q.; Xu, X.; Goddard, W. "ReaxFF SiO reactive force field for silicon and silicon oxide systems", *J. Phys. Chem. A* **2003,** *107,* 3803-3811.

[35] Fogarty, J. C.; Aktulga, H. M.; Grama, A. Y.; van Duin, A. C. T.; Pandit, S. A. "A reactive molecular dynamics simulation of the silica-water interface", *J. Chem. Phys.* **2010,** *132,* 174704.

[36] Argyris, D.; Tummala, N. R.; Striolo, A.; Cole, D. R. "Molecular structure and dynamics in thin water films at the silica and graphite surfaces", *J. Phys. Chem. C* **2008,** *112,* 13587–13599.

[37] Argyris, D.; Cole, D. R.; Striolo, A. "Dynamic behavior of interfacial water at the silica surface", *J. Phys. Chem. C* **2009,** *113,* 19591–19600.

[38] Le, T.; Striolo, A.; Cole, D. R. "CO_2–C_4H_{10} mixtures simulated in silica slit pores: Relation between structure and dynamics", *J. Phys. Chem. C* **2015,** *119,* 15274–15284.

[39] Ding, F.; Hu, Z.; Zhong, Q.; Manfred, K.; Gattass, R. R.; Brindza, M. R.; Fourkas, J. T.; Walker, R. A.; Weeks, J. D. "Interfacial organization of acetonitrile: simulation and experiment", *J. Phys. Chem. C* **2010,** *114,* 17651–17659.

[40] Hu, Z.; Weeks, J. D. "Acetonitrile on silica surfaces and at its liquid-vapor interface: Structural correlations and collective dynamics", *J. Phys. Chem. C* **2010,** *114,* 10202–10211.

[41] Berne, B. J.; Fourkas, J. T.; Walker, R. A.; Weeks, J. D. "Nitriles at silica interfaces resemble supported lipid bilayers", *Acc. Chem. Res* **2016,** *49,* 1605–1613.

[42] Milischuk, A. A.; Ladanyi, B. M. "Structure and dynamics of water confined in silica nanopores", *J. Chem. Phys.* **2011,** *135,* 174709.

[43] Romero-Vargas Castrillón, S.; Giovambattista, N.; Aksay, I. A.; Debenedetti, P. G. "Effect of surface polarity on the structure and dynamics of water in nanoscale confinement", *J. Phys. Chem. B* **2009,** *113,* 1438–1446.

[44] Romero-Vargas Castrillón, S.; Giovambattista, N.; Aksay, I. A.; Debenedetti, P. G. "Evolution from surface-influenced to bulk-like dynamics in nanoscopically confined water", *J. Phys. Chem. B* **2009,** *113,* 7973–7976.

[45] Romero-Vargas Castrillón, S.; Giovambattista, N.; Aksay, I. A.; Debenedetti, P. G. "Effect

of surface polarity on the structure and dynamics of water in nanoscale confinement", *J. Phys. Chem. B* **2009,** *113,* 1438–1446.

[46] Giovambattista, N.; Debenedetti, P. G.; Rossky, P. J. "Enhanced surface hydrophobicity by coupling of surface polarity and topography", *Proc. Natl. Acad. Sci. USA* **2009,** *106,* 15181–15185.

[47] Romero-Vargas Castrillón, S.; Giovambattista, N.; Aksay, I. A.; Debenedetti, P. G. "Structure and energetics of thin film water", *J. Phys. Chem. C* **2011,** *115,* 4624–4635.

[48] Stirnemann, G.; Castrillón, S. R.-V.; Hynes, J. T.; Rossky, P. J.; Debenedetti, P. G.; Laage, D. "Non-monotonic dependence of water reorientation dynamics on surface hydrophilicity: Competing effects of the hydration structure and hydrogen-bond strength", *Phys Chem Chem Phys* **2011,** *13,* 19911–19917.

[49] Bourg, I. C.; Steefel, C. I. "Molecular dynamics simulations of water structure and diffusion in silica nanopores", *J. Phys. Chem. C* **2012,** *116,* 11556–11564.

[50] Gulmen, T. S.; Thompson, W. H. "Grand canonical Monte Carlo simulations of acetonitrile filling of silica pores of varying hydrophilicity/hydrophobicity", *Langmuir* **2009,** *25,* 1103–1111.

[51] Morales, C. M.; Thompson, W. H. "Simulations of infrared spectra of nanoconfined liquids: acetonitrile confined in nanoscale, hydrophilic silica pores", *J. Phys. Chem. A* **2009,** *113,* 1922–1933.

[52] Laage, D.; Thompson, W. H. "Reorientation dynamics of nanoconfined water: Power-law decay, hydrogen-bond jumps, and test of a two-state model", *J. Chem. Phys.* **2012,** *136,* 044513.

[53] Fogarty, A. C.; Duboué-Dijon, E.; Laage, D.; Thompson, W. H. "Origins of the non-

exponential reorientation dynamics of nanoconfined water", *J. Chem. Phys.* **2014,** *141,* 18C523.

[54] Norton, C. D.; Thompson, W. H. "On the diffusion of acetonitrile in nanoscale amorphous silica pores. Understanding anisotropy and the effects of hydrogen bonding", *J. Phys. Chem. C* **2013,** *117,* 19107–19114.

[55] Norton, C. D.; Thompson, W. H. "Reorientation dynamics of nanoconfined acetonitrile: A critical examination of two-state models", *J. Phys. Chem. B* **2014,** *118,* 8227–8235.

[56] Yamada, S. A.; Shin, J. Y.; Thompson, W. H.; Fayer, M. D. "Water dynamics in nanoporous silica: Ultrafast vibrational spectroscopy and molecular dynamics simulations", *J. Phys. Chem. C* **2019,** *123,* 5790–5803.

[57] Yamada, S. A.; Hung, S. T.; Thompson, W. H.; Fayer, M. D. "Effects of pore size on water dynamics in mesoporous silica", *J. Chem. Phys.* **2020,** *152,* 154704.

[58] Cowen, B. J.; El-Genk, M. S. "On force fields for molecular dynamics simulations of crystalline silica", *Comp. Mater. Sci.* **2015,** *107,* 88–101.

[59] Kulkarni, A. D.; Truhlar, D. G.; Goverapet Srinivasan, S.; van Duin, A. C. T.; Norman, P.; Schwartzentruber, T. E. "Oxygen interactions with silica surfaces: Coupled cluster and density functional investigation and the development of a new ReaxFF potential", *J. Phys. Chem. C* **2013,** *117,* 258–269.

[60] Yeon, J.; van Duin, A. C. T. "ReaxFF molecular dynamics simulations of hydroxylation kinetics for amorphous and nano-silica structure, and its relations with atomic strain energy", *J. Phys. Chem. C* **2016,** *120,* 305–317.

[61] Rimsza, J. M.; Yeon, J.; van Duin, A. C. T.; Du, J. "Water interactions with nanoporous silica: Comparison of ReaxFF and *ab initio* based molecular dynamics simulations", *J. Phys. Chem. C* **2016,** *120,* 24803–24816.

[62] Mahadevan, T. S.; Garofalini, S. H. "Dissociative chemisorption of water onto silica surfaces and formation of hydronium ions", *J. Phys. Chem. B* **2008,** *112,* 1507–1515.

[63] Lockwood, G. K.; Garofalini, S. H. "Bridging oxygen as a site for proton adsorption on the vitreous silica surface", *J. Chem. Phys.* **2009,** *131,* 074703.

[64] Kagan, M.; Lockwood, G. K.; Garofalini, S. H. "Reactive simulations of the activation barrier to dissolution of amorphous silica in water", *Phys. Chem. Chem. Phys.* **2014,** *16,* 9294–9301.

[65] C., M.; Kob, W.; Binder, K. "Classical and ab-initio molecular dynamic simulation of an amorphous silica surface", *Comput. Phys. Commun.* **2002,** *147,* 222-225.

[66] Benoit, M.; Kob, W. "The vibrational dynamics of vitreous silica: Classical force fields vs. first principles", *Europhys. Lett.* **2002,** *60,* 269-275.

[67] Skelton, A. A.; Fenter, P.; Kubicki, J. D.; Wesolowski, D. J.; Cummings, P. T. "Simulations of the quartz($10\bar{1}1$)/water interface: A comparison of classical force fields, ab-initio molecular dynamics, and x-ray reflectivity experiments", *J. Phys. Chem. C* **2011,** *115,* 2076–2088.

[68] Skelton, A. A.; Wesolowski, D. J.; Cummings, P. T. "Investigating the quartz ($10\bar{1}0$)/water interface using classical and ab-initio molecular dynamics", *Langmuir* **2011,** *27,* 8700–8709.

[69] Leung, K.; Nielsen, I. M. B.; Criscenti, L. J. "Elucidating the bimodal acid-base behavior of the water-silica interface from first principles", *J. Am. Chem. Soc.* **2009,** *131,* 18358–18365.

[70] Wright, L. B.; Walsh, T. R. "First-principles molecular dynamics simulations of NH_4^+ and CH_3COO^- adsorption at the aqueous quartz interface", *J. Chem. Phys.* **2012,** *137,* 224702.

[71] Gaigeot, M.-P.; Sprik, M.; Sulpizi, M. "Oxide/water interfaces: How the surface chemistry modifies interfacial water properties", *J. Phys.-Condens. Mat.* **2012,** *24,* 124106.

[72] Sulpizi, M.; Gaigeot, M.-P.; Sprik, M. "The silica–water interface: How the silanols determine the surface acidity and modulate the water properties", *J. Chem. Theor. Comp.* **2012,** *8,* 1037–1047.

[73] Cimas, Á.; Tielens, F.; Sulpizi, M.; Gaigeot, M.-P.; Costa, D. "The amorphous silica–liquid water interface studied by ab initiomolecular dynamics (AIMD): local organization in global disorder", *J. Phys.-Condens. Mat.* **2014,** *26,* 244106.

[74] Pfeiffer-Laplaud, M.; Costa, D.; Tielens, F.; Gaigeot, M.-P.; Sulpizi, M. "Bimodal acidity at the amorphous silica/water interface", *J. Phys. Chem. C* **2015,** *119,* 27354–27362.

[75] Pfeiffer-Laplaud, M.; Gaigeot, M.-P.; Sulpizi, M. "pK_a at quartz/electrolyte interfaces", *J. Phys. Chem. Lett.* **2016,** *7,* 3229–3234.

[76] Parashar, S.; Lesnicki, D.; Sulpizi, M. "Increased acid dissociation at the quartz/water interface", *J. Phys. Chem. Lett.* **2018,** *9,* 2186–2189.

[77] Black, J. E.; Iacovella, C. R.; Cummings, P. T.; McCabe, C. "Molecular dynamics study of alkylsilane monolayers on realistic amorphous silica surfaces", *Langmuir* **2015,** *31,* 3086–3093.

[78] Vollmayr, K.; Kob, W.; Binder, K. "Cooling-rate effects in amorphous silica: A computer-simulation study", *Phys. Rev. B* **1996,** *54,* 15808-15827.

[79] Varghese, J. J.; Mushrif, S. H. "Origins of complex solvent effects on chemical reactivity and computational tools to investigate them: A review", *React. Chem. Eng.* **2019,** *4,* 165–206.

[80] Davies, P. R. "On the role of water in heterogeneous catalysis: A tribute to Professor M. Wyn Roberts", *Top. Catal.* **2016,** *59,* 671–677.

[81] Lari, G. M.; Dapsens, P. Y.; Scholz, D.; Mitchell, S.; Mondelli, C.; Pérez-Ramírez, J.

"Deactivation mechanisms of tin-zeolites in biomass conversions", *Green Chem.* **2016,** *18,* 1249–1260.

[82] Baum, M.; Rébiscoul, D.; Juranyi, F.; Rieutord, F. "Structural and dynamical properties of water confined in highly ordered mesoporous silica in the presence of electrolytes", *J. Phys. Chem. C* **2018,** *122,* 19857–19868.

[83] Chen, L.; He, X.; Liu, H.; Qian, L.; Kim, S. H. "Water adsorption on hydrophilic and hydrophobic surfaces of silicon", *J. Phys. Chem. C* **2018,** *122,* 11385–11391.

[84] Alabarse, F. G.; Haines, J.; Cambon, O.; Levelut, C.; Bourgogne, D.; Haidoux, A.; Granier, D.; Coasne, B. "Freezing of water confined at the nanoscale", *Phys. Rev. Lett.* **2012,** *109*, 035701.

[85] Mancinelli, R.; Bruni, F.; Ricci, M. "Structural studies of confined liquids: The case of water confined in MCM-41", *J. Mol. Liq.* **2011,** *159*, 42–46.

[86] Ostroverkhov, V.; Waychunas, G.; Shen, Y. "Vibrational spectra of water at water/alpha-quartz (0001) interface", *Chem. Phys. Lett.* **2004,** *386,* 144–148.

[87] Ostroverkhov, V.; Waychunas, G.; Shen, Y. "New information on water interfacial structure revealed by phase-sensitive surface spectroscopy", *Phys. Rev. Lett.* **2005,** *94*, –.

[88] Myalitsin, A.; Urashima, S.-h.; Nihonyanagi, S.; Yamaguchi, S.; Tahara, T. "Water structure at the buried silica/aqueous interface studied by heterodyne-detected vibrational sum-frequency generation", *J. Phys. Chem. C* **2016,** *120,* 9357–9363.

[89] Urashima, S.-h.; Myalitsin, A.; Nihonyanagi, S.; Tahara, T. "The topmost water structure at a charged silica/aqueous interface revealed by heterodyne-detected vibrational sum frequency generation spectroscopy", *J. Phys. Chem. Lett.* **2018,** *9,* 4109–4114.

[90] Gordillo, M.; Marti, J. "Molecular dynamics description of a layer of water molecules on a hydrophobic surface", *J. Chem. Phys.* **2002,** *117*, 3425–3430.

[91] Levine, S.; Garofalini, S. "A structural analysis of the vitreous silica surface via a molecular dynamics computer simulation", *J. Chem. Phys.* **1987,** *86,* 2997-3002.

[92] Vollmayr, K.; Kob, W.; Binder, K. "How do the properties of a glass depend on the cooling rate? A computer simulation study of a Lennard-Jones system", *J. Chem. Phys.* **1996,** *105,* 4714–4728.

[93] Roder, A.; Kob, W.; Binder, K. "Structure and dynamics of amorphous silica surfaces", *J. Chem. Phys.* **2001,** *114,* 7602-7614.

[94] Brinker, C. J.; Scherer, G. W. *Sol-Gel Science: The Physics and Chemistry of Sol-Gel Processing;* Academic Press: San Diego, CA, 1990.

[95] Liu, G.; Li, Y.-Z.; Jonas, J. "Confined Geometry Effects on Reorientational Dynamics of Molecular Liquids in Porous Silica Glasse", *J. Chem. Phys.* **1991,** *95,* 6892–6901.

[96] Loughnane, B. J.; Farrer, R. A.; Scodinu, A.; Fourkas, J. T. "Dynamics of a wetting liquid in nanopores: An optical Kerr effect study of the dynamics of acetonitrile confined in sol-gel glasses", *J. Chem. Phys.* **1999,** *111,* 5116–5123.

[97] Berendsen, H. J. C.; Postma, J. P. M.; van Gunsteren, W. F.; DiNola, A.; Haak, J. R. "Molecular dynamics with coupling to an external bath", *J. Chem. Phys.* **1984,** *81,* 3684–3690.

[98] The LAMMPS molecular dynamics package, http://lammps.sandia.gov.

[99] Plimpton, S. "Fast parallel algorithms for short-range molecular dynamics", *J. Comput. Phys.* **1995,** *117,* 1–19.

[100] Allen, M. P.; Tildesley, D. J. *Computer Simulation of Liquids;* Oxford: New York, NY, 1987.

[101] Schrader, A. M.; Monroe, J. I.; Sheil, R.; Dobbs, H. A.; Keller, T. J.; Li, Y.; Jain, S.; Shell, M. S.; Israelachvili, J. N.; Han, S. "Surface chemical heterogeneity modulates silica surface hydration", *Proc. Natl. Acad. Sci. USA* **2018,** *115,* 2890–2895.

[102] Rimsza, J.; Jones, R.; Criscenti, L. "Surface structure and stability of partially hydroxylated silica surfaces", *Langmuir* **2017,** *33,* 3882-3891.

[103] Ryckaert, J. P.; Ciccotti, G.; Berendsen, H. J. "Numerical integration of the cartesian equations of motion of a system with constraints: molecular dynamics of n-alkanes", *J. Comput. Phys.* **1977,** *23,* 327–341.

[104] Martínez, L.; Andrade, R.; Birgin, E. G.; Martínez, J. M. "PACKMOL: A package for building initial configurations for molecular dynamics simulations", *J. Comput. Chem.* **2009,** *30,* 2157–2164.

[105] Nosé, S. "A molecular dynamics method for simulations in the canonical ensemble", *Mol. Phys.* **1984,** *52,* 255–268.

[106] Hoover, W. G. "Canonical dynamics: Equilibrium phase-space distributions", *Phys. Rev. A* **1985,** *31,* 1695–1697.

[107] Berendsen, H. J. C.; Grigera, J. R.; Straatsma, T. P. "The missing term in effective pair potentials", *J. Phys. Chem.* **1987,** *91,* 6269–6271.

[108] Darden, T.; York, D.; Pedersen, L. "Particle mesh Ewald: An N·log(N) method for Ewald sums in large systems", *J. Chem. Phys.* **1993,** *98,* 10089–10092.

[109] Pollock, E. L.; Glosli, J. "Comments on PPPM, FMM, and the Ewald Method for Large Periodic Coulombic Systems", *Comput. Phys. Comm.* **1995,** *95,* 93–110.

[110] Fogarty, A. C.; Duboué-Dijon, E.; Laage, D.; Thompson, W. H. "Origins of the non-exponential reorientation dynamics of nanoconfined water", *J. Chem. Phys.* **2014,** *141,* 18C523.

[111] Burris, P. C.; Laage, D.; Thompson, W. H. "Simulations of the Infrared, Raman, and 2D-IR Photon Echo Spectra of Water in Nanoscale Silica Pores", *J. Chem. Phys.* **2016,** *144,* 194709.

[112] D., B.; Blanc, A.; A., G.; Fajula, F. "New trends in the design of supported catalysts on mesoporous silicas and their applications in fine chemicals", *Catal. Today* **2002,** *73,* 139-152.

[113] Thornburg, N. E.; Nauert, S. L.; Thompson, A. B.; Notestein, J. M. "Synthesis-structure-function relationships of silica-supported niobium(V) catalysts for alkene epoxidation with H_2O_2", *ACS Catal.* **2016,** *6,* 6124–6134.

[114] Yang, J.; Meng, S.; Xu, L.; Wang, E. G. "Water adsorption on hydroxylated silica surfaces studied using the density functional theory", *Phys. Rev. B* **2005,** *71,* 258–12.

[115] Roy, D.; Liu, S.; Woods, B. L.; Siler, A. R.; Fourkas, J. T.; Weeks, J. D.; Walker, R. A. "Nonpolar adsorption at the silica/methanol interface: Surface mediated polarity and solvent density across a strongly associating solid/liquid boundary", *J. Phys. Chem. C* **2013,** *117,* 27052–27061.

[116] Karnes, J. J.; Gobrogge, E. A.; Walker, R. A.; Benjamin, I. "Unusual structure and dynamics at silica/methanol and silica/ethanol interfaces—a molecular dynamics and nonlinear optical study", *J. Phys. Chem. B* **2016,** *120,* 1569–1578.

[117] Rybka, J.; Kärger, J.; Tallarek, U. "Single-molecule and ensemble diffusivities in individual nanopores with spatially dependent mobility", *ChemPhysChem* **2017,** *18,* 2094–2102.

[118] Wang, Y.-P.; Ren, K.; Liu, S. "The joint effect of surface polarity and concentration on the structure and dynamics of acetonitrile solution: a molecular dynamics simulation study", *Phys. Chem. Chem. Phys.* **2020,** *22,* 10322–10334.

[119] Rarivomanantsoa, M.; Jund, P.; Jullien, R. "Classical molecular dynamics simulations of amorphous silica surfaces", *J. Phys-Condens. Mat.* **2001,** *13,* 6707-6718.

[120] C., M.; Kob, W.; Binder, K. "Classical and ab-initio molecular dynamic simulation of an amorphous silica surface", *Comput. Phys. Commun.* **2002,** *147,* 222-225.

[121] Pedone, A.; Malavasi, G.; Menziani, M. C.; Segre, U.; Musso, F.; Corno, M.; Civalleri, B.; Ugliengo, P. "FFSiOH: A new force field for silica polymorphs and their hydroxylated surfaces based on periodic B3LYP calculations", *Chem. Mater.* **2008,** *20,* 2522–2531.

[122] Munetoh, S.; Motooka, T.; Moriguchi, K.; Shintani, A. "Interatomic potential for Si–O systems using Tersoff parameterization", *Comp. Mater. Sci.* **2007,** *39,* 334–339.

[123] Hassanali, A. A.; Singer, S. J. "Model for the water-amorphous silica interface: The undissociated surface", *J. Phys. Chem. B* **2007,** *111,* 11181–11193.

[124] Yu, J.; Devanathan, R.; Weber, W. J. "Unified interatomic potential for zircon, zirconia and silica systems", *J. Mater. Chem.* **2009,** *19,* 3923–3930.

[125] Koziatek, P.; Barrat, J.; Rodney, D. "Short- and medium-range orders in as-quenched and deformed SiO_2 glasses: An atomistic study", *J. Non-Cryst. Solids* **2015,** *414,* 7–15.

[126] Alan, B. O.; Barisik, M.; Ozcelik, H. G. "Roughness effects on the surface charge properties of silica nanoparticles", *J. Phys. Chem. C* **2020,** *124,* 7274–7286.

[127] Shoemaker, D. P.; Garland, C. W.; Nibler, J. W. *Experiments in physical chemistry;* McGraw-Hill: New York, NY, 1989.

[128] Mozzi, R.; Warren, B. "The structure of vitreous silica", *J. Appl. Crystallogr.* **1969,** *2,* 164–172.

[129] Da Silva, J. R. G.; Pinatti, D. G.; Anderson, C. E.; L., R. M. "A refinement of the structure of vitreous silica", *Philos. Mag.* **1975,** *31,* 713-717.

[130] Coombs, P. G.; De Natale, J. F.; Hood, P. J.; McElfresh, E. K.; Wortman, R. S.; Schackelford, J. F. "The nature of the Si–O–Si bond angle distribution in vitreous silica", *Philos. Mag.* **1985,** *51,* L39-L42.

[131] Du, J.; Cormack, A. N. "Molecular dynamics simulation of the structure and hydroxylation of silica glass surfaces", *J. Am. Ceram. Soc.* **2005,** *88,* 2532–2539.

[132] Rarivomanantsoa, M.; Jund, P.; Jullien, R. "Classical molecular dynamics simulations of amorphous silica surfaces", *J. Phys-Condens. Mat.* **2001,** *13,* 6707-6718.

[133] Feuston, B.; Garofalini, S. "Topological and bonding defects in vitreous silica surfaces", *J. Chem. Phys.* **1989,** *91,* 564–570.

[134] Feuston, B.; Garofalini, S. "Water-induced relaxation of the vitreous silica surface", *J. Appl. Phys.* **1990,** *68,* 4830–4836.

[135] Warren, W.; Kanicki, J.; Rong, F.; Poindexter, E. "Paramagnetic point defects in amorphous silicon dioxide and amorphous silicon nitride thin films", *J. Electrochem. Soc.* **1992,** *139,* 872–880.

[136] Safar, M.; Alenzi, K.; Albehairy, S. "Counting cycles in an undirected graph using DFS-XOR algorithm", *2009 1st International Conference on Networked Digital Technologies, NDT 2009* **2009,** 132–139.

[137] Bell, R. J.; Dean, P. "The structure of vitreous silica : Validity of the random network theory", *Philos. Mag.* **1972,** *25,* 1381–1398.

[138] Guttman, L. "Ring structure of the crystalline and amorphous forms of silicon dioxide", *J. Non-Cryst. Solids* **1990,** *116,* 145–147.

[139] King, S. "Ring configurations in a random network model of vitreous silica", *Nature Publishing Group* **1967,** *216,* 615–616.

[140] Mitra, S. K. "Molecular dynamics simulation of silicon dioxide glass", *Philos. Mag. B* **1982,** *45,* 529-548.

[141] Zeitler, T. R.; Cormack, A. "Interaction of water with bioactive glass surfaces", *J. Cryst. Growth* **2006,** *294,* 96 - 102.

[142] Shen, Y. R.; Ostroverkhov, V. "Sum-frequency vibrational spectroscopy on water interfaces: polar orientation of water molecules at interfaces.", *Chem. Rev.* **2006,** *106,* 1140–1154.

[143] Laage, D.; Hynes, J. T. "A molecular jump mechanism of water reorientation", *Science* **2006,** *311,* 832–835.

[144] Laage, D.; Hynes, J. T. "On the molecular mechanism of water reorientation", *J. Phys. Chem. B* **2008,** *112,* 14230–14242.

[145] Mitternacht, S. "FreeSASA: An open source C library for solvent accessible surface area calculations", 2016 F1000Research 5:189.

[146] Liang, Y.; Miranda, C. R.; Scandolo, S. "Mechanical strength and coordination defects in compressed silica glass: Molecular dynamics simulations", *Phys. Rev. B* **2007,** *75,* 024205.

[147] Minton, A. P. "The Influence of Macromolecular Crowding and Macromolecular Confinement on Biochemical Reactions in Physiological Media", *J. Biol. Chem.* **2001,** *276,* 10577–10580.

[148] Wang, Y.; Bryan, C.; Xu, H.; Gao, H. "Nanogeochemistry: Geochemical Reactions and Mass Transfers in Nanopores", *Geology* **2003,** *31,* 387–390.

[149] Alarcos, N.; Cohen, B.; Ziółek, M.; Douhal, A. "Photochemistry and Photophysics in Silica-Based Materials: Ultrafast and Single Molecule Spectroscopy Observation", *Chem. Rev.* **2017,** *117,* 13639–13720.

[150] Thompson, W. H. "Perspective: Dynamics of confined liquids", *J. Chem. Phys.* **2018,** *149,* 170901.

[151] Yan, W.; Ramanadan, A.; Patel, P.; Maiti, S.; Laird, B.; Thompson, W.; Subramaniam, B. "Mechanistic insights for enhancing activity and stability of Nb-incorporated silicates for selective ethylene epoxidation", *J. Catal.* **2016,** *336,* 75–84.

[152] Soled, S. "Silica-supported catalysts get a new breath of life", *Science* **2015,** *350,* 1171–1172.

[153] Santiso, E. E.; George, A. M.; Turner, C. H.; Kostov, M. K.; Gubbins, K. E.; Buongiorno-Nardelli, M.; Sliwinska-Bartkowiak, M. "Adsorption and catalysis: The effect of confinement on chemical reactions", *Appl. Surf. Sci.* **2005,** *252,* 766–777.

[154] Malfait, B.; Correia, Natália, T.; Ciotonea, C.; Dhainaut, J.; Dacquin, J.-P.; Royer, S.; Tabary, N.; Guinet, Y.; Hédoux, A. "Manipulating the physical states of confined ibuprofen in SBA-15 based drug delivery systems obtained by solid-state loading: Impact of the loading degree", *J. Chem. Phys.* **2020,** *153,* 154506.

[155] Lin, Y. S.; Pieniazek, P. A.; Yang, M.; Skinner, J. L. "On the calculation of rotational anisotropy decay, as measured by ultrafast polarization-resolved vibrational pump-probe experiments", *J. Chem. Phys.* **2010,** *132,* 174505.

[156] Gordon, R. G. "Relations between raman spectroscopy and nuclear spin relaxation", *J. Chem. Phys.* **1965,** *42,* 3658–3665.

[157] Bakker, H. J.; Skinner, J. L. "Vibrational spectroscopy as a probe of structure and dynamics in liquid water", *Chem. Rev.* **2010,** *110,* 1498–1517.

[158] Rezus, Y. L. A.; Bakker, H. J. "On the orientational relaxation of HDO in liquid water", *J. Chem. Phys.* **2005,** *123,* 114502.

[159] Petersen, C.; Tielrooij, K. J.; Bakker, H. J. "Strong temperature dependence of water reorientation in hydrophobic hydration shells", *J. Chem. Phys.* **2009,** *130,* 214511.

[160] Piletic, I. R.; Moilanen, D. E.; Spry, D. B.; Levinger, N. E.; Fayer, M. D. "Testing the core/shell model of nanoconfined water in reverse micelles using linear and nonlinear IR spectroscopy", *J. Phys. Chem. A* **2006,** *110,* 4985–4999.

[161] Moilanen, D. E.; Fenn, E. E.; Lin, Y.-S.; Skinner, J. L.; Bagchi, B.; Fayer, M. D. "Water inertial reorientation: Hydrogen bond strength and the angular potential", *P. Natl. Acad. Sci. USA* **2008,** *105,* 5295–5300.

[162] Nicodemus, R. A.; Corcelli, S. A.; Skinner, J. L.; Tokmakoff, A. "Collective hydrogen bond reorganization in water studied with temperature-dependent ultrafast infrared spectroscopy", *J. Phys. Chem. B* **2011,** *115,* 5604–5616.

[163] Piskulich, Z. A.; Mesele, O. O.; Thompson, W. H. "Removing the barrier to the calculation of activation energies: Diffusion coefficients and reorientation times in liquid water", *J. Chem. Phys.* **2017,** *147,* 134103.

[164] Croissant, J. G.; Butler, K. S.; Zink, J. I.; Brinker, C. J. "Synthetic amorphous silica nanoparticles: toxicity, biomedical and environmental implications", *Nat. Rev. Mater.* **2020,** *5,* 886–909.

[165] Zhang, H. *et al.* "Processing pathway dependence of amorphous silica nanoparticle toxicity: Colloidal vs pyrolytic", *J. Am. Chem. Soc.* **2012,** *134,* 15790–15804.